Benedetta Cappa Marinetti
Artista Futurista
“ Velocità di motoscafo ”
(1919 - 1924)

GREEN PROCESSES BASED ON SC-CO_2: APPLICATION TO MATERIALS OF BIOMEDICAL INTEREST

Lucia Baldino

Unione Europea

Ministero dell'Istruzione,
dell'Università e della Ricerca

UNIVERSITÀ DEGLI
STUDI DI SALERNO

Department of Industrial Engineering

Ph.D. Course in Chemical Engineering
(XIII Cycle)

GREEN PROCESSES BASED ON SC-CO_2: APPLICATION TO MATERIALS OF BIOMEDICAL INTEREST

Supervisors
Prof. Ernesto Reverchon
Dr. Iolanda De Marco

Ph.D. Student
Lucia Baldino

Scientific Referees
Prof. Nicola Maffulli
Dr. Stefano Cardea
Dr. Mariella Fusco

Ph.D. Course Coordinator
Prof. Paolo Ciambelli

Publication list

International journals

Reverchon E., Baldino L., Cardea S., De Marco I., 2012, Biodegradable synthetic scaffolds for tendon regeneration, **Muscles, Ligaments and Tendons Journal**, 2, 181-186.

Cardea S., Baldino L., De Marco I., Pisanti P., Reverchon E., 2013, Supercritical gel drying of polymeric hydrogels for tissue engineering applications, **Chemical Engineering Transactions**, 32, 1123-1128.

Cardea S., Baldino L., Pisanti P., Reverchon E., 2014, 3-D PLLA scaffolds formation by a supercritical freeze extraction assisted process, **Journal of Materials Science: Materials in Medicine**, 25, 355-362.

Baldino L., Cardea S., Reverchon E., 2014, Supercritical assisted enzymatic membranes preparation, for active packaging applications, **Journal of Membrane Science**, 453, 409-418.

Cardea S., Baldino L., Scognamiglio M., Reverchon E., 2014, 3D PLLA/Ibuprofen composite scaffolds obtained by a supercritical fluids assisted process, **Journal of Materials Science: Materials in Medicine**, 25, 989-998.

De Marco I., Baldino L., Cardea S., Reverchon E., 2014, Production of ethyl cellulose scaffolds by supercritical CO_2 phase separation, **Chemical Engineering Transactions**, 38, 265-270.

Cardea S., Baldino L., De Marco I., Reverchon E., 2014, Generation of loaded PMMA scaffolds using supercritical CO_2 assisted phase separation, **Chemical Engineering Transactions**, 38, 241-246.

Baldino L., Cardea S., De Marco I., Reverchon E., 2014, Chitosan scaffolds formation by a supercritical freeze extraction process, **The Journal of Supercritical Fluids**, 90, 27-34.

Baldino L., Cardea S., Reverchon E., 2014, Alginate scaffolds for vascular application, **Journal of Tissue Engineering and Regenerative Medicine**, 8, 457-458.

Reverchon E., Baldino L., Cardea S., 2014, Technical aspects on biodegradable scaffolds and applications of supercritical fluids assisted processes, **Journal of Tissue Engineering and Regenerative Medicine**, 8, 16.

Campardelli R., Baldino L., Reverchon E., Supercritical fluids applications in nanomedicine, **The Journal of Supercritical Fluids, in press**.

De Marco I., Baldino L., Cardea S., Reverchon E., Supercritical gel drying for the production of starch aerogels for delivery systems, **submitted to Chemical Engineering Transactions**.

Baldino L., Cardea S., Reverchon E., Natural aerogels production by supercritical gel drying, **submitted to Chemical Engineering Transactions**.

Baldino L., Cardea S., Reverchon E., Antimicrobial membranes produced by supercritical assisted phase inversion, **submitted to Chemical Engineering Transactions**.

De Marco I., Baldino L., Cardea S., Reverchon E., Effect of process parameters on Cellulose Acetate scaffolds morphology obtained by supercritical CO_2 phase inversion, **submitted to CRC Press/Balkema (Taylor & Francis Group)**.

Baldino L., Concilio S., Cardea S., De Marco I., Reverchon E., Complete glutaraldehyde elimination during chitosan hydrogel drying by SC-CO_2 processing, **submitted to Carbohydrate Polymers**.

Baldino L., Sarno M., Cardea S., Irusta S., Ciambelli P., Santamaria J., Reverchon E., Graphene oxide exfoliation and purification during the formation of cellulose acetate nanocomposites by supercritical CO_2 assisted phase inversion, **submitted to Journal of Membrane Science**.

Baldino L., Cardea S., Maffulli N., Reverchon E., Regeneration techniques for tendon-to-bone and tendon-to-muscle interfaces reconstruction, **submitted to Tissue Engineering Part B**.

Baldino L., Naddeo F., Cardea S., Naddeo A., Reverchon E., FEM modeling of the reinforcement mechanism of hydroxyapatite in PLLA scaffolds produced by supercritical drying, for Tissue Engineering applications, **submitted to Journal of the Mechanical Behavior of Biomedical Materials**.

Book

Baldino L., Maffulli N., Reverchon E., Bone-Tendon Interface, **Regenerative Engineering of Musculoskeletal Tissues and Interfaces, Eds. Syam Nukavarapu, Joseph Freeman, Cato Laurencin, 2015, in press**.

Proceedings

Baldino L., Cardea S., Reverchon E., Supercritical assisted enzymatic membranes preparation, 10th Conference on Supercritical Fluids and Their Applications, Naples April 29 - May 6, 2013 E. Reverchon & I. De Marco Pag. 261-266 ISBN:88-7897-061-1 ID:4195305.

Cardea S., Baldino L., De Marco I., Scognamiglio M., Reverchon E., 3-D PLLA scaffolds formation by supercritical processing, 10th Conference on Supercritical Fluids and Their Applications, Naples April 29 - May 6, 2013 E. Reverchon & I. De Marco Pag. 309-314 ISBN:88-7897-061-1 ID:4195305.

Reverchon E., Della Porta G., Campardelli R., Baldino L., Cardea S., De Marco I., Tissue engineering using supercritical fluids based technology, 1st Scientific workshop on stem cells for ligament and tendon tissue engineering and regeneration, Pescara April 18, 2013 ISMULT Pag. 1-3 ID:4091653.

Baldino L., Cardea S., De Pascale M.L., Scognamiglio M., Reverchon E., 3-D composite scaffolds obtained by a supercritical fluids assisted process, 14th European Meeting on Supercritical Fluids, Marseille May 18-21, 2014.

Reverchon E., Baldino L., Supercritical fluids in nanomedicine, Translational nanomedicine international meeting, Angers August 27-29, 2014.

Patents

Baldino L., Cardea S., Reverchon E., 2013, “Procedimento per la produzione di membrane porose caricate con principi antimicrobici”, **VI2013A000285**.

Baldino L., Cardea S., Reverchon E., 2014, “Antimicrobically active packaging, antimicrobically active membrane for packaging and related uses”, **PCT/IB2014/066424**.

CONTENTS

CHAPTER I. INTRODUCTION 1

I.1 Tissue engineering 1
I.2 Natural and synthetic polymers for biomedical applications . 3
I.3 Three-dimensional polymeric scaffold fabrication and different kinds of scaffold 4
I.3.1 Porous scaffolds 5
I.3.2 Hydrogel scaffolds 5
I.3.3 Fibrous scaffolds 6
I.3.4 Microsphere scaffolds 6
I.3.5 Polymer-bioceramic composite scaffolds 7
I.3.6 Acellular scaffolds 7

CHAPTER II. SUPERCRITICAL ASSISTED PROCESSES VS TRADITIONAL PROCESSES FOR THE PRODUCTION OF MATERIALS OF BIOMEDICAL INTEREST 9

II.1 Supercritical foaming 9
II.2 Supercritical assisted phase separation 13
II.3 Processes based on solvent elimination by supercritical CO_2 15
II.3.1 Solvent casting + particulate leaching 15
II.3.2 Drying of ionic liquid-polymer mixtures 16
II.3.3 Gel drying 17
II.4 Electrospinning in supercritical CO_2 19

CHAPTER III. AIMS OF THE THESIS 23

CHAPTER IV. MATERIALS AND METHODS 25

IV.1 Materials 25
IV.1.1 Cellulose acetate (CA) 26
IV.1.2 PLLA 26

IV.1.3 Chitosan 26
IV.1.4 Lysozyme 26
IV.1.5 Graphene oxide 27
IV.1.6 Ibuprofen 27
IV.1.7 Hydroxyapatite 27
IV.2 Equipment 28
IV.3 Supercritical assisted phase separation 30
IV.4 Supercritical freeze extraction process 30
IV.5 Supercritical gel drying 30
IV.6 Analytical methods 31
IV.6.1 Field Emission Scanning Electron Microscopy (FESEM) 31
IV.6.2 Transmission Electron Microscopy (TEM) 31
IV.6.3 Structure pore size analysis 31
IV.6.4 Structure porosity 31
IV.6.5 Differential Scanning Calorimetry (DSC) 31
IV.6.6 Thermogravimetric Analysis (TGA) 32
IV.6.7 X-Ray Diffraction (XRD) 32
IV.6.8 Raman spectroscopy 32
IV.6.9 Energy dispersive X-ray spectroscopy (EDX) 32
IV.6.10 Fourier Transform Infrared Spectroscopy (FT-IR) 32
IV.6.11 Solvent residue analysis 32
IV.6.12 Mechanical test 33
IV.6.13 In vitro release assay 33
IV.6.14 Cells culture 33

CHAPTER V. RESULTS AND DISCUSSION 35

V.1 Cellulose acetate + Lysozyme 35
V.1.1 Enzymatic membranes preparation 35
V.1.2 Effect of process parameters on enzymatic membranes morphology 36
V.1.2.1 CA concentration 10% w/w 37
V.1.2.2 CA concentration 15% w/w 38
V.1.2.3 CA concentration 20% w/w 41

V.1.2.4 Comments and formation mechanisms 43
V.1.3 Other characterizations of CA membranes 45
V.1.4 Lysozyme release kinetics and activity 47
V.1.4.1 Influence of CA concentration on the kinetics of lysozyme release 48
V.1.4.2 Influence of CA concentration on mobile lysozyme activity... 52
V.1.4.3 Immobilized lysozyme activity 54
V.1.5 Conclusions 56
V.2 Graphene oxide exfoliation and purification during the formation of cellulose acetate nanocomposites by supercritical CO_2 assisted phase separation 57
V.2.1 Preparation of CA/GO composite structures........................ 57
V.2.2 GO characterization.. 58
V.2.3 Polymer-GO nanocomposites... 61
V.2.4 Conclusions and perspectives... 70
V.3 3-D PLLA scaffolds formation by a supercritical freeze extraction assisted process.. 71
V.3.1 Preparation of PLLA scaffolds... 71
V.3.2 PLLA scaffold: results and discussion 71
V.3.3 Conclusions 79
V.4 3-D PLLA/Ibuprofen composite scaffolds obtained by a supercritical fluids assisted process... 79
V.4.1 Preparation of PLLA composite scaffolds 79
V.4.2 PLLA composite scaffold: results and discussion................ 80
V.4.3 Conclusions 92
V.5 Chitosan scaffolds formation by a supercritical freeze extraction process 93
V.5.1 Chitosan scaffolds preparation 93
V.5.2 Chitosan scaffolds: results and discussion 93
V.5.3 Conclusions 102
V.6 Complete Glutaraldehyde elimination during Chitosan hydrogel drying by SC-CO_2 processing 103
V.6.1 Preparation of Chitosan aerogel 103
V.6.2 Crosslinked Chitosan aerogel: results and discussion........ 104

V.6.2.1 Glutaraldehyde release from Chitosan aerogel 106
V.6.2.2 FTIR analysis 108
V.6.2.3 TGA analysis 109
V.6.3 Conclusions 110
V.7 FEM Modeling of the reinforcement mechanism of HA in PLLA scaffolds 111
V.7.1 Preparation of the composite scaffolds 111
V.7.2 Experimental results 111
V.7.2.1 Effect of HA nanoparticles percentage 111
V.7.3 FEM modeling and results 116
V.7.3.1 Modeling micrometric porous structure 116
V.7.3.2 Modeling the nanofiber network 120
V.7.3.3 Modeling of the filler (HA) 124
V.7.4 Discussion, conclusions and perspectives 127

CHAPTER VI. CONCLUSIONS 131

REFERENCES 133

LIST OF SYMBOLS 147

LIST OF FIGURES

Figure IV.1 Equipment used for the experimentation: (a) Photo, (b) P&ID... 29

Figure V.1 *Section of a CA membrane obtained starting from a 10% w/w CA solution. Process conditions 150 bar, 55°C*.. 37
Figure V.2 *Membrane obtained starting from a 10% w/w CA solution processed at 150 bar, 55 °C: (a) bottom surface; and (b) top surface* 38
Figure V.3 *Section of a CA membrane obtained starting from a 15% w/w CA solution. Process conditions 200 bar, 45 °C*.. 38
Figure V.4 *Pore size distribution in CA membranes obtained starting from a solution 15% w/w, processed at 55/150, 45/200, and 35/250 T/p*................ 39
Figure V.5 *Pore size distribution in CA membranes obtained starting from a solution 15% w/w, processed at 55/200, 45/200, and 35/200 T/p*................ 41
Figure V.6 *Section of a CA membrane obtained starting from a 20% w/w CA solution, taken at different enlargements: (a) 250 X; and (b) 1000 X. Process conditions 250 bar, 35 °C*.. 42
Figure V.7 *Pore size distribution in CA membranes obtained starting from a solution 20% w/w, processed at 55/150, 45/200, and 35/250 T/p*................ 43
Figure V.8 *Generic equilibrium diagram CA/acetone/SC-CO$_2$* 44
Figure V.9 *Thermograms of CA, lysozyme and CA plus lysozyme membranes processed at 200 bar, 45 °C*.. 46
Figure V.10 *EDX maps of a membrane at 20% w/w CA processed at 200 bar, 45 °C: (a) Carbon atoms in blue (i.e., CA) and (b) Sulfur atoms in red (i.e., lysozyme)*.. 47
Figure V.11 *Comparison among lysozyme release kinetics from membranes at 10, 15, 20% w/w CA, processed at: (a) 250 bar, 35 °C; (b) 200 bar, 45 °C; and (c) 150 bar, 55 °C*... 51
Figure V.12 *Comparison among enzymatic activities of mobile lysozyme from membranes at 10, 15, 20% w/w CA, processed at 200 bar, 45 °C* 53
Figure V.13 *Enzymatic activity of lysozyme immobilized in membranes processed at 200 bar, 45 °C at: 10%, 15% and 20% w/w CA* 55
Figure V.14 *Immobilized lysozyme activity of 20% w/w CA membrane, processed at 200 bar 45 °C, when the direct contact with the microorganism was replicated* 56
Figure V.15 *(A,B,D,E,F,G) TEM images of GO at different magnifications, (C) EDX spectrum taken in the area indicated with D*................................ 59
Figure V.16 *XRD of starting Graphite and of GO (A), GO Raman Spectrum (B)* 60
Figure V.17 *XPS - C 1s core level for GO* 60
Figure V.18 *TG-DTG-MS profiles for GO* 61

Figure V.19 *CA structures obtained at 200 bar 40 °C starting from 25% w/w CA/NMP solution: a) macroscopic view, b) FESEM analysis of the section, c) FESEM analysis of the top surface* 62
Figure V.20 *CA/GO structures obtained at 200 bar 40 °C starting from 25% w/w CA/NMP solution and 3% w/w of GO: a) macroscopic view, b) FESEM analysis of the section, c) FESEM analysis of the top surface* 63
Figure V.21 *CA/GO structures obtained at 200 bar 40 °C starting from 25% w/w CA/NMP solution and 9% w/w of GO: a) macroscopic view, b) FESEM analysis of the section, c) FESEM analysis of the top surface* 64
Figure V.22 *Pore size distribution in CA/GO composite structures obtained at different GO loadings* 65
Figure V.23 *TEM image of CA_GO_2_8h at different magnifications* 66
Figure V.24 *TG-DTG-MS profiles for CA (A), CA_GO_1 (B), CA_GO_2 (C), CA_GO_2_8h (D)* 68
Figure V.25 *TG-DTG-MS profiles for GO from CA_GO_2_8h after CA removal in NMP* 69
Figure V.26 *X-ray diffraction pattern of GO from CA_GO_2_8h, after a CA removal in NMP (A); Raman Spectra of GO, CA, CA_GO_1, CA_GO_2, CA_GO_2_8h (B) and GO, from CA_GO_2_8h, after a CA dissolution in NMP (C)* 69
Figure V.27 *Sections of PLLA scaffolds obtained starting from solutions at different polymer concentrations: (a) 5% w/w, (b) 10% w/w, (c) 15% w/w, (d) 20% w/w, phase separated at -30 °C and dried by SC-CO_2 at 35 °C and 100 bar* 72
Figure V.28 *Pore size distribution in PLLA scaffolds obtained starting from different polymer concentrations* 73
Figure V.29 *FESEM image at higher magnification of a 10% w/w PLLA scaffold, phase separated at -30 °C and dried by SC-CO_2 at 100 bar and 35 °C* 74
Figure V.30 *PLLA scaffold surfaces obtained starting from (a) 10% and (b) 20% w/w polymer concentration, processed at 100 bar and 35 °C* 74
Figure V.31 *L209s PLLA scaffold section dried at 100 bar and 35 °C, 15% w/w PLLA* 76
Figure V.32 *PLLA scaffold skin (20% w/w) obtained drying the structure at 250 bar and 35 °C* 76
Figure V.33 *Qualitative binary diagram for the system PLLA-Chloroform* 77
Figure V.34 *Qualitative ternary diagram for the PLLA/Chloroform/SC-CO_2 system* 78
Figure V.35 *Sections of PLLA/ibuprofen composite scaffolds obtained starting from solutions at different polymer concentrations: a) 5% w/w, b) 10% w/w, c) 15% w/w, phase separated at -30 °C and dried by SC-CO_2 at 45 °C and 150 bar* 81
Figure V.36 *Pore size distribution of PLLA/ibuprofen composite scaffolds obtained starting from different polymer concentrations* 82

Figure V.37 *FESEM image at higher magnification of a 15% w/w PLLA/ibuprofen composite scaffold, phase separated at -30 °C and dried by SC-CO_2 at 150 bar and 45 °C* 83
Figure V.38 *PLLA/ibuprofen composite scaffold surfaces obtained starting from a) 5% w/w, b) 10% w/w, c) 15% w/w polymer concentration, with 10% w/w of ibuprofen, dried at 100 bar and 45 °C by SC-CO_2* 84
Figure V.39 *EDX analysis of PLLA/ibuprofen composite scaffolds obtained at 150 bar and 55 °C; a) red: Carbon map, b) green: Sodium map* 85
Figure V.40 *PLLA/ibuprofen composite scaffolds obtained at 15% w/w of PLLA, 35 °C and at different pressures: (a) 100 bar; (b) 200 bar* 86
Figure V.41 *Pore size distributions of PLLA/iburprofen composite scaffolds obtained at 15% w/w of PLLA, 35 °C and at different pressures (100, 150 and 200 bar)* 87
Figure V.42 *PLLA/ibuprofen composite scaffolds obtained at 15% w/w of PLLA, 100 bar and at different temperatures: (a) 35 °C; (b) 55 °C* 88
Figure V.43 *Pore size distributions of PLLA/ibuprofen composite scaffolds obtained at 15% w/w of PLLA, 100 bar and at different temperatures (35, 45 and 55 °C)* 88
Figure V.44 *Ibuprofen release profiles from PLLA scaffolds with different polymer concentrations (from 5 to 15% w/w) obtained by supercritical drying at 150 bar and 45 °C* 89
Figure V.45 *Skin of 15% w/w PLLA scaffolds obtained at 200 bar and 45 °C, before (a) and after (b) the drug release* 90
Figure V.46 *Ibuprofen release profiles from scaffolds obtained starting from 5% w/w PLLA, at 35 °C and different pressures (a) and starting from 10% w/w PLLA, at 150 bar and different temperatures (b)* 92
Figure V.47 *Effect of chitosan concentration on scaffolds morphology obtained starting from water:acetic acid ratio 97:3: (a) 2% w/w, (b) 5% w/w, (c) 10% w/w* 95
Figure V.48 *Pore size distribution of chitosan scaffolds obtained starting from 5 and 10% w/w chitosan solutions with a water:acetic acid ratio of 97:3* 96
Figure V.49 *Nanofibrous sub-structure of pore walls in 10% w/w chitosan scaffolds obtained starting from solutions with water:acetic acid ratio of 97:3* 97
Figure V.50 *Top surface of 10% w/w chitosan scaffolds obtained starting from solutions with water:acetic acid ratio of 97:3* 97
Figure V.51 *Effect of acetic acid concentration on chitosan scaffolds obtained starting from 10% w/w chitosan solutions; water:acetic acid ratio of (a) 99:1 and (b) 95:5* 98
Figure V.52 *Pore size distribution of chitosan scaffolds obtained starting from 10% w/w chitosan solutions with different water:acetic acid ratio (99:1, 97:3, 95:5)* 99

Figure V.53 *Qualitative binary phase diagram "polymer concentration vs. temperature" for the system chitosan/acid water* 100
Figure V.54 *Qualitative modification of binary phase diagram changing acetic acid concentration* 101
Figure V.55 *hMSCs cultured for 2 (a) and 4 (b) days in osteogenic media. Live cells (stained green) and dead cells (stained red) on scaffolds obtained starting from 10% w/w of chitosan with 3% v/v of acetic acid* 102
Figure V.56 *FESEM images of Chitosan medium* M_w *(2% w/w): (a) CH aerogel section; (b) CH:GTA 16:1 aerogel section; (c) CH:GTA 8:1 aerogel section; (d) CH:GTA 4:1 aerogel section* 105
Figure V.57 *FESEM image of CH:GTA 4:1 aerogel surface*.................... 105
Figure V.58 *GTA release from CH aerogels 2% w/w* 107
Figure V.59 *FTIR spectra of pure CH and CH aerogels, 2% w/w crosslinked with GTA* 109
Figure V.60 *Thermogravimetric analysis of CH aerogel samples* 110
Figure V.61 *PLLA/HA scaffolds obtained by* $SC\text{-}CO_2$ *drying at 200 bar and 35 °C, with a-b) 10% w/w HA, c-d) 50% w/w HA*...................................... 112
Figure V.62 *PLLA scaffolds obtained by* $SC\text{-}CO_2$ *drying at 200 bar and 35 °C, a) 15% w/w PLLA, b) 15% w/w PLLA + 50% w/w HA, c) HA nanoparticles on the bottom of a PLLA micropore, 50% w/w HA* 114
Figure V.63 *HA nanoparticles distribution (measured through the Calcium atoms distribution - red) along the section of a PLLA scaffold with 30% w/w of HA* 115
Figure V.64 *hcp (left) and fcc (right) close-packing of spheres*................ 117
Figure V.65 *RVE FEM model (micrometric structure level): a) 3D view; b) Top view* 118
Figure V.66 *RVE showing a meshed tetrahedral space frame*.................. 121
Figure V.67 *Schematic example of a covered fiber section: on the left, relation between real fiber and FEM model; on the right, a detail of the contact between HA particles and PLLA fiber*... 125
Figure V.68 *Plateau effect of the Young's modulus with the increasing weight percentage of HA for a single fiber FEM model*............................. 126
Figure V.69 *Explanatory example of a cubic RVE of the nanostructured model: PLLA (blue elements); HA (yellow elements)* 127
Figure V.70 *Superposition of the numerical results on the experimental results* 128

LIST OF TABLES

Table IV.1 *Polymers used for the experimentation*.................................... 25
Table IV.2 *Solvents used for the experimentation*...................................... 25

Table V.1 *Membrane pore size analysis* 40
Table V.2 *Mobile lysozyme activity for CA membranes processed at 200 bar and 45 °C* 53
Table V.3 *Mean pore size of CA+GO structures obtained at different GO loadings*.. 65
Table V.4 *CH and GTA amounts used for the crosslinking reaction*........ 103
Table V.5 *Maximum GTA concentration measured in the release medium* 107
Table V.6 *Degradation temperature of CH aerogels crosslinked with GTA* 110
Table V.7 *Compressive modulus of PLLA scaffolds obtained with different HA contents*... 115

Abstract

This research is focused on the production of structures of biomedical interest using supercritical assisted processes: Supercritical freeze extraction, Supercritical gel drying and Supercritical phase separation. These processes have been selected to overcome the limitations of the traditional ones used in this field; indeed, they produce structures with a disordered microporosity, without an organization at nanometric level, with poor mechanical properties and with potential cytotoxic effect due to the residues of organic solvents and crosslinking agents. These problems reduce the efficiency of the cells culture on these structures in terms of adhesion, proliferation and differentiation in the tissue that it would to regenerate.

Therefore, during the experimentation, several polymers, of natural and synthetic origin, were tested for bone, tendon and vascular applications. In particular, in this thesis:

- synthetic and natural structures characterized by a micrometric porosity and wrinkled pore walls were produced by Supercritical freeze extraction process,
- in the case of polymer/drug composite structures, a homogeneous distribution and controlled release of the active compound was assured,
- aerogels starting from natural polymers, that mimic the tissue extracellular matrix at nanometric level were produced by Supercritical gel drying,
- bioactive materials were tested; in particular, graphene oxide exfoliation and purification, during the formation of cellulose acetate nanocomposites, was obtained by Supercritical phase separation,
- FEM Modeling was developed, confirming that mechanical properties of aerogels depend on how the nanofibrous network is connected in the space and that bending is the major mode of deformation of the network.

CHAPTER I. Introduction

I.1 Tissue engineering

Tissue engineering (TE) is the ensemble of techniques that have been proposed to repair diseased or damaged tissues or to replace and regenerate part of organs of the human body; many of them are still at the stage of research proposal or have moved to the first steps of development.

TE originates from reconstructive surgery used for the direct transplantation of a donor tissue to repair damaged tissues and organs. Many difficulties arise with direct transplantation, due to insufficient number of organ donors, rejection of the donor organ and pathogens transmission. An autogenic tissue transplant (using patient own cells) would address most limitations of the direct transplantation and avoid difficulties concerning rejection and pathogens transmission. Therefore, constructing a tissue-engineered replacement *in vitro* can be an excellent alternative to the direct transplantation of donor organs (Vacanti *et al.*, 1999; Fuchs *et al.*, 2001).

A crucial step of the *in vitro* replacement is the scaffold fabrication. An opportunity is to use decellularized tissues and has been largely used to create heart valves, epithelial tissue and blood vessels; however, these “natural” scaffolds suffer of several limitations, among all infections transmission and rejection.

It is also possible to propose scaffolds obtained as 3-D synthetic constructs which serve as temporary support to allow isolated cells to form a new tissue, before being transplanted to the host tissue. These are the structures we will discuss in this thesis. A biodegradable matrix with sufficient mechanical strength, optimized architecture and suitable degradation rate, could perform this objective. The temporary substitution of different biological materials (bones, cartilages, nerves, tendons, vessels, cardiac valves, skin and tissues for the gastrointestinal system) requires different structural characteristics; but, all tissues share a series of common characteristics that have to be simultaneously fulfilled:

- a highly regular and reproducible 3-D structure (macrostructure) similar to the tissue to be substituted;

- a very high porosity (exceeding 90%) and, in many cases, a large open pore geometry, that allows cells migration and reorganization (Ma, 2004). Porosity and pore interconnectivity, directly affect the diffusion of nutrients and the removal of metabolic wastes;
- a suitable pore size depending on the specific tissue to be replaced;
- the scaffold should present nano-structural surface characteristics that allow cell adhesion, the proper identification of the extracellular matrix (ECM), proliferation, migration and differentiation. Cells are generally submerged in a collagen matrix characterized by a fibrous nanostructure with fiber diameters ranging between 50 and 500 nm. As a consequence, a similar structure should be formed on the walls of the scaffold to allow cells adhesion and growth (Ma, 2004);
- mechanical properties to maintain the predesigned tissue structure and support the specific loadings applied to the original tissue; the correct values depend on the organs to be repaired;
- biodegradability, biocompatibility and a proper degradation rate, to match the rate of the neo-tissue formation; for this reason, it is very important the choice of the polymer and of its molecular weight, since biodegradability largely depends on these two characteristics;
- absence/reduction of the inflammatory response, mainly due to solvent residues and to degradation products. Chronic inflammation obstacles the neo-tissue formation.

All these specifications are simultaneously required to allow the colonization of the scaffold by stem or specialized cells and all the requirements have to be fulfilled to avoid apoptosis or necrosis of the delicate biological guests.

Many polymers have been tested for TE application. They are commonly divided in natural and synthetic polymers and their characteristics have been discussed in some specific reviews (Gunatillake *et al.*, 2003; Jagur-Grodzinski, 2006; Puppi *et al.*, 2010).

Several techniques have been proposed for scaffolds fabrication that include: fiber bonding, solvent casting, melt molding, solid free form fabrication, gas foaming, electrospinning and freeze drying, frequently combined with particulate leaching. Details about these processes can be found in specific reviews (Liu *et al.*, 2004; Ma, 2004).

However, conventional scaffold fabrication techniques suffer various limitations; particularly, it is very difficult to obtain simultaneously the macro, micro- and nanostructural characteristics that have been previously described. For example, it is difficult to obtain:

- large porosity together with a control of the pore diameter, of the pore connectivity and of the mechanical resistance;
- large porosity together with the nanometric pore surface that enhances cell adhesion and growth;

- complex 3-D structures; several techniques are limited to the production of thin disks or films;
- the removal of toxic solvents that are located deep inside the structure.

Supercritical carbon dioxide (SC-CO_2) assisted processes have been proposed in this field, starting from some pioneering works on supercritical foaming (Mooney *et al.*, 1996; Harris *et al.*, 1998). Besides SC-CO_2 assisted foaming, various other techniques have been used such as: supercritical assisted phase separation, supercritical gel drying, electrospinning in SC-CO_2.

The general aim of SC-CO_2 assisted techniques is to improve the traditional TE processes, using the characteristic properties of SC-CO_2 to control scaffolds morphologies thanks to the modulability of mass transfer properties, characteristic of dense gases and the specific thermodynamic behavior of gas mixtures at high pressure. An efficient solvent elimination can be obtained due to the large affinity of SC-CO_2 with almost all the organic solvents and short processing times are possible, taking advantage of the enhanced mass transfer rates.

I.2 Natural and synthetic polymers for biomedical applications

In biomedical applications, the criteria for selecting the biomaterials are based on their material chemistry, molecular weight, solubility, shape and structure, hydrophilicity/hydrophobicity, water absorption degradation and erosion mechanism.

Polymeric scaffolds are drawing a great attention due to their properties such as high surface-to-volume ratio, high porosity with very small pore size, biodegradation and mechanical properties. They offer advantages of biocompatibility, versatility and the biological properties which are significant in the application of TE and organ substitution. Naturally occurring polymers, synthetic biodegradable, and synthetic non-biodegradable polymers are the main kinds of polymers used as biomaterials.

Natural polymers can be considered as the first biodegradable biomaterials used clinically (Nair *et al.*, 2007). Natural materials have better interactions with the cells that allow them to enhance the cells' performance in biological system. They can be classified as proteins (silk, collagen, gelatin, fibrinogen, elastin, keratin, actin and myosin), polysaccharides (cellulose, amylose, dextran, chitin and glycosaminoglycans), or polynucleotides (DNA, RNA) (Ozdil *et al.*, 2014).

Synthetic polymers are highly useful in biomedical field since their properties (e.g., porosity, degradation time and mechanical characteristics) can be tailored for specific applications. Synthetic polymers are often cheaper than biologic scaffolds; they can be produced in large uniform quantities and have a long shelf time. Many commercially available synthetic polymers show physico-chemical and mechanical properties comparable to those of biological tissues. They exhibit, in general, predictable and reproducible mechanical and physical properties such as tensile strength, elastic modulus and degradation rate (Gunatillake *et al.*, 2006). PLA, PGA, and PLGA copolymers are among the most commonly used synthetic polymers in TE (Ma, 2004). PHA belongs to a class of microbial polyesters and is being increasingly considered for applications in TE (Chen *et al.*, 2002).

Bioactive ceramics, such as HA, TCP and specific compositions of silicate and phosphate glasses (bioactive glasses) and glass-ceramics (such as apatite-wollastonite) react with physiological fluids and through cellular activity form tenacious bonds to hard and in some cases soft tissue engineering (Hench, 1991). However, their biocompatibility and biodegradability are often insufficient, limiting their potential use in the clinical side. It is possible to overcome these issues by blending synthetic and natural polymers or by using composite materials that improve the scaffold properties and thereby allowing controlled degradation (Cascone *et al.*, 2001) and improving the biocompatibility in biomedical applications (Ciardelli *et al.*, 2005).

I.3 Three-dimensional polymeric scaffold fabrication and different kinds of scaffold

In an era of decreasing availability of organs for transplantation and a growing need for suitable replacements, the emerging field of TE gives hope to patients who require tissue and organ substitutes. Since 1980, researchers developed many novel techniques to shape polymers into complex architectures that exhibit the desired properties for specific TE applications. Typical scaffold designs included meshes, fibers, sponges and foams and so forth. These designs are chosen since they promote uniform cell distribution, diffusion of nutrients and the growth of organized cell communities (Freed *et al.*, 1998). Most techniques involve the application of heat and/or pressure to the polymer or dissolving it in an organic solvent to mold the material into its desired shape. While each method presents distinct advantages and disadvantages, the appropriate technique must be selected to meet the requirements for the specific kind of tissue.

To repair and regenerate lost or damaged tissue and organs, 3D scaffolds must be designed, fabricated, and utilized to regenerate the tissue similar in both anatomical structure and function to the original tissue or organ to be replaced or repaired. Therefore, different kinds of scaffold, including porous scaffold, microsphere scaffold, hydrogel scaffold, fibrous scaffold, polymer-bioceramic composite scaffold and acellular scaffolds have been developed.

I.3.1 Porous scaffolds

Sponge or foam porous scaffolds have been used in TE applications (Zhang *et al.*, 1999), especially for growth of host tissue, bone regrowth, or organ vascularization. Their porous network simulates the ECM architecture allowing cells to interact with their environment. Though foams and sponges are more mechanically stable compared to mesh structures, their use is still limited due to the open spaces present throughout the scaffold. A foam polymeric scaffold approach has several potential advantages for proliferating or adherent cell lines such as: (a) provide a physical surface onto which the cells can lay their own ECM, (b) may inhibit cell growth of adherent contact-inhibited cells, (c) provides improved nutrient transport to the center of the device through the porous interconnecting channel network, and (d) may limit cluster size to the pore size of the foam and thereby eliminating very large clusters that can potentially develop a necrotic center. Depending on the choice of solvent and phase separating conditions, the foams can be controlled to form either random or oriented pore architectures (Ma *et al.*, 2001b) and ideal pore sizes vary for different cells and tissues (Wei *et al.*, 2004).

I.3.2 Hydrogel scaffolds

The design and application of biodegradable hydrogels has dramatically increased the potential impact of hydrogel materials in the biomedical field and enabled the development of exciting advances in controlled drug delivery and TE applications (Cabodi *et al.*, 2005). Hydrogels, comprised of naturally derived macromolecules, have potential advantages of biocompatibility, cell-controlled degradability and intrinsic cellular interaction. They may exhibit batch variations and generally exhibit a narrow and limited range of mechanical properties. In contrast, synthetic polymers can be prepared with precisely controlled structures and functions.

Hydrogels in TE must meet a number of design criteria to work appropriately and promote new tissue formation. These criteria include both physical parameters (e.g., degradation and mechanics) as well as biological performance parameters (e.g., cell adhesion). Biocompatible hydrogels are currently used in cartilage wound healing, bone regeneration, wound dress and as carriers for drug delivery (Peppas *et al.*, 1993). They are often favorable for promoting cell migration, angiogenesis, high water content and rapid nutrient diffusion (Bryant *et al.*, 2001).

I.3.3 Fibrous scaffolds

The development of nanofibers enhanced the scope for fabricating scaffolds that can potentially mimic the architecture of natural human tissue at the nanometer scale.

Currently, there are three techniques available for the synthesis of nanofibers: electrospinning, self-assembly and phase separation. Electrospinning is the most widely studied technique and also seems to exhibit the most promising results for TE applications. The high surface-area-to-volume ratio of the nanofibers combined with their microporous structure favors cell adhesion, proliferation, migration and differentiation, all of which are highly desired properties for biomedical applications (Bhattarai *et al.*, 2004; Ma *et al.*, 2005). Nanofibers used as scaffolds for musculoskeletal TE including bone, cartilage, ligament and skeletal muscle, skin, vascular, neural TE and as vehicle for the controlled delivery of drugs, proteins and DNA (Vasita *et al.*, 2006). The blending technique is a common choice for the nanofiber functionalization. However, most of the polymer nanofibers do not possess any specific functional groups and they must be specifically functionalized for successful applications. The most popular and simplest nanofiber modification methods are physical blending and coating. Surface grafting polymerization has also been used for attaching ligand molecules and adhesive proteins on nanofiber surface for application of affinity membrane and TE scaffold, respectively.

I.3.4 Microsphere scaffolds

Microsphere scaffolds are largely used as drug delivery systems and in advanced TE applications such as gene therapy, antibiotic treatment of infected bone and so forth (Stephens *et al.*, 2000). The influence of nanotechnology on scaffold design and the possibility of sustained release formulations of growth factors via microspheres are showing promising developments.

Microsphere scaffolds are generally a polymer matrix used for drug encapsulation for the release of drugs at a relatively slow rate over a prolonged period of time (Berkland *et al.*, 2002). They offer several benefits, including ease of fabrication, control over morphology, physico-chemical characteristics and versatility of controlling the release kinetics of encapsulated factors (Berkland *et al.*, 2003). The methods used to produce microsphere-based scaffolds utilized heat sintering (Borden *et al.*, 2004; Yao *et al.*, 2005), solvent vapor treatment (Jaklenec *et al.*, 2008a; Jaklenec *et al.*, 2008b), solvent/nonsolvent sintering method (Nukavarapu *et al.*, 2008) or nonsolvent sintering technique (Singh *et al.*, 2008).

I.3.5 Polymer-bioceramic composite scaffolds

Development of composite materials for TE is attractive since their properties can be engineered to suit the mechanical and physiological demands of the host tissue by controlling the volume fraction, morphology and arrangement of the reinforcing phase (Rezwan *et al.*, 2006). Ceramics used in fabricating implants can be classified as nonabsorbable (relatively inert), bioactive or surface reactive (semi-inert) (Hench, 1993), and biodegradable or resorbable (non-inert) (Hentrich *et al.*, 1971).

Ceramics are known for their good compatibility, corrosion resistance and high compression resistance. Drawbacks of ceramics include brittleness, low fracture strength, difficulty to fabricate, low mechanical reliability, lack of resilience and high density. In recent years, researchers realized that ceramics and their composites can also be used to augment or replace various parts of body, particularly bone. The ceramics used for the latter purposes are classified as bioceramics. The combination of polymers and inorganic phases leads to composite materials with improved mechanical properties due to the inherent higher stiffness and strength of the inorganic material. Secondly, addition of bioactive phases to bioresorbable polymers can alter the polymer degradation behavior of the scaffolds (Blaker *et al.*, 2003; Kim *et al.*, 2005). Complications in the development of polymer bioceramics composite scaffold are: (i) maintenance of strength and the stability of the interface during the degradation period and replacement by the natural host tissue and (ii) matching resorption rates to the repair rates of body tissues developed for hard tissue implants and TE scaffolds, due to their excellent biocompatibility, bioactivity, and bioresorption in calcified tissue. The composite scaffolds support uniform cell seeding, cell ingrowth and tissue formation.

I.3.6 Acellular scaffolds

Acellular tissue matrices can be prepared by manufacturing artificial scaffolds or by removing cellular components from tissues by mechanical and chemical manipulation, to produce collagen-rich matrices (Dahms *et al.*, 1998; Yoo *et al.*, 1998; Chen *et al.*, 1999). These matrices slowly degrade on implantation and are generally replaced by the ECM proteins secreted by the ingrowing cells. The ultimate goal of any decellularization protocol is to remove all cellular material without adversely affecting the composition, mechanical integrity and eventual biological activity of the remaining ECM. Since the structures of the proteins (e.g., collagen and elastin) in acellular matrices are well conserved and normally arranged, the mechanical properties of the acellular matrices are not significantly different from those of native bladder submucosa (Dahms *et al.*, 1997).

Although various synthetic biodegradable polymer scaffolds have been developed and improved by mimicking biological structures, comparing to other scaffolds, acellular scaffolds have the following advantages:
(i) retain their correct anatomical structure even after the decellularisation process;
(ii) retain native ECM architecture and possess the cell adhesion ligands;
(iii) the decellularisation process reduces immunological responses by completely removing cellular components;
(iv) the decellularisation process facilitates similar biomechanical properties as those of native tissues that are critical for the long-term functionality of the grafts.

Various extracellular matrices have been utilized successfully for TE in animal models and products incorporating decellularized heart valves, small intestinal submucosa (SIS) and urinary bladder received regulatory approval for use in human patients (Gilbert *et al.*, 2006).

CHAPTER II. Supercritical Assisted Processes vs Traditional Processes for the Production of Materials of Biomedical Interest

II.1 Supercritical foaming

Traditional foaming techniques use a chemical agent that produces the gaseous compounds responsible of the formation of bubbles that, blocked into the polymer, produce a foam (Meng *et al.*, 2004). Foaming process is, in principle, simple and it is possible to achieve a relative control of pore diameter by calibrating the process parameters. However, it tends to produce prevalently closed pores structures; indeed, its standard industrial application is in thermal and acoustic insulation.

The supercritical homologous of this process uses SC-CO_2 to produce microcellular foams when released from the polymer. The main requirement of SC-CO_2 foaming process is that CO_2 should be dissolved in a sufficient amount in the polymer; this characteristic excludes, for instance, the use of polymers which have a low affinity for CO_2.

When compared to traditional foaming processes, SC-CO_2 based technique is characterized by larger mass transfer coefficients and by the tunability of the quantity of CO_2 dissolved in the polymer, via pressure and temperature variations; moreover, this process is solventless.

Supercritical foaming is based on the following steps: first, the polymer is saturated with the supercritical fluid at high pressure; second, the polymer/gas mixture is quenched into a supersaturated state by either reducing pressure or increasing temperature: bubble nucleation is produced; third, growth of the gas cells formed throughout the polymer sample is obtained. The driving force for bubble nucleation and growth is the temperature difference $T-T_g$ that is controlled changing the temperature by direct heating of the sample, or by manipulating T_g through process pressure.

Other process parameters that influence foam characteristics are the depressurization rate and the cooling velocity.

In the first applications of SC-CO_2 foaming, prevalently closed structures were obtained (Goel *et al.*, 1994; Arora *et al.*, 1998; Stafford *et al.*, 1999; Reverchon *et al.*, 2007a). This technique was used to produce foams of various polymers as poly(ether imide) (Krause *et al.*, 2002), poly(ether sulfone) (Krause *et al.*, 2002), atactic polystyrene (Stafford *et al.*, 1999), poly(methyl methacrylate) (Goel *et al.*, 1994), poly(ethylene-covinylacetate) (Jacobs *et al.*, 2004) and the effect of process parameters such as saturation pressure, processing time and temperature were in some cases investigated. For example, Reverchon and Cardea (Reverchon *et al.*, 2007a) proposed the foaming of polystyrene by SC-CO_2, obtaining very regular cellular structures. These authors also showed that the classical foaming theory could be applied also to the supercritical assisted process; in particular, two factors should be met during the depressurization step for generating uniform foams: the absorption of a sufficient amount of CO_2 to let pores nucleation and growth during the depressurization and the T_g of the polymer should be lower of the temperature used in the experiment. This second condition is also favored by T_g depression due to CO_2 adsorption.

Supercritical foaming has also been used to produce open-pore structures suitable for TE applications. This possibility was first proposed by Mooney et al. (Mooney *et al.*, 1996). They claimed that PLGA open porous structures could be obtained by this process, avoiding the use of organic solvents. The same research group (Harris *et al.*, 2001) in a subsequent work added to CO_2-foaming process a solid porogen (foaming/particulate leaching technique) to overcome the limited pore connectivity. There was no quantitative information about the obtained pores connectivity; but, the attempts of cultivating muscle cells for adhesion and proliferation put in evidence as an adequate cells growth was measured only on foam surfaces. Similar results were obtained by Sheridan et al. (Sheridan *et al.*, 2000) using various polymers and testing angiogenic factors delivery. Barry et al. (Barry *et al.*, 2006) prepared methyl-methacrylate structures by SC-CO_2 foaming, claiming that the degree of porosity and interconnectivity of the scaffolds can be controlled simply by modifying the depressurization rate of the process: scaffolds with a porosity around 81% and with good connectivity (57% open pores) were obtained according to these authors. Another typical characteristic of the foaming process is the formation of a continuous skin on the external surfaces; these authors tried to overcome this problem removing the foam skin; then, chondrocytes proliferation was studied, confirming an adequate adhesion and growth on the foams surface. Singh et al. (Singh *et al.*, 2004) used this process for PLGA foams generation; the authors claimed a large percentage of interconnected pores but field emission scanning electron microscope (FESEM) images proposed in this work, showed a reduced quantity of large interconnections. The apparent discrepancy between the two experimental evidences could be related to the presence of very small interconnection that are not evident in FESEM images; however, the interconnections useful for TE are the larger ones that should allow cells migration within the scaffold. Subsequently, Barry et al. (Barry *et al.*, 2005) tested other non-degradable polymers using the same procedures of a previous work (Barry *et al.*, 2006); again the authors indicated a large open pores percentage; but, FESEM images suggest that prevalently not largely connected structures were formed. In this case, neuroblastoma cultivation was proposed for some days (4-5) and the spread of the cells on the foam structure was observed. Mathieu et al. (Mathieu *et al.*, 2005) prepared bioresorbable ceramic-polymer composites using mixtures of PLA and ceramic compounds such as HA and TCP. The effect of process parameters was analyzed: slower cooling rates induced larger and more interconnected pores; ceramic particles tended to distribute on the pore walls of composite foams. The foams were also characterized by a mechanical point of view: higher compression resistance for composite structures was measured. Moreover, stem cells spread (after 2 weeks) on foams surface and moved across pores; they also started to differentiate in osteoblast lineage. An explanation of pores interconnection was also attempted: at lower viscosity, pores can grow for a longer time and pore walls have time to break, creating interconnections; however, only partial interconnection was observed and measured. Using ceramic fillers, more heterogeneous structures were obtained. Mathieu et al. (Mathieu *et al.*, 2006) processed the same composite to evidence anisotropy in foams morphology with pores oriented in the foaming direction. This characteristic could be useful in some TE applications where largely oriented tissue have to be regenerated. This anisotropy was also found in the mechanical behavior of the foams. Other authors (Jenkins *et al.*, 2006) applied SC-foaming technique to PCL. The effect of the depressurization time on the final microstructure of the foam was studied: it resulted in a combination of open and closed pores. The most interesting result was that, due to the partial (up to 70%) crystallization of the PCL foams, the inner surface presented a microtexture on pore surfaces; whereas, as a rule, foams present only smooth internal surfaces (Goel *et al.*, 1994). This characteristic could be of interest for cell adhesion. Tai el al. (Tai *et al.*, 2007) tested SC-foaming on PLGA copolymers of various composition and molecular weight. The effect of various processing parameters was studied (mainly temperature, pressure and processing times); again, partly interconnected structures were obtained, with non-porous skins. Luetzow et al. (Luetzow *et al.*, 2007) loaded PCL foams with a small model molecule. The main scope was to understand if molecules can be loaded in the polymeric structure and if their presence modifies the foam. Up to 43% w/w of this compound was loaded in the SC-CO_2 foamed polymer and crystals of dimensions up to about 3 mm were formed, that largely modified the structure. Velasco et al. (Velasco *et al.*, 2010) prepared partly degradable

PMMA + PLA structures by SC-CO_2 foaming and tried to incorporate ibuprofen. As in other SC-foaming works, they obtained a dense outer skin and a relative pores interconnectivity up to 64%. Cell culture was also attempted using human fibroblasts that were examined by FESEM. Ibuprofen was partly extracted during the process since it is partly soluble in SC-CO_2, as stated by the authors. The structures showed a good cells adhesion and proliferation after 7 days of culture.

Other authors tried to couple supercritical foaming with particulate leaching to induce the massive formation of open pores structures. The idea is that adequate quantities of a leachable material could contribute in breaking pore walls. Kim et al. (Kim *et al.*, 2006) produced PLGA/HA composite scaffolds by gas foaming + particulate leaching. Disks of 100-200 µm thickness, containing HA nanoparticles were generated using 90% w/w NaCl particles as pore opener. They obtained a highly open pore structure with no evidence of external non-porous layer and with an average compressive modulus of 4.5 MPa. Cells culture using rat calvarial osteoblasts was tested: an adhesion percentage of about 66% and osteoblasts growth in 4 weeks, corresponding to about 85% of cells increase, were obtained. They also attempted *in vivo* implantation of the osteoblast-seeded PLGA scaffolds and 8 weeks after the implantation they observed the formation of bone lamellar structures in the case of HA containing scaffolds. Salerno et al. (Salerno *et al.*, 2008) applied gas foaming plus microparticles leaching to PCL loaded with high quantities of NaCl microparticles (about 5 µm in diameter) and particularly concentrated their attention on 30/70 and 20/80 w/w PCL/NaCl composites. Subcritical CO_2 (65 bar) was used as the foaming agent. The large quantity of NaCl influenced the foaming process restricting the pores expansion, due to the increase in the composite stiffness; therefore, foams showed a decrease of pore size with NaCl percentage increase. Using microparticles concentration gradients, these authors were also able to induce a porosity gradient in the PCL structures. They induced about 100% open pores formation in PCL foams, starting at about 40% w/w NaCl. On the other hand, no quantitative indication were given about the mechanical properties of the structures after the leaching step, that could be influenced by the very high quantity of loaded microparticles. Mou et al. (Mou *et al.*, 2011) tested PLGA plus collagen plus HA by SC-foaming of tablets of different composition. They found that the expansion factor of the mixture decreased with the amount of collagen and HA; the influence of collagen was the most significant. Then, using 2.5% HA and 2.5% collagen, tested the effect of various process parameters like temperature, pressure and saturation time, measuring the average pore size and porosity. Mean pore sizes between 100 and 700 µm were observed and porosities ranging between about 48 and 92% were measured; however, no clear distinction between open and closed pores was presented. Cell attachment (max 93% after 4 h) and proliferation studies showed that human osteoblasts distributed throughout the foam as shown by FESEM and fluorescence images. This information was confirmed by chemical assays.

A particular and interesting application of dense CO_2 assisted foaming was presented by Dehghani and coworkers (Annabi *et al.*, 2009; Annabi *et al.*, 2010; Ji *et al.*, 2011). They were able to induce controlled foaming of elastin, elastin + tropoelastin and chitosan hydrogels, allowing CO_2 saturation, followed crosslinking under pressure. Chemical crosslinking (glutaraldehyde) was used to stabilize the hydrogel; then, the system was depressurized with the generation of bubbles that induced gas foaming. This process enhanced the porosity of the final structure, with respect to atmospheric pressure processing and was successful at lower temperatures (down to 4 °C in the case of chitosan) with the production of pores with average diameters ranging between about 25 and 80 µm depending on the biopolymer used. At higher temperatures $T > 23$ °C non-porous structures were obtained for chitosan due to the faster crosslinking of the hydrogel. Cells seeding (fibroblasts) on the hydrogels produced by the dense CO_2 assisted process was performed and their migration and growth was enhanced with respect to traditionally processed materials.

Summarizing, foaming process application to TE has the advantages that it is a very simple process and generally no solvents are required. On the other hand, the control of sample dimensions and shape is not easy, due to the large volume increase produced by foaming process and non-porous external skins can be generally formed. There is commonly a lack of interconnectivity between pores, that some authors tried to overcome using a massive microparticles loading (Salerno *et al.*, 2008; Salerno *et al.*, 2010) or blending with a second phase formed by a harder material, to break pores wall. Correspondingly, the structures obtained possess lower mechanical properties. The nanofibrous internal structure, that should mimic the natural ECM, is absent in this process; only when the polymer crystallization superimposes to foaming, rough internal pore surfaces can be produced that favor cells adhesion.

II.2 Supercritical assisted phase separation

Phase separation (PS) is obtained when a system formed by a polymer and a solvent becomes thermodynamically unstable and tends to separate into two phases: a polymer-rich and a polymer-lean phase. During the solvent removal, the polymer-rich phase solidifies. PS can be induced in several ways (Van de Witte *et al.*, 1996a); the two main techniques adopted are: thermal induced phase separation (TIPS) and solvent induced phase separation (SIPS). The most common process is the SIPS in which the polymer solution is casted on an inert support, that is, then, immersed into a bath filled with a second solvent in which the polymer is not soluble, but, forms a solution with the polymer solvent. The contact between the two solvents causes the formation of a liquid solution, followed by the phase separation with the formation of several different possible structures (Van de Witte *et al.*, 1996a). If process conditions have been properly selected, micrometric open pore structures are formed and, in some cases, non-porous skins are formed. These structures have been largely used as membranes (Van de Witte *et al.*, 1996a). PS processing is relatively simple, but, some limitations are present such as limited versatility in solvents combination, long processing times due to several post-treatments to wash the structure and the presence of residual solvents in the final product.

Phase separation techniques have been proposed to produce (prevalently bi-dimensional) scaffolds for TE applications (Lo *et al.*, 1995; Schugens *et al.*, 1996; Nam *et al.*, 1999). For example, the preparation of PLA biodegradable interconnected microcellular structures has been reported (Schugens *et al.*, 1996). Nam et al. (Nam *et al.*, 1999) found that isotropic open porous PLA scaffolds can be obtained by a coarsening effect in the TIPS process and tested the introduction of surfactants that act as porogen to enhance the pore size. The formation of PLGA scaffolds containing bioactive molecules has been also tested (Hua *et al.*, 2002).

The supercritical modification of the phase inversion process is based on the use of SC-CO_2 as the non-solvent. This alternative can overcome some limitations of the traditional processes. SC-CO_2 can dry the polymer rapidly, due to the enhanced mass transfer properties typical of supercritical fluids; moreover, the structure can be obtained without additional post-treatments, since the solvent used to dissolve the polymer is completely extracted. It is easy to recover the liquid solvent, since it dissolves in SC-CO_2 and can be removed from gaseous CO_2 by depressurization. SC-CO_2 processing allows to modulate the structure morphology and pore size changing pressure and temperature. Supercritical assisted phase separation (SC-PS) has been proposed for the formation of polymeric membranes to be used for several applications such as filtration processes (Cardea *et al.*, 2006), catalysis (Cardea *et al.*, 2011), drug controlled release (Reverchon *et al.*, 2006c; Duarte *et al.*, 2009b; Temtem *et al.*, 2009; Cardea *et al.*, 2010), etc.

The most relevant parameters in membranes formation by SC-PS resulted: polymer concentration, pressure, temperature and solvent type. In some cases, other process parameters have also been investigated such as the depressurization rate and the addition of another polymer in the starting solution (Temtem *et al.*, 2008). Depending on the process conditions and on the kind of polymer used, the four main morphologies characteristic of the conventional phase inversion were observed even on the same polymer (Reverchon *et al.*, 2004; Xu *et al.*, 2005; Reverchon *et al.*, 2006a; Reverchon *et al.*, 2007b; Temtem *et al.*, 2008). At given process conditions it is possible to observe dense, cellular and bicontinuous structures and particulate precipitation.

Some biopolymers have also been processed using this technique (Kim *et al.*, 2004; Cao *et al.*, 2005; Reverchon *et al.*, 2005b; Xu *et al.*, 2005; Reverchon *et al.*, 2006d; Temtem *et al.*, 2008). In some cases, the SC-PS process has also been explicitly proposed for the formation of structures potentially useful for scaffolding applications. Tsivintzelis et al. (Tsivintzelis *et al.*, 2007) reported the preparation of PLLA scaffolds in which montmorillonite (a nanostructured clay) was also added for the reinforcement of the polymeric matrix. Duarte et al. (Duarte *et al.*, 2009d) prepared porous structures of starch based polymers that presented a rough surface in which micro- and macropores were visible. This particular microstructure could enhance the transport properties and could also encourage cell attachment and proliferation. These matrices were also characterized by a highly interconnected porous structure. Using SC-PS, chitosan-PLLA blends (Duarte *et al.*, 2010) and starch-PLA blends loaded with dexamethasone (Duarte *et al.*, 2009c) were prepared. This compound can work as osteogenic medium to direct the differentiation of stem cells toward osteogenic lineage. The same authors (Duarte *et al.*, 2009a) tried to apply the SC-PS to PLLA scaffolds in which bioactive glass microspheres were added to increase the mechanical characteristics of the base structure. An *in vitro* bioactivity study was carried out using a simulated body fluid and the results showed that the presence of the bioactive glass induced the formation of a bone-like apatite layer, useful for TE applications. The main limitation of this technique is the difficulty to obtain 3-D structures, since flat porous structures can be obtained, as a rule. Moreover, the internal surfaces usually do not contain a nanostructure, except for the case of some semi-crystalline polymers (Reverchon *et al.*, 2006a) where the crystallization process induces the formation of nanostructures on the walls of the micrometric pores.

II.3 Processes based on solvent elimination by supercritical CO_2

Other processes that have been used to generate scaffolds are based on the elimination of liquid solvents from polymeric solutions/gels. They are: solvent casting + particulate leaching, ionic liquid-polymer mixture drying and gel drying.

II.3.1 Solvent casting + particulate leaching

This process involves casting of a polymer, dissolved in an organic solvent, around a suitable porogen, drying and solidification of the polymer by evaporation or lyophilization and the subsequent leaching of the porogen;

operating in this way, a porous polymeric structure is obtained (Murphy *et al.*, 2002; Hou *et al.*, 2003; Oh *et al.*, 2003; Wu *et al.*, 2005).

PLLA and PLGA scaffolds were prepared using sieved salt particles as porogen (Mikos *et al.*, 1994). Similar techniques utilized alternative biocompatible porogens, such as sugars (Holy *et al.*, 1999) and lipids (Hacker *et al.*, 2003). PLGA scaffolds were produced using spheres of paraffin as porogen (Zhang *et al.*, 2006); PLGA was first dissolved in acetone; then, the composite was pressed into a predesigned mold cavity and kept under pressure for 4 h at room temperature. After solvent evaporation, paraffin spheres were leached out by extraction with n-pentane for 24 h. The resulting PLGA porous scaffolds had a relatively ordered porous structure with well defined interconnectivity between the pores. The porosity ranged from 80 to 97%, adjusted varying the porogen content. Ma et al. (Ma *et al.*, 2001c) prepared highly porous PLLA and PLLA/HA composite scaffolds, that were seeded with osteoblastic cells and cultured *in vitro*. When PLLA scaffolds were used, the osteoblasts adhered primarily on the outer surface of the polymer; in contrast, the osteoblasts penetrated deeply into the PLLA/HA scaffolds and uniformly distributed inside the structure due to the capability of HA to promote the osteogenicity of the polymer (Zhang *et al.*, 2010). Bone-specific markers were expressed more abundantly in the PLLA/HA composite scaffolds.

The solvent evaporation or extraction and, in some cases, even the leaching of the porogen (for example, in the case of paraffin spheres) could be obtained by SC-CO_2 processing, obtaining a simple and more efficient elimination of the unwanted compounds. Positive aspects of this process are the possibility of obtaining controlled porosity and high interconnectivity. On the other hand, it is necessary to perform post-treatments on the scaffolds to eliminate the solvent, long processing times are required and the pores obtained presents smooth walls that can be not suitable for cellular adhesion.

II.3.2 Drying of ionic liquid-polymer mixtures

Some natural biopolymers, like chitin and chitosan, are very difficult to solubilize or even not soluble in common solvents; therefore, the possibility to dissolve them in ionic liquids (ILs) can represent a good opportunity for their application in various fields, included TE. ILs are organic salts that are liquids at room temperature, exhibit non-detectable vapor pressure and due to their polar characteristic can dissolve highly polar compounds.

The possibility to prepare cellulose porous structures using an IL has been demonstrated by Tsioptsias and Panagiotou (Tsioptsias *et al.*, 2008b). These authors used an IL, namely 1-n-butyl-3-methylimidazalim chloride, to form cellulose solutions containing PMMA microparticles and HA nanoparticles. The suspension were stored at room temperature for 24 h to allow gelation; then, the IL solvent was eliminated by immersion in water and methanol and PMMA microparticles were eliminated by leaching with dichloromethane, followed by vacuum distillation. The final result was an interconnected microporus cellulose structure.

In subsequent papers (Tsioptsias *et al.*, 2008c; Silva *et al.*, 2011), this technique was modified using SC-CO_2 to improve and modify the drying process that was also accompanied by foaming of the structure (Tsioptsias *et al.*, 2008a). For example, in the case of chitin (Silva *et al.*, 2011), this biopolymer was dissolved in 1-butyl-3-methylimidazalim acetate (BmimAc), a gel was formed, that was immersed in ethanol, to eliminate a large amount of BmimAc; then, the material was submitted to Soxhlet extraction followed by steps of supercritical extraction using mixtures of CO_2 and ethanol of different composition; at the end of the process, pure SC-CO_2 was used. Microporous chitin structures were obtained; supercritical assisted solvent elimination process was very efficient and very low cytotoxic levels were found on the processed materials.

II.3.3 Gel drying

Gel drying allows to obtain nanofibrous interconnected structures that can well reproduce ECM; but, the gel alone does not contain macropores large enough to favor cellular growth and diffusion along the scaffold. Therefore, particulate leaching is added to produce scaffolds with a large porous structure with controlled pore size and porosity. A combination of gel drying + particulate leaching has been proposed by Ma and Zhang (Ma *et al.*, 1999) that prepared nanofibrous structures of PLLA, PDLA and PLGA, taking advantage of the natural nanostructural characteristics of these gels. The process was performed in five steps: (1) polymer solubilization in a liquid solvent, (2) phase separation/gelation, (3) solvent extraction from the gel using water, (4) freezing, and then (5) freeze-drying under vacuum. They obtained a nanofibrous structure with an open porosity ranging from 93.8 to 98.5%; the diameter of the nanofibers was approximately 160 nm. Subsequently, the same authors (Zhang *et al.*, 2000) generated PLLA scaffolds combining the above described technique with particulate leaching to obtain, inside the fibrous structure, pores larger than 100 µm. Sugar spheres were used as porogen. In this way, they obtained scaffolds with different microporosities maintaining the nanofibrous structure. Wei and Ma (Wei *et al.*, 2006) tested the bioactivity of these PLLA scaffolds and demonstrated bone-like apatite deposition, throughout the scaffold immersed in a simulated body fluid (SBF). Preincorporation of nanosized hydroxyapatite eliminated the induction period and facilitated apatite growth in the SBF. Apatite growth primarily occurred on the surface of the pores, but not in the interior of the nanofibrous network. Hu et al. (Hu *et al.*, 2010) investigated the effect of nanofibrous PLLA scaffolds prepared by this technique on phenotype control of human aortic smooth muscle cells (HASMCs). A tubular PLLA scaffold, intended for blood vessel regeneration, was fabricated and cell seeding studies showed the cells distribution throughout the scaffold. It was found that PLLA scaffolds preferentially supported contractile phenotype of HASMCs under *in vitro* culture conditions, as evidenced by gene expression level of smooth muscle cells (SMCs) contractile markers, including smooth muscle myosin heavy chain, smoothelin and myocardin. Xie et al. (Xie *et al.*, 2011) tested these scaffolds with pluripotent stem cells (iPSCs). iPSCs were directed to differentiate into SMCs and cultured *in vitro*; data showed the expression of SMC specific marker genes, including myocardin and smoothelin. The scaffolds produced using this process show several advantages with respect to the ones produced using all the other techniques, such as controlled and large open porosity (> 90%), large internal surface areas, very large connectivity at micronic and nanometric level. In particular, this process assures the coexistence of the micro- and nano-structural characteristics that have been previously described. On the other hand, it presents also some limitations: first, it is performed in several steps, which make this process time-consuming (more than 1 week); second, it uses some organic solvents, that are difficult to be eliminated and that can be entrapped inside the nanometric network, compromising the subsequent growth of cells in the scaffolds; third, it is difficult to preserve three dimensional structure due to the surface tension of the liquid solvents during the drying step: the partial collapse of the porous structure is frequent.

To overcome these limitations, a SC-CO_2 assisted process for the production of scaffolds has been recently proposed (Reverchon *et al.*, 2008; Reverchon *et al.*, 2009). The process is similar to the previous one for several aspects; but, SC-CO_2 is used to eliminate the organic solvents in a simple and effective step. Reverchon et al. (Reverchon *et al.*, 2008) tested this process for the formation of PLLA scaffolds. They prepared PLLA gels starting from PLLA-dioxane-ethanol solutions and added fructose as the porogen; then, supercritical drying and water leaching were performed. Scaffolds with elevated porosity (> 90%) and with good mechanical properties with a compressive modulus up to 81 kPa were obtained. Moreover, the coexistence of the fibrous nanostructure together with micronic pores of controllable size was maintained without any collapse of the structure. Supercritical processing is shorter (8 h) when compared with the traditional technique and very small solvent residues have been found (< 5 ppm). This last aspect is very interesting; indeed, the possible inflammatory response of the hosting tissue strongly depends on the amount of residual solvent inside the scaffold. Subsequently, the same authors (Reverchon *et al.*, 2009) prepared PLLA-HA composite scaffolds inserting nanometric HA particles in the starting solution and analyzed the effect of HA content on the compressive modulus. The increase of the amount of HA in the gel improved mechanical properties of the structure; a compressive modulus higher than 100 kPa was obtained. Supercritical dried PLLA gel using porogen particles of different diameters were also tested, cultivating human Mesenchymal stem cells (hMSCs) in a perfusion bioreactor. Several tenths on 4 mm × 4 mm PLLA scaffolds with internal porosities of 100, 250 and 500 µm were tested in a 12 days study (Pisanti *et al.*, 2012). After 8 days, the maximum expression of ALP was obtained, especially in 250 µm diameter scaffolds, indicating the massive differentiation of the hMSCs in osteoblasts. Moreover, the scaffolds were uniformly colonized by the guest cells. In the same paper (Pisanti *et al.*, 2012), a longer term study of 24 days confirmed the results of the previous tests; moreover, bone morphogenic protein-2 (BMP-2) levels followed a similar trend as ALP protein, confirming the dependence on pore size. These results are very promising since not only gel dried + particulate leaching scaffolds possess all the characteristics required for TE; but, the synthetic structure induced the expected behaviors of migration, growth and differentiation of the guest cells inside all the scaffold. In conclusion, in SC-gel drying the time consuming steps related to solvents exchange and extraction are substituted by a very fast supercritical process performed at zero surface tension. The collapse of the gel structure is avoided, since SC-CO_2 rapidly forms supercritical mixtures with many organic compounds at temperatures and pressures (for example, at 100 bar and 40 °C) readily obtainable from the processing point of view and especially temperatures are compatible with the thermal stability of polymers. Moreover, it is possible to have an accurate reproduction of the shape and 3-D structure of the tissue to be substituted.

II.4 Electrospinning in supercritical CO_2

Electrospinning (ES) is a process that uses an electric field to control the formation and deposition of polymer fibers onto a target substrate. A polymer solution or melt is injected with an electrical potential to create a charge imbalance. When a sufficiently high voltage is applied to the liquid, it becomes charged and electrostatic repulsion counteracts the surface tension and the liquid is stretched; at the critical point a stream of liquid erupts from the surface, producing the so-called Taylor cone. If the molecular cohesion of the liquid is sufficiently high, stream breakup does not occur and a charged liquid jet is formed. The jet is directed by the electric field toward the ground target; during the travel to the target, the solvent evaporates and fibers are formed. The number of investigations devoted to scaffolds preparation for TE by electrospinning is large (Luu *et al.*, 2003; Shields *et al.*, 2004; Zhong *et al.*, 2007; Wang *et al.*, 2010; Jha *et al.*, 2011). The spectrum of electrospun materials used to prepare nanofiber-based scaffolds for TE is broad. Biocompatible and biodegradable polymers of natural and synthetic origin such as PGA, PLLA, PCL, as well as copolymers from the corresponding monomers, polyurethanes, polyphosphazenes, collagen, gelatin and chitosan are only some examples (Luu *et al.*, 2003; Wang *et al.*, 2010).

Furthermore, synthetic polymers such as PLLA or PCL mixed with or coated with natural polymers such as gelatin or chitosan, or even grafted with such systems, have been used for the realization of fibrous scaffolds by ES; the aim of such modifications being to produce surfaces with enhanced adhesion and proliferation capability for cells. A broad spectrum of cells have been seeded on electrospun scaffolds, among them: hMSCs, neural stem cells, keratinocytes, cardiomyocytes, chondrocytes, smooth muscle cells, fibroblasts, osteoblasts and endothelial cells are just a few examples, and the target tissue included skin, bone, cartilage, neural tissue, heart, blood vessel and lung tissue (Zhong *et al.*, 2007; Nandakumar *et al.*, 2010; Wang *et al.*, 2010; Jha *et al.*, 2011). Generally speaking, the success of the electrospinning technique for TE applications is due to the relative simple procedure and the capability of generating nanometric and micrometric fibrous structures that could resemble the ECM.

With the aim of overcoming the performance of the classical electrospinning process, a supercritical fluids assisted electrospinning was proposed in which the electrospinning chamber was filled with SC-CO_2 (Levit *et al.*, 2004). SC-CO_2 in the chamber softened the polymer, reducing its viscosity thus, aiding the production of polymer fibers. The authors found that it was possible to form PDMS and PLA fibers within a thermodynamic window where the polymer has been softened, but not dissolved by SC-CO_2. As an additional advantage, SC-CO_2 reduces the polymer viscosity at temperatures lower than those necessary when melt processing is used. A similar procedure was proposed by Lee et al. (Lee *et al.*, 2007). PVP was electrospun in presence of SC-CO_2 obtaining fibers ranging between 400 and 900 nm. SC-CO_2 presence not only fastened the elimination of solvents (avoiding post-processing), but, increased the “quality” of the fibers, avoiding the formation of beads; i.e., of polymer nodules along the fibers. McHugh et al. (McHugh *et al.*, 2007) described the application of near-critical and supercritical CO_2 at the electrospinning processing, to create fibers with novel morphologies, obtained adjusting operating pressure and temperature. When electrospinning into a CO_2-rich bath was performed, an open-pore PVP fiber morphology was created, whose characteristics depended on the operating pressure.

In conclusion, electrospinning is one of the processes most frequently proposed for TE applications; it is especially suitable to produce flat structures; but, some crucial problems characterize the structures obtained: mainly, the mechanical resistance, control of the structural porosity and solvent residues.

Supercritical fluid assisted electrospinning is still a “young” process: its advantages are faster and complete solvent elimination and the possibility to produce porous filaments.

CHAPTER II

CHAPTER III. Aims of the Thesis

The aim of this research is the production of porous biopolymeric structures for biomedical applications, using green processes based on SC-CO_2.

During this work, the goals are:

- ✓ to test natural and synthetic polymers, alone and/or blended, for the production of new biopolymeric structures characterized by a micro and nanoporous morphology, suitable for the biomedical field;
- ✓ to load these structures with active compounds improving their performace from a biological and mechanical point of view;
- ✓ to produce safety biopolymeric structures; i.e., organic solvent and crosslinking agent residues free;
- ✓ to model the mechanical behavior of micro and nanoporous structures filled with a reinforcement for TE applications.

To obtain these different structures, with specific morphological and physico-chemical characteristics and proper shape, the parameters that mainly affect the processes tested will be studied.

CHAPTER III

CHAPTER IV. Materials and Methods

IV.1 Materials

In this work, various polymers and solvents are tested. An inventory of used polymers and solvents during the experimentation is supplied in Table IV.1 and Table IV.2, respectively.

Table IV.1 *Polymers used for the experimentation*

Polymer	*Supplier*
Cellulose Acetate	Sigma-Aldrich
PLLA	
L207s	Evonik
L209s	Evonik
Chitosan	Sigma-Aldrich

Table IV.2 *Solvents used for the experimentation*

Solvent	*Purity [%]*	*Boiling Point [°C]*	*Supplier*
Acetone	99.5	56	Sigma-Aldrich
N-methyl Pyrrolidone (NMP)	99.5	202	Sigma-Aldrich
Chloroform	99.0	61.5	Sigma-Aldrich
Acetic Acid	99.9	118	Sigma-Aldrich
Ethanol	99.8	78	Sigma-Aldrich

IV.1.1 Cellulose acetate (CA)

Cellulose is a naturally occurring material found in wood, cotton, hemp and other plant-based materials. It consists of repeating anhydroglucose units joined by β-(1,4) linkages, forming the basic repeating unit.

Although the primary use of cellulose films has been for wrapping purposes, it has also found an application in the treatment of renal failure, as well as in a variety of more recent clinical applications, such as for scaffolds in TE, temporary skin substitute, a haemostatic agent, post operative adhesion barrier and as a culture material for hepatocytes (Hoenich, 2007).

IV.1.2 PLLA

Poly(l-lactic) acid (PLLA) is one of two isomeric forms of poly(lactic acid): d(−) and l(−). Similar to PGA, PLLA is classified as a linear poly(*α*-hydroxy acid) that is formed by ring-opening polymerization of l-lactide. PLLA is structurally similar to PGA, with the addition of a pendant methyl group. This group increases the hydrophobicity and lowers the melting temperature to 170 to 180 °C for PLLA. PLLA typically undergoes bulk, hydrolytic ester-linkage degradation, decomposing into lactic acid. The body is thought to excrete lactic acid in the form of water and carbon dioxide via the respiratory system. The hydrophobic nature of PLLA allows for protein absorption and cell adhesion making them suitable as scaffolds (Garlotta, 2001).

IV.1.3 Chitosan

Chitosan is a linear copolymer of β-(1-4) linked 2-acetamido-2-deoxy-β-d-glucopyranose and 2-amino-2-deoxy-β-d-glycopyranose. It is obtained by deacetylation of chitin, a polysaccharide widely distributed in nature (e.g., crustaceans, insects and certain fungi) (Muzzarelli, 1973). Chitosan as an artificial variant of chitin is more suitable for useful bioapplications; the positive facets of excellent biocompatibility and biodegradability with ecological safety and low toxicity with versatile biological activities such as antimicrobial activity and low immunogenicity have provided ample opportunities for further development (Mourya *et al.*, 2008; Rinaudo, 2008).

IV.1.4 Lysozyme

Lysozyme is an antimicrobial compound, single peptide protein, which possesses enzymatic activity against beta 1-4 glycosidic linkages between N-acetylmuramic acid and N-acetylglucosamine found in peptidoglycan of the bacteria (Conte *et al.*, 2007).

IV.1.5 Graphene oxide

Graphene oxide (GO) was prepared according to the modified Hummers method. In a typical procedure, graphite (1.0 g) was mixed with 23 mL of H_2SO_4 (95%) and the mixture was stirred for 30 min within an ice bath. Potassium permanganate (3.0 g) was added very slowly to the suspension, with vigorous stirring, while maintaining a reaction temperature of 20 °C. The ice bath was removed and the reaction mixture was stirred overnight at 35 °C. Then, water was added to the pasty solution with constant agitation: the colour of the solution changed to yellowish brown. After 2 h of vigorous stirring, 25 mL of 30% H_2O_2 were added and immediately the colour of the solution turned to golden yellow. The mixture was washed several times with 5% HCl and, then, with deionized water, until the solution become acid free. At the end of the process, the reaction mixture was filtered and dried under vacuum at 65 °C.

IV.1.6 Ibuprofen

Ibuprofen [2-(p-isobutylphenyl)propionic acid] is an anti-inflammatory agent. It has been widely used orally, intravenously and even topically, for example, in postoperative conditions, where an immediately available dose might be useful or required. However, only recently specific studies on ibuprofen loading into and release from porous scaffolds have been reported (Cantón *et al.*, 2010; Cardea *et al.*, 2014b).

IV.1.7 Hydroxyapatite

Hydroxyapatite (HA) is a naturally occurring mineral form of calcium apatite. HA is chemically similar to the mineral component of bones and hard tissues in mammals. It is one of few materials that are classed as bioactive, meaning that it will support bone ingrowth and osseointegration when used in orthopaedic, dental and maxillofacial applications (Ma, 2008).

IV.2 Equipment

The home-made equipment used for the experimentation, is shown in Figure IV.1.

a

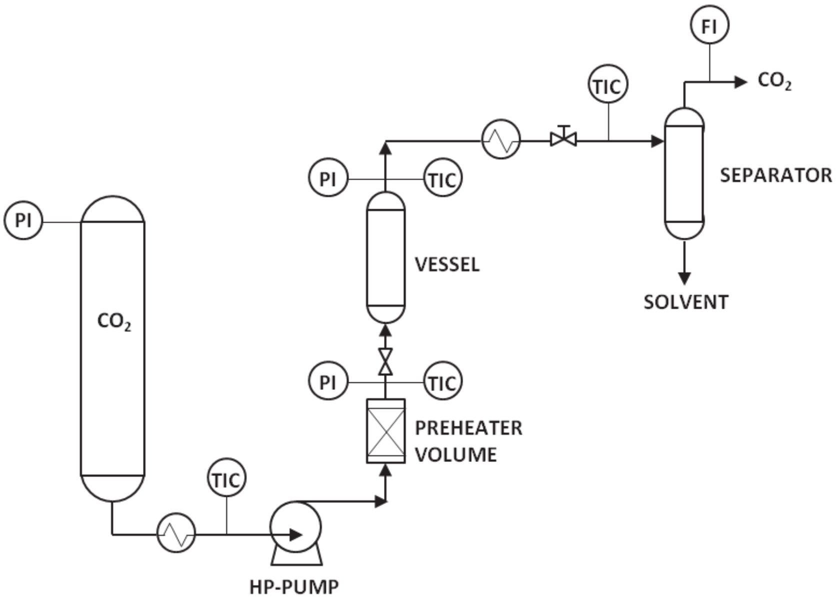

b

Figure IV.1 Equipment used for the experimentation: (a) Photo, (b) P&ID.

The apparatus is supported by a steel skid created *ad hoc* (Figure IV.1a). The parts, which constitute the equipment, are (Figure IV.1b):

- CO_2 tank farm
- cryostat
- high pressure membrane pump
- preheater volume equipped with band heaters
- 316 stainless steel cylindrical high-pressure vessel equipped with band heaters
- micrometering valve
- solvent separator
- rotameter
- manometer
- temperature controllers.

IV.3 Supercritical assisted phase separation

In the supercritical assisted phase separation process, SC-CO_2 is the non-solvent that induces the phase separation of the polymer solution. Compared with the wet phase inversion method, advantages of this phase separation process can be:

- SC-CO_2 can dry the polymer membrane rapidly and totally without the collapse of the structure due to the absence of a liquid-vapour interface. The dry membrane can be obtained without additional post-treatment because there are no traces of organic solvents.
- It is easy to recover the solvent; the solvent dissolved in SC-CO_2 can be removed from gaseous CO_2 in a separator located downstream the membrane formation vessel.
- CO_2 is not toxic, not flammable and cheap (Reverchon *et al.*, 2004).

IV.4 Supercritical freeze extraction process

Supercritical Freeze Extraction Process (SFEP) combines the advantages of TIPS process for phase separation and 3-D structures formation, followed by immediate supercritical drying that can produce complete and fast solvent elimination avoiding structure collapse, because the process is carried out with a negligible surface tension of the supercritical mixture (organic solvent + CO_2) (Cardea *et al.*, 2014a).

IV.5 Supercritical gel drying

Supercritical gel drying is a new process that allows the drying of gels through the formation of a supercritical solution between CO_2 and the liquid solvent. The supercritical mixture shows no surface tension and can be easily eliminated in a single step by the continuous flushing of SC-CO_2 in the drying vessel (Reverchon *et al.*, 2008).

IV.6 Analytical methods

IV.6.1 Field Emission Scanning Electron Microscopy (FESEM)

To perform FESEM, samples were cryo-fractured using liquid Nitrogen; then, they were sputter coated with Gold (Agar Auto Sputter Coater mod. 108 A, Stansted, UK) at 30 mA for 160 s and analyzed using a FESEM (mod. LEO 1525, Carl Zeiss SMT AG, Oberkochen, Germany), to evidence the micro and nanostructure and to measure the diameter of the fibers forming the structure of the samples.

IV.6.2 Transmission Electron Microscopy (TEM)

TEM images were acquired using a FEI Tecnai, The Netherlands electron microscope, operating at 200 kV with a LaB_6 filament as the source of electrons, equipped with an Energy Dispersive X-ray Spectroscopy (EDX) probe.

IV.6.3 Structure pore size analysis

Sigma Scan Pro 5.0 (Jandel Scientific, San Rafael, CANADA) and Origin 8.5 (Microcal, Northampton, USA) softwares were used to determine the average diameter of pores in the structure. Images taken at various locations in the structure were used for each calculation. We measured about 300 pores for each sample analyzed. Using Origin software, we first represented a histogram with the percentage of the pores having a given diameter; then, we performed a curve fitting to obtain the distribution curve.

IV.6.4 Structure porosity

Porosity (ε), that represents the “void space” of the structure, was calculated using an Ultrapycnometer 1000 (Quantachrome instruments, Florida, USA).

IV.6.5 Differential Scanning Calorimetry (DSC)

DSC (DSC 30 Mettler, Toledo) was carried out to analyze and identify any change in the thermograms of pure substances compared to sample formulations.

IV.6.6 Thermogravimetric Analysis (TGA)

The thermal decomposition behavior was investigated using a thermo-analyzer (Q600, TA Instruments) online connected to a quadrupole mass detector (Quadstar 422, Pfeiffer Vacuum, USA). The measurement was carried out in 1% v/v O_2 in Nitrogen and in air flow.

IV.6.7 X-Ray Diffraction (XRD)

XRD measurements (Bruker D8 X-ray diffractometer, USA) were performed with CuKα radiation. The measurements were performed on the thin Carbon film obtained after filtration.

IV.6.8 Raman spectroscopy

Raman spectra were obtained at room temperature with a microRaman spectrometer (Renishaw inVia, UK, 514 nm excitation wavelength).

IV.6.9 Energy dispersive X-ray spectroscopy (EDX)

Samples were cryofractured using liquid nitrogen and sputter coated with chrome (EMITECH K575X peltier cooled); then, they were analyzed by EDX (INCA Energy 350, Oxford Instruments) to identify the elements that constitute the samples.

IV.6.10 Fourier Transform Infrared Spectroscopy (FT-IR)

FT-IR spectra were recorded using a Thermo Nicolet Nexus Spectrometer (Rodano (MI), Italy), equipped with ATR (Attenuated Total Reflection) sampling, working with a Zinc selenide crystal.

IV.6.11 Solvent residue analysis

Organic solvent residues were measured by a headspace (HS) sampler (mod. 7694E, Hewlett Packard, USA) coupled to a gas chromatograph (GC) interfaced with a flame ionization detector (GC-FID, mod. 6890 GC-SYSTEM, Hewlett Packard, USA). The solvent was separated using two fused-silica capillary columns connected in series by press-fit: the first column (mod. Carbomax EASYSEP, Stepbios, Italy) connected to the detector, 30 m length, 0.53 mm i.d., 1 µm film thickness and the second (mod. Cp Sil5CB CHROMPACK, Stepbios, Italy) connected to the injector; 25 m length, 0.53 mm i.d., 5 µm film thickness. GC conditions were the one described in the USP 467 Pharmacopea with some minor modifications:

oven temperature from 45 °C to 210 °C for 15 min. The injector was maintained at 135 °C (split mode, ratio 4:1) and helium was used as the carrier gas (5 mL/min). Head space conditions were: equilibration time, 30 min at 95 °C; pressurization time, 0.15 min, and loop fill time, 0.15 min. Head space samples were prepared in 20 mL vials filled with internal standard DMI (3 mL) and 500 mg of NaCl and water (0.75 mL) in which samples were suspended.

IV.6.12 Mechanical test

Compressive mechanical properties of the scaffolds were measured using an INSTRON 4301 (Instron Int. Ltd, High Wycombe, UK) instrument. Cylindrical samples with a diameter of 2 cm and a thickness of 4 mm were compressed at a cross-head speed of 1 mm/min. The modulus was measured from the slope of the initial linear portion of the stress-strain curve.

IV.6.13 In vitro release assay

In vitro release rate assays were performed to determine the release kinetics of the interest compound from the porous structures. The different methods will be subsequently described for each system analyzed. At predetermined time intervals, the concentration of the interest compound was assayed using a UV-Vis spectrophotometer (Varian, mod. Cary 50 Scan, Palo Alto, USA).

IV.6.14 Cells culture

Dried samples were cut, using a surgical blade, to obtain scaffolds of 5 mm in diameter and 4 mm height. The samples size was imposed by the bioreactor dimension. To avoid the shrinkage of the nanostructure, the samples were cut using a blade previously immersed in liquid nitrogen. They were stored in refrigerator until used to prevent any possible degradation of the polymer. Subsequently, the scaffolds were sterilized in 70% ethanol; then, they were soaked for 30 min intervals, repeated four times, in sterile phosphate buffered saline solution (Fisher Scientific, Pittsburgh PA) to remove ethanol and to keep pH at a nearly physiologic value (physiological pH = 7.4). Sterilized scaffolds were soaked in DMEM supplemented with 10% fetal bovine serum for 4 h. hMSCs were removed from tissue culture flasks using trypsin/EDTA and pelleted via centrifugation at 500 × g for 5 min. The cells pellet was then resuspended at a density of 1.2 × 107 cells/mL to prepare the solution for seeding. Scaffolds were removed from DMEM and seeded with 10 µL of the solution (1.2 × 105 cells/scaffold) via pipetting directly on the scaffold surface. The scaffolds were, then, put in an incubator for 4 h, without media to allow cell attachment on the scaffolds surface. On study day -1 (cell seeding day), all cell seeded scaffolds were cultured in static into well plates using control media for 24 h, to facilitate the cell adhesion. A “Live/Dead” cell viability assay was performed to assess hMSC viability: cell viability and proliferation were investigated at days 2 and 4 following a previous study (Betz *et al.*, 2008). The principle of the live/dead assay is that membrane-permeantcalcein-AM is cleaved by esterases in live cells yielding cytoplasmic green fluorescence, and membrane-impermeant ethidiumhomodimer-1 labels nucleic acids of membrane-compromised cells produce red fluorescence. Thus, live cells display green fluorescence, and dead cells display red fluorescence. On days 2 and 4, cell culture media was removed and the specimen was washed with Dulbecco’s phosphate-buffered saline (pH = 7.2). Two milliliters of media (without serum) containing 0.002 mmol/L calcein-AMand 0.002 mmol/L ethidium homodimer-1 (both from Invitrogen, Carlsbad, CA) was added to each specimen. The cells were observed using epifluorescence microscopy (Nikon Eclipse TE-2000S, Melville, NY). The percentage of live cells was measured according to the definition: as PLIVE = NLIVE/(NLIVE + NDEAD), where NLIVE = number of live cells and NDEAD = number of dead cells, in the same image. Ten specimens of each material were tested (n = 10). Two randomly chosen zones of view were photographed from each specimen for a total of 20 photos.

CHAPTER V. Results and Discussion

V.1 Cellulose acetate + Lysozyme

The aim of this work is the production of CA membranes loaded with lysozyme, used as model compound, by SC-CO_2 assisted phase separation.

As previously discussed, this technique allows to control the morphology and porosity of the membranes obtained, and, therefore, can also allow the control of lysozyme release times. Enzyme unfolding can be preserved during processing maintaining small water quantities in the membrane.

The processing times are short and negligible organic solvent residues are present in the produced membranes.

Lysozyme loaded membranes will be characterized in terms of porosity, enzyme release and activity against *Micrococcus lysodeikticus*, used as a model microorganism.

V.1.1 Enzymatic membranes preparation

Polymer solutions were prepared by solubilizing CA in acetone; the solution containing lysozyme and water was separately prepared and, then, poured in the polymeric solution and mixed for 40 min. Solutions with CA contents of 5, 10, 15 and 20% w/w, and a fixed quantity of 1.5% w/w lysozyme and 5% w/w water were prepared. The solution was distributed on stainless steel caps, with a diameter of 2 cm and a height of about 800 μm, and, then, processed. Membranes were produced in a home-made laboratory apparatus described in the Chapter IV. When operative temperature was reached, the caps were rapidly put inside the membrane preparation vessel (a 316 stainless steel vessel with an internal volume of 80 mL) to minimize the evaporation of the solvent. The vessel was closed and filled from the bottom with SC-CO_2 up to the desired pressure, using a high pressure pump (MiltonRoy-Milroyal B, Pont-Saint-Pierre, France) in about 10 min. Then, the vessel was flushed with CO_2 for 3 h, and, depressurized in about 30 min, collecting the dried membranes.

V.1.2 Effect of process parameters on enzymatic membranes morphology

Supercritical assisted phase separation differs from the traditional phase inversion process since compressed CO_2 is used as the non-solvent, instead of a liquid. It has several advantages, mainly membrane properties could be modulated changing process conditions (Reverchon *et al.*, 2004; Reverchon *et al.*, 2005a; Cardea *et al.*, 2010), the resulting membrane does not require further processing since all the solvents are removed by SC-CO_2 and the process is very short. This last characteristic also improves membranes symmetry (Reverchon *et al.*, 2004).

In this work, the experiments have been performed by directly adding lysozyme and 5% w/w of water to the polymer-acetone solution. The addition of small quantities of water is mandatory to allow the enzyme to maintain its unfolding; i.e., when lysozyme molecules are surrounded by water molecules, they can maintain their original active structure (unfolding) even in a non aqueous environment (acetone) and enzyme denaturation (deactivation) can be avoided. But, water is a solvent that shows a very reduced affinity with CO_2 at the ordinary supercritical conditions used for polymer and active compounds processing (Sabirzyanov *et al.*, 2002), therefore, only small percentages of water can be added to acetone and its influence on the supercritical assisted phase inversion has to be verified.

Various series of experiments have been performed. In all of them, 1.5% w/w of lysozyme and 5% w/w of water have been added to the acetone-CA solution and CA concentration has been varied from 5 to 20% w/w (with respect to the total solution); temperatures between 35 and 55 °C and pressure between 150 and 250 bar have been tested.

The first relevant result is that the presence of water and of lysozyme at the percentage used in this work does not largely interfere with SC-CO_2 phase separation of the CA-acetone solution; indeed, in all the experiments performed in this study, formed and dried membranes have been obtained.

The second relevant result is that all structures, produced using 5% w/w CA in the starting solution, are formed by microparticles; thus, they did not fulfill the required characteristics of compactness and, therefore, they have been discarded in the following of this study.

The third consideration is that it is possible to study the different CA membranes considering the influence of single parameters like CA concentration, pressure and temperature on membranes morphology; but, the analysis of results suggests that in this case the different morphologies observed are mainly controlled by polymer concentration in the starting solution. Indeed, microparticulate membranes have been obtained at CA percentages of 5% w/w, whatever the other process conditions (p and T); membranes characterized by large finger structures have been obtained in the case of 10% w/w CA and cellular membranes have been produced at 15 and 20% w/w of CA.

CA concentration also influenced the morphology of the membranes surface. Increasing CA content in the starting solution, the top surface modified from beads-like (5% w/w), to partially porous (10% w/w), to dense with isolated pores (15-20% w/w), whereas the bottom surface modified from bicontinuos with microparticles (5% w/w), to cellular (10% w/w) to dense with isolated pores (15-20% w/w).

Therefore, in this study we will discuss the morphologies/pore sizes as depending on CA concentration in the forming solution. The sequences that will be highlighted are 35/250, 45/200 and 55/150 T/p, corresponding to SC-CO_2 densities of 0.90, 0.81 and 0.66 g/cm^3, respectively. This set of membranes has been chosen since it better describes the effect of SC-CO_2 density on the final morphology.

V.1.2.1 CA concentration 10% w/w

At all tested process conditions, when a solution with a starting concentration of CA at 10% w/w was been used, fingers were observed along the section of the membrane. An example of this morphology is given in Figure V.1, where a FESEM image of a CA membrane produced operating at 150 bar and 55 °C is shown. Fingers occupy a large part of the whole membrane section. Of course, for this kind of membranes, no cells diameter analysis has been possible. However, changing process conditions from 150 bar and 55 °C to 250 bar and 35 °C, smaller fingers have been observed along the membrane section.

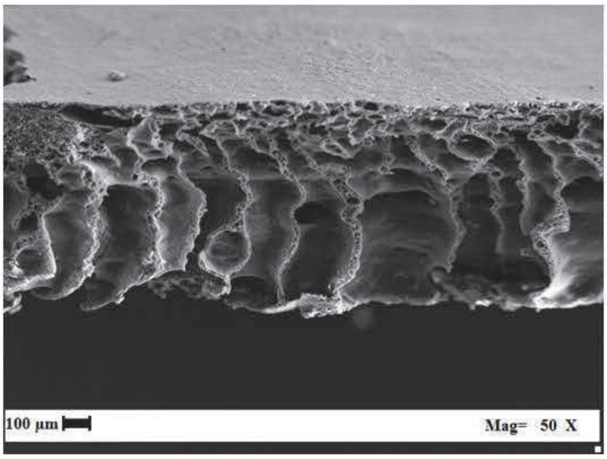

Figure V.1 *Section of a CA membrane obtained starting from a 10% w/w CA solution. Process conditions 150 bar, 55°C*

We also analyzed the membrane surfaces and corresponding FESEM images are reported in Figure V.2; as indicated in the previous paragraph, the membrane is characterized by a partially porous bottom surface (Figure V.2a) and cellular top surface (Figure V.2b).

These results indicate that 10% w/w membranes are not symmetrical. Porosity analysis has been performed and values of about 79% void space have been found inside these membranes.

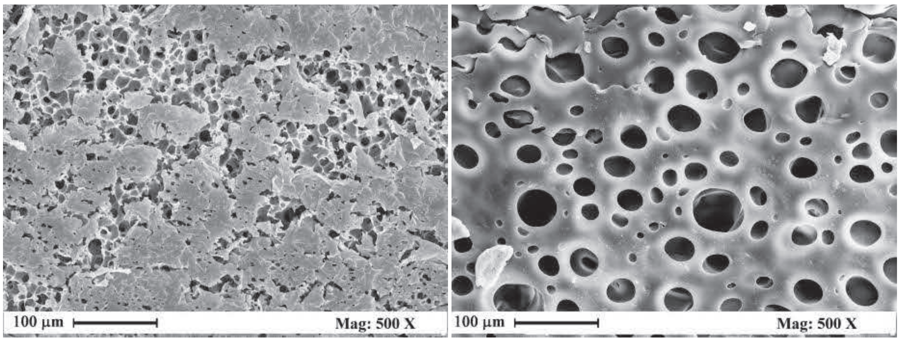

a b

Figure V.2 *Membrane obtained starting from a 10% w/w CA solution processed at 150 bar, 55 °C: (a) bottom surface; and (b) top surface*

V.1.2.2 CA concentration 15% w/w

It is possible to observe from FESEM image reported in Figure V.3 that the membrane at 15% w/w CA, processed at 200 bar and 45 °C, presents a cellular morphology. Using this starting CA concentration, the same morphology has been obtained at all the operative conditions tested.

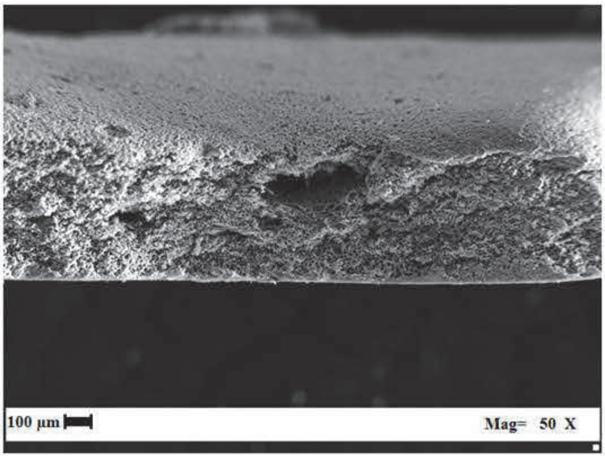

Figure V.3 *Section of a CA membrane obtained starting from a 15% w/w CA solution. Process conditions 200 bar, 45 °C*

However, the structures obtained present different pore size. Pores diameter analysis has been performed using the techniques reported in Chapter IV. From Figure V.4 and Table V.1, it is possible to observe that increasing the density of SC-CO_2, the average pore size decreases from 9.47 to 2.42 μm; pore size distribution also sharpens.

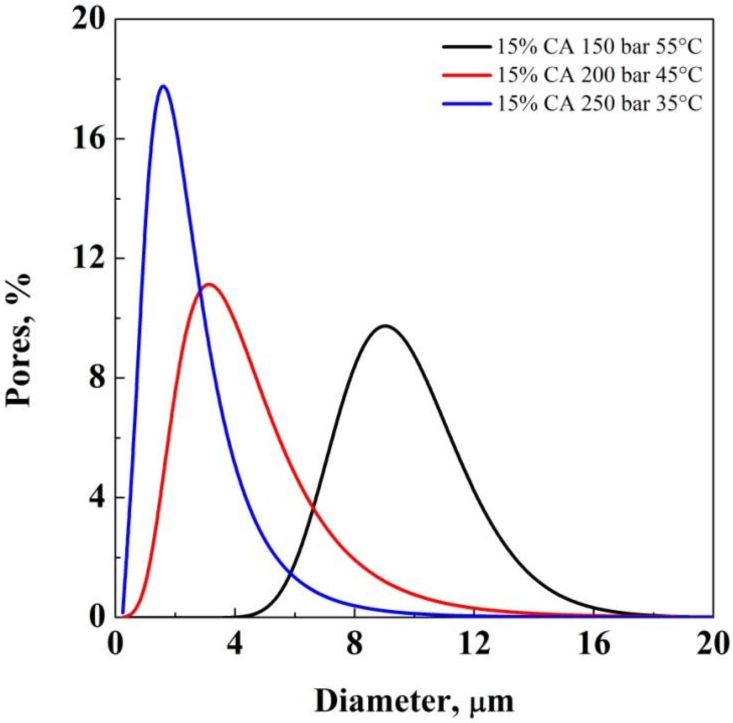

Figure V.4 *Pore size distribution in CA membranes obtained starting from a solution 15% w/w, processed at 55/150, 45/200, and 35/250 T/p*

Table V.1 *Membrane pore size analysis*

T [°C]	*P [bar]*	*CA [% w/w]*	*Mean pore size and standard deviation [µm]*
35	250	15	2.42 ± 1.27
		20	2.10 ± 1.07
45	200	15	4.64 ± 2.26
		20	2.97 ± 1.65
55	150	15	9.47 ± 2.30
		20	5.97 ± 1.65

In these experiments, both membrane surfaces are characterized by a dense layer with isolated pores; i.e., symmetrical membranes have been obtained. Porosity analysis has been performed and about 73% of void space has been found inside the CA membranes.

We also focused our attention on the effect of one of the crucial parameters of the process: the temperature. In particular, we reported the effect of temperature on membranes generated at 200 bar: increasing temperature from 35 to 55 °C, the membrane pore size increases from about 3.78 to 9.34 µm, as shown in Figure V.5.

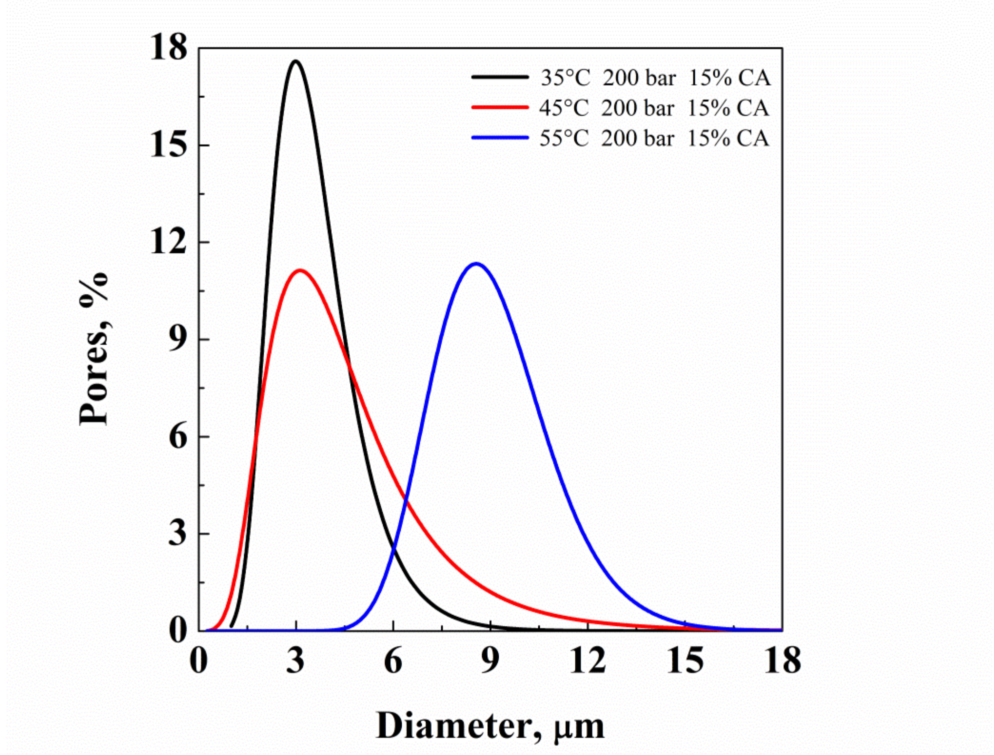

Figure V.5 *Pore size distribution in CA membranes obtained starting from a solution 15% w/w, processed at 55/200, 45/200, and 35/200 T/p*

V.1.2.3 CA concentration 20% w/w

Membranes generated from CA solutions at 20% w/w presented again a cellular structure. In Figure V.6, FESEM images of the section of a membrane processed at 250 bar and 35 °C are shown; they have been taken at two different magnifications: membrane uniformity is shown in the lower magnification image, whereas pores structure is better evidenced at larger magnification.

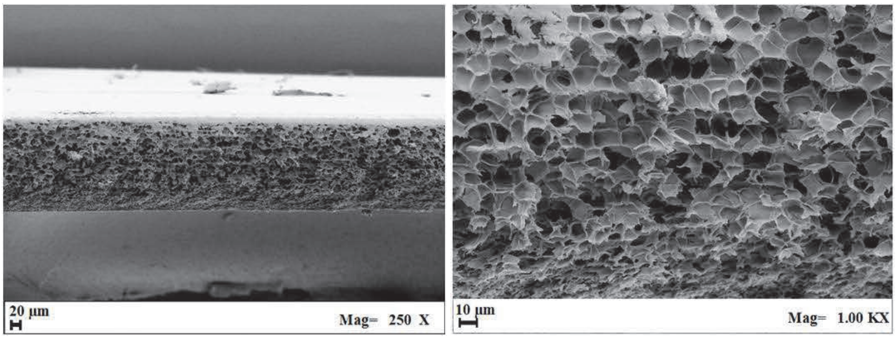

a b

Figure V.6 *Section of a CA membrane obtained starting from a 20% w/w CA solution, taken at different enlargements: (a) 250 X; and (b) 1000 X. Process conditions 250 bar, 35 °C*

For this CA concentration, the porosity of the membrane is even more regular when compared to the membranes produced at 15% w/w CA, as evidenced by the comparison of FESEM images in Figure V.6 with that in Figure V.3.

This observation is confirmed by the diagram reported in Figure V.7 and by data in Table V.1, in which the pore size distribution is shown for CA membranes obtained from 20% w/w solutions, processed at 55/150, 45/200, 35/250 T/p.

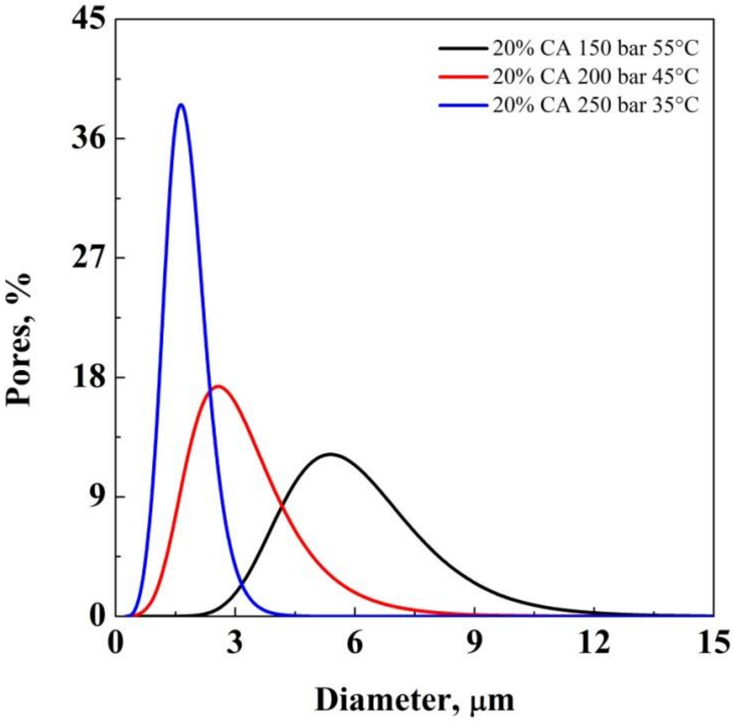

Figure V.7 *Pore size distribution in CA membranes obtained starting from a solution 20% w/w, processed at 55/150, 45/200, and 35/250 T/p*

As in the previous case, increasing the density of SC-CO_2, the average pore size decreases (from 5.97 to 2.10 μm) and the cell distributions are sharper; compared with Figure V.4, the measured mean pore sizes are smaller and the distributions are sharper.

In this series of experiments, both membrane surfaces have been characterized by a dense layer with isolated pores; i.e., symmetrical membranes have been obtained. Porosity analysis has been performed in this case and 69% of void space has been found.

V.1.2.4 Comments and formation mechanisms

For what concerns the formation mechanisms related to the different membrane morphologies observed in this study, we can look at a qualitative triangular diagram (see Figure V.8), and refer to the classical inversion phase theory (Van de Witte *et al.*, 1996a) (although in this case we are neglecting the presence of water in the system).

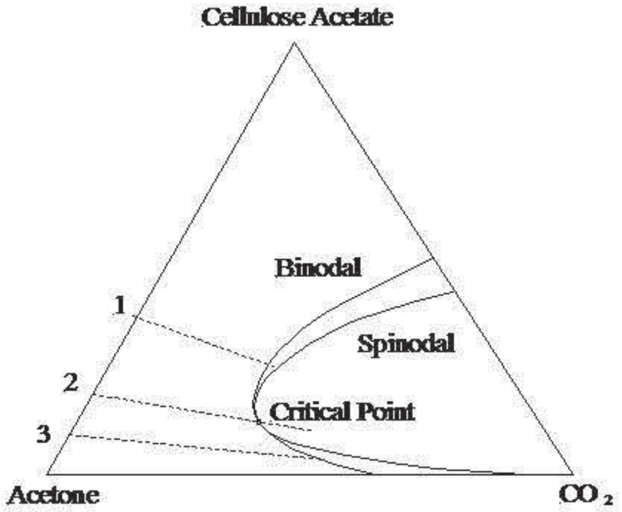

Figure V.8 *Generic equilibrium diagram CA/acetone/SC-CO_2*

Starting from the more dilute solution (e.g., 5% w/w CA, path 3), taking into account the addition of the non-solvent (SC-CO_2), the trajectory of the system can enter in the miscibility gap between the bimodal and the spinodal curve below the critical point. In this zone, the phase separation with nucleation and growth of a polymer rich phase within a polymer poor phase takes place, with the consequent formation of a particulate structure. Increasing the polymer concentration (e.g., 10% w/w CA, path 2), the path enters in the spinodal region and fingers are obtained. Their formation can be explained by the mechanism proposed by Stropnik et al. (Stropnik *et al.*, 2002). According to these authors, during the skin formation, part of the non-solvent enters in the layer just beneath the skin and induces the phase separation. It goes on until the shrinkage of the upper part of the membrane-forming system starts and forms a pressure wave that induces the coalescence of the growing nucleus of polymer. At 15% w/w CA, which corresponds to path 1, the trajectory of the system enters the upper part of the miscibility gap, between the bimodal and spinodal curve. In this case, the phase separation occurs with nucleation and growth of the polymer poor phase within the polymer rich phase, leading to the formation of a cellular structure. A similar interpretation is possible for the formation of 20% w/w CA membranes.

Considering the effect of process parameters (pressure and temperature) on the pore size, the results can be explained considering that when SC-CO_2 density decreases, the phase separation process becomes slower, and the polymer-poor phase has more time to grow; as a consequence, larger pores are generated. This behavior has been observed at all process conditions tested.

V.1.3 Other characterizations of CA membranes

DSC and EDX analyses are reported for the membranes processed at 200 bar and 45 °C. The aim of DSC analysis has been to compare CA and lysozyme thermograms with those of the different polymer/enzyme formulations.

CA thermogram, in Figure V.9, shows that the polymer glass transition temperature is located at about 78 °C, and its melting temperature is 237 °C.

Lysozyme thermogram has a minimum at 60 °C, which corresponds to the enzyme denaturation temperature.

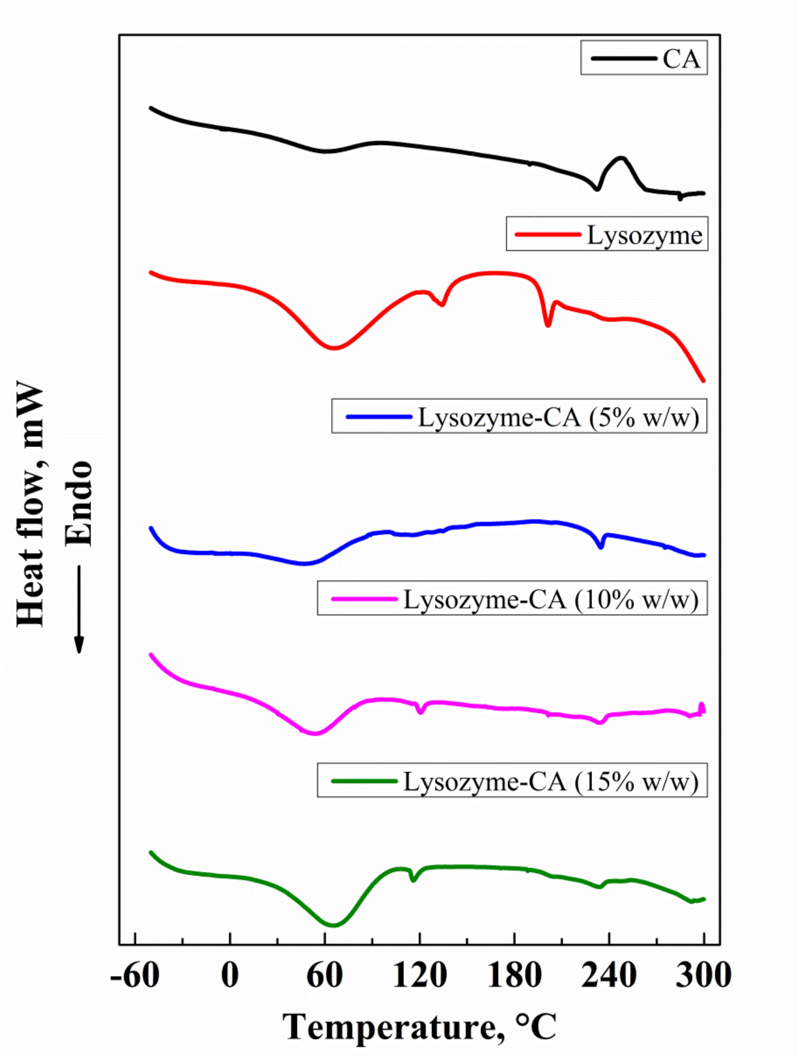

Figure V.9 *Thermograms of CA, lysozyme and CA plus lysozyme membranes processed at 200 bar, 45 °C*

By increasing the polymer concentration, a minimum localized at about 60 °C becomes evident, that corresponds to the denaturation temperature of the enzyme. The glass transition temperature of pure CA is preserved, whereas the melting peak tends to expand as a function of the polymer amount in the starting solution. Indeed, the area of the peak is proportional to the mass, the enthalpy of fusion and the percentage of crystallinity of the polymer.

Thermograms in Figure V.9 also confirm the encapsulation of the enzyme within the polymer matrix and highlight the fact that polymer and lysozyme maintain their physical characteristics, behaving like a two components mixture.

To evaluate the dispersion of the enzyme in the polymer matrix, EDX analysis has been performed. In Figure V.10, maps of Carbon (for CA) and Sulfur (for lysozyme) in a membrane at 20% w/w CA and processed at 200 bar and 45 °C are reported. Sulfur signal has been selected to indicate lysozyme, since sulfur bridges form covalent bonds between cysteines that stabilize the tertiary structure of the enzyme.

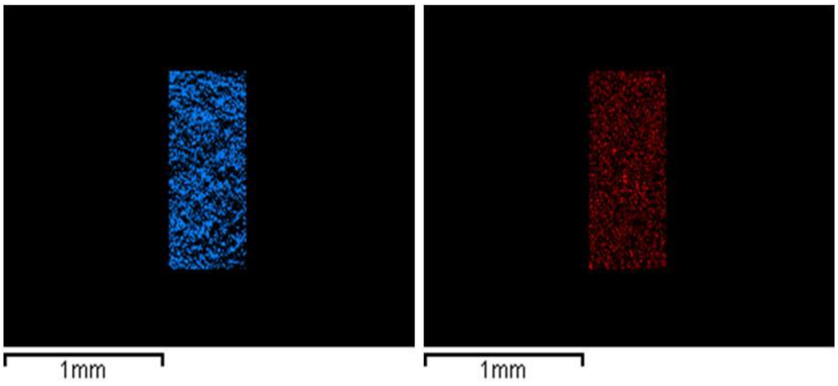

a b

Figure V.10 *EDX maps of a membrane at 20% w/w CA processed at 200 bar, 45 °C: (a) Carbon atoms in blue (i.e., CA) and (b) Sulfur atoms in red (i.e., lysozyme)*

The maps (Figure V.10) of the elements generated by the EDX analysis show that the antimicrobial compound is uniformly dispersed within the polymeric matrix, because the areas in which Carbon is present (blue) correspond to the areas in which lysozyme (Sulfur, in red) is also detected.

Summarizing, DSC and EDX results demonstrated the achievement of a necessary prerequisite (homogeneous encapsulation of the bio-component) to obtain the controlled release of the enzyme for the produced membranes.

V.1.4 Lysozyme release kinetics and activity

At this point of the study, we decided to select some of the produced membranes, to study the release of lysozyme and its activity, when it interacts with the selected microorganism (*M. lysodeikticus*).

It is relevant to indicate that CA + lysozyme membranes at CA concentration of 10% w/w, as previously discussed, do not present a cellular structure, however, they have also been selected, to verify the relevance or not of membrane microstructure on enzyme release kinetics. CA membranes at 15 and 20% w/w show a cellular structure and, therefore, they probably present the best selection of characteristics for enzyme release.

Another fact that has to be punctualized is that lysozyme can diffuse from the membrane to the bulk of the liquid solution and we will discuss about this amount as ‘mobile’ enzyme and, part of lysozyme can remain entrapped in the solid-porous structure: we will discuss about this amount as ‘immobilized’ enzyme. However, this part of the enzyme is not lost for the biological activity and, when in direct contact with the bacteria suspension, can maintain its killing activity.

Therefore, mobile and immobilized fractions are mostly a partition of the active device that can also be controlled by manipulating membranes morphology.

V.1.4.1 Influence of CA concentration on the kinetics of lysozyme release

The kinetics of lysozyme release from CA membranes produced in this study have been obtained measuring the increase of enzyme concentration in distilled water, using the following procedure: the enzymatic membrane was placed in a bottle containing 50 mL of distilled water and stirred at 250 rpm. To determine the release rate from the membrane and the concentration of lysozyme, analysis was carried out in continuation using an UV/Vis spectrophotometer, and reading the absorbance of the sample at 280 nm (that is the wave length at which lysozyme shows maximum absorption).

As expected, a continuous increase of lysozyme concentration has been observed, as reported in the diagram in Figure V.11, that is related to the release tests performed on lysozyme loaded CA membranes produced (see Table V.1 for the related data) at 10, 15 and 20% w/w CA. The maximum enzyme concentration (C_∞) has been normalized to 100% to allow the comparison of the release curves.

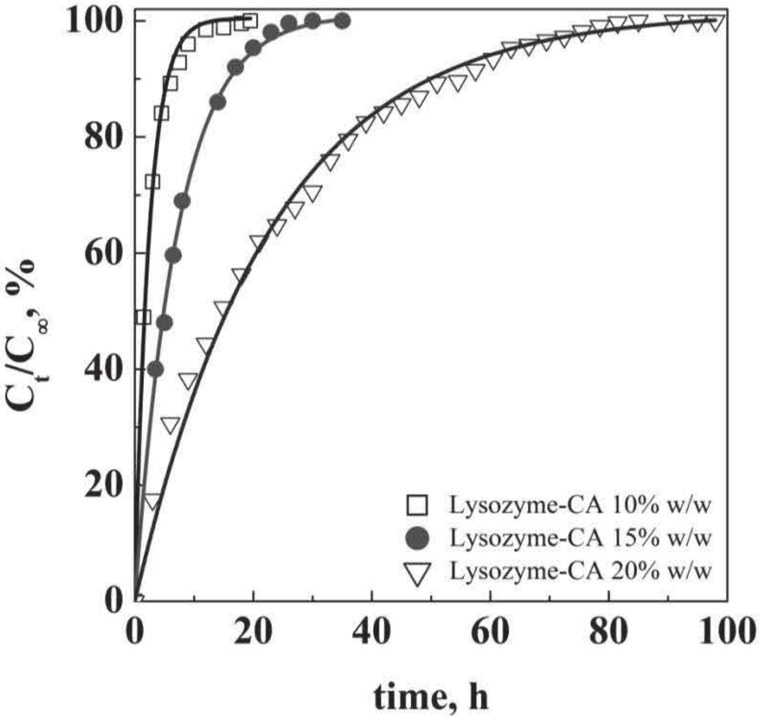
100
80
60
40
20
0
C_t/C_∞, %
0
20
40
60
80
100
time, h
□ Lysozyme-CA 10% w/w
● Lysozyme-CA 15% w/w
▽ Lysozyme-CA 20% w/w

a

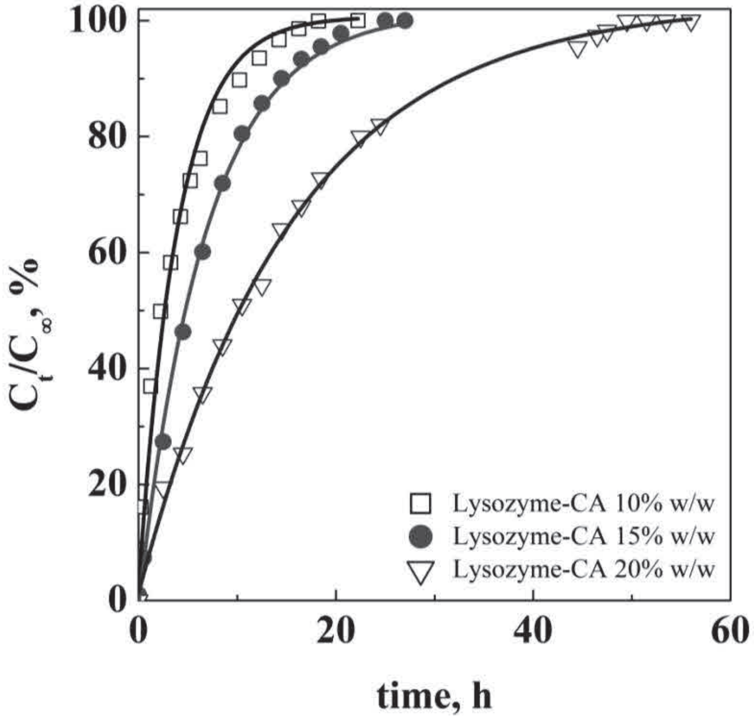
C_t/C_∞, %
0
20
40
60
80
100
time, h
0
20
40
60
□ Lysozyme-CA 10% w/w
● Lysozyme-CA 15% w/w
▽ Lysozyme-CA 20% w/w

b

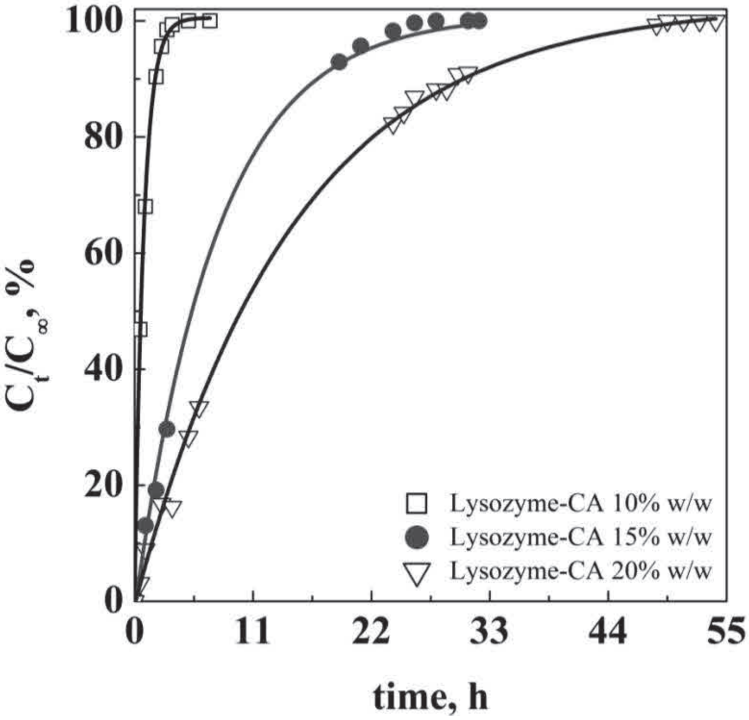

c

Figure V.11 *Comparison among lysozyme release kinetics from membranes at 10, 15, 20% w/w CA, processed at: (a) 250 bar, 35 °C; (b) 200 bar, 45 °C; and (c) 150 bar, 55 °C*

Increasing CA concentration, the diffusion rate of lysozyme decreases, due to the increase of mass transfer resistance and a maximum of about 90 h is required to obtain the maximum concentration (Figure V.11a). The same overall behavior has been observed for the membranes produced at 200/45 and 150/55 bar/°C (Figures V.11b and c). The only relevant difference is that in these cases the release has been completed in shorter times (maximum about 60 h). This result can be explained looking at the membranes morphological study previously performed: 150 bar/55 °C correspond to a CO_2 density of 0.66 g/cm^3, 200 bar/45 °C and 250 bar/35 °C correspond to CO_2 densities of 0.81 and 0.90 g/cm^3, respectively. The increase of CO_2 density produced CA membranes with smaller pore diameters and, therefore, the slowest diffusion rates have been observed for the membranes produced at 250 bar and 35 °C, even if the observed overall membranes morphology did not vary with density in the experiments performed at 200 bar, 45 °C and 250 bar, 35 °C.

Summarizing these results, when CA concentration in the starting solution was increased, lysozyme diffusion rate decreased; higher CO_2 densities produced smaller pores and, therefore, also a decrease of the enzyme diffusion rates. The maximum quantity of released enzyme decreased, it means that the relative quantity of mobile enzyme is smaller for the membranes produced at high CA concentration and at larger CO_2 densities.

V.1.4.2 Influence of CA concentration on mobile lysozyme activity

Mobile lysozyme activity has been measured for the membranes produced at 200 bar and 45 °C, using the method described by Mecitoğlu et al. (Mecitoğlu *et al.*, 2006); i.e., by measuring the decrease in absorbance of a *M. lysodeikticus* suspension (0.26 mg/mL) prepared in 0.05 M Na-phosphate buffer at pH 7.0. A volume of 2.3 mL of the substrate was mixed with 0.2 mL of the solution containing lysozyme. Analysis was performed at room temperature. The reduction in absorbance was measured at 660 nm (that is the wave length at which *M. lysodeikticus* shows maximum absorption) for 2 min, using an UV/Vis spectrophotometer. Enzyme activity was calculated from the slope of the initial linear portion of absorbance vs. time curve; it can be expressed as unit (U) or percent initial activity. One U was defined as a 0.001 change in absorbance within a 1-min time interval. The units were divided by membrane surface, and the activity was expressed in units per cm^2 (U/cm^2). Analyses were carried out in triplicate.

In Figure V.12, we reported the results and the fitting curves related to membranes produced at 10, 15 and 20% w/w CA. The measured activity (U_t) has been normalized on the maximum observed activity (U_∞) to allow the comparison of the performance of the different membranes; its absolute values are reported in Table V.2.

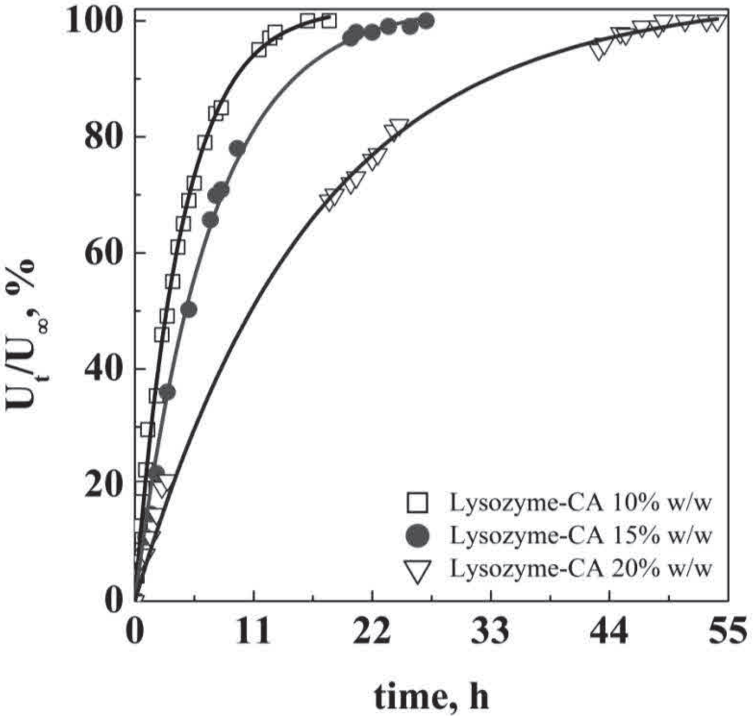

Figure V.12 *Comparison among enzymatic activities of mobile lysozyme from membranes at 10, 15, 20% w/w CA, processed at 200 bar, 45 °C*

Table V.2 *Mobile lysozyme activity for CA membranes processed at 200 bar and 45 °C*

Composition (CA, % w/w)	***Maximum activity of mobile lysozyme (U/cm^2)***	***Approximate time to obtain maximum activity (h)***
10	189	20
15	51	23
20	26	45

First of all, these results confirm that lysozyme has maintained its killing activity against the microorganism and confirm that the process we adopted did not destroy the delicate 3-D organization (unfolding) of the biomolecule and its activity has not been compromised. The maximum duration of this activity is about 90 h (for 20% w/w membrane at 250 bar, 35 °C) that corresponds to about 4 days of protection of the system to be preserved.

V.1.4.3 Immobilized lysozyme activity

We have seen in the previous discussion that part of lysozyme remains entrapped in the membranes structure and that this quantity increases with CA concentration and CO_2 density. However, this part of the enzyme can be relevant and should be still active: it can still interact with the microorganism and kill it. The analysis of immobilized enzyme activity has been previously reported, using crushed membranes (Mecitoğlu *et al.*, 2006). The measurement of immobilized lysozyme activity on CA membranes produced at 200 bar/45 °C, using the same membranes that have been previously used to measure the asymptotic release of the mobile enzyme, has been performed using the following method (Mecitoğlu *et al.*, 2006): the membrane was placed in a glass bottle and brought in direct contact with 25 mL of a suspension of *M. lysodeikticus* (0.26 mg/mL); also this analysis was performed at room temperature. The decrease in absorbance at 660 nm was monitored periodically. The activity of lysozyme was determined in the same manner as for mobile enzyme.

Looking at results reported in Figure V.13, lysozyme entrapped in CA membranes is still active, therefore, the process has been sufficiently mild to avoid impairment of enzyme activity also inside the membrane. In these experiments, CA membranes were put in direct contact with the *M. lysodeikticus* suspension and contained different starting quantities of enzymes, depending on the facts that have been previously used to release the mobile fraction of lysozyme. This consideration explains the fact that 10% w/w CA membranes did not contain enzymes enough to kill all micrococcus contained in the suspension; indeed, these membranes showed a very large maximum activity for mobile lysozyme release (189 U/cm^2) when compared to the corresponding maximum activity of the other membranes (Table V.2). Fifteen and 20% w/w CA membranes, instead, have been able to kill all microorganisms present in the suspension in about 2 and 1 h, respectively (see Figure V.13). At this point, we decided to perform a further series of experiments on the same CA 20% w/w membrane, using the procedure that we have adopted for immobilized enzyme activity; i.e., we repeated several times the experiment, using the same membrane and changing the *M. lysodeikticus* suspension after the complete killing of the microorganism. We observed (see Figure V.14) that the membrane killing activity was maintained for (some) subsequent experiments and only after four experiments in series, the enzyme contained in the membrane was no more sufficient to kill all the *M. lysodeikticus* contained in the suspension.

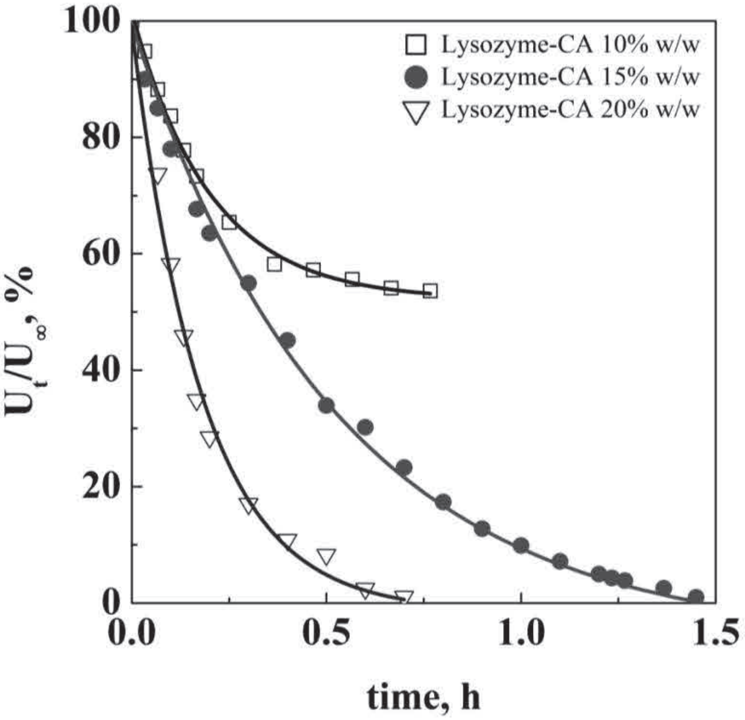

Figure V.13 *Enzymatic activity of lysozyme immobilized in membranes processed at 200 bar, 45 °C at: 10%, 15% and 20% w/w CA*

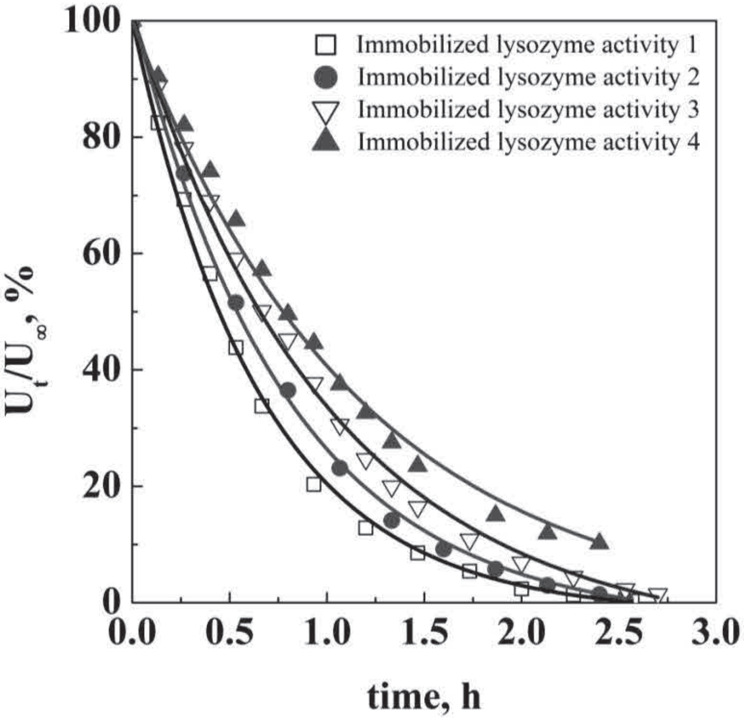

Figure V.14 *Immobilized lysozyme activity of 20% w/w CA membrane, processed at 200 bar 45 °C, when the direct contact with the microorganism was replicated*

Therefore, we can consider that we have observed two limit behaviors for 10 and 20% w/w CA membranes. In the 10% w/w case, the majority of the enzyme was mobile, as a result of the extremely opened finger structure, and its mobile activity was strong; but, its corresponding immobilized activity was not sufficient to kill all the microorganism when it was, subsequently, put in direct contact with it. On the contrary, in the 20% w/w CA case, mobile lysozyme was at the lowest value (see Table V.2), but, the immobilized part contained in the membrane was able to kill all the *M. lysodeikticus*, when in direct contact, for several repeated experiments.

V.1.5 Conclusions

CA membranes loaded with lysozyme were successfully produced and characterized; the enzyme retained its activity that was tested against *M. lysodeikticus*.

The results are very interesting in terms of release times: up to a maximum of 90 h for mobile enzyme for CA membranes produced at 250 bar and 35 °C. The presence of mobile and immobilized enzyme suggests that the membranes can be optimized for two different uses: if lysozyme migration is required to obtain a long range effect in the selected environment, membranes that release the major quantity of mobile lysozyme are preferable. If a localized strong effect is required to produce a direct interaction with the target surface, membranes with the largest quantity of immobilized enzyme should be used.

V.2 Graphene oxide exfoliation and purification during the formation of cellulose acetate nanocomposites by supercritical CO_2 assisted phase separation

The aim of this work is to obtain homogenous polymer-GO nanocomposite matrices controlling the exfoliation and, more generally speaking, the interactions of GO layers and their behavior in a polymeric matrix using SC-CO_2 assisted phase separation.

The aim is to combine the advantages of SC-CO_2 assisted loading techniques with the possibility of increasing/controlling the exfoliation of GO. CA has been selected as the polymeric matrix, due to its numerous potential applications; for example, as scaffold in cartilage regeneration (Mayer-Wagner *et al.*, 2011), neural differentiation (Du *et al.*, 2014) and cardiac applications (Entcheva *et al.*, 2004), in dialysis membranes (Idris *et al.*, 2006) and in ultrafiltration devices (Kutowy *et al.*, 1975).

We verified the process feasibility and its implications on GO composition and layers arrangement. We also analyzed the effect of different GO loadings on morphology, pore size and on the physico-chemical characteristics of the composite structures.

V.2.1 Preparation of CA/GO composite structures

We produced CA/GO composites by a SC-CO_2 assisted phase separation process. First, solutions of CA in NMP with a concentration of 25% w/w were prepared. Subsequently, GO was suspended in the polymeric solution with concentrations of either 3 or 9% w/w with respect to the polymer content. The ternary system was stirred at room temperature until it became homogeneous and, then, was phase-separated using SC-CO_2 at 200 bar and 40 °C for 4 h, with a CO_2 flow rate of about 2 Kg/h. In the remainder of this work, these samples will be noted as CA_GO_1 and CA_GO_2 for GO fillings of 3 and 9% w/w, respectively. Further, CA/GO composites (termed as CA_GO_2_8h) were obtained after 8 h phase separation at 200 bar and 40 °C, from a GO 9% w/w polymeric solution. The vessel was filled from the bottom with SC-CO_2, up to the desired pressure, using a high pressure pump

(Milton Roy-Milroyal B, Pont-Saint-Pierre, France). The pressure was controlled by a manometer (mod. MP1, OMET, Italy) and the temperature was set by a controller (mod. 305, Watlow, Italy). A depressurization time of 15 min was used to bring back the system at atmospheric pressure.

V.2.2 GO characterization

TEM images of GO produced in this work are shown in Figure V.15: thin layers with sizes in the range of half to tens of square microns were observed. GO was laminar, curled and corrugated, as reported before (Chai *et al.*, 2014), due to the presence of surface functional groups such as hydroxyl groups, carboxyl groups and epoxy groups. In particular, in Figures V.15E and F nanosheets edges of about 5 nm can be detected that correspond to the largest thickness observed in the sample. In the regions indicated by the arrows in Figures V.15E and F, 6 and 4 twisted layers can be seen, respectively. Therefore, we can state that the starting GO material was organized in a few layers; i.e., it was partly exfoliated. Thinner nanosheets can be seen in Figure V.15G. Figure V.15C shows the energy dispersive TEM based EDX of the prepared sample, with a carbon/oxygen (C/O) ratio of ~ 2.6 .at (Compton *et al.*, 2011). Small amounts of S and Cl, deriving from the GO preparation process are also present; indeed, it is know that even a very accurate washing process cannot completely remove these species from GO (Eigler *et al.*, 2012a).

The (002) reflection peak of graphite flakes appears at $2\theta=26.0^{\circ}$, exhibiting a highly ordered crystal structure with an interlayer spacing of 3.4 Å, that is consistent with the literature (Lee *et al.*, 2008). After oxidation of the precursor, XRD pattern of GO shows the (002) reflection at $2\theta=8.9^{\circ}$, that corresponds to an interlayer space of 7.9 Å (Figure V.16A). This can be explained by the hydrophilic character induced by the high oxidation level of GO, favoring the presence of intercalated water molecules between adjacent GO sheets (values varying form 0.6 nm for dry GO to 1.2 nm for hydrated GO have been reported) (Stankovich *et al.*, 2007).

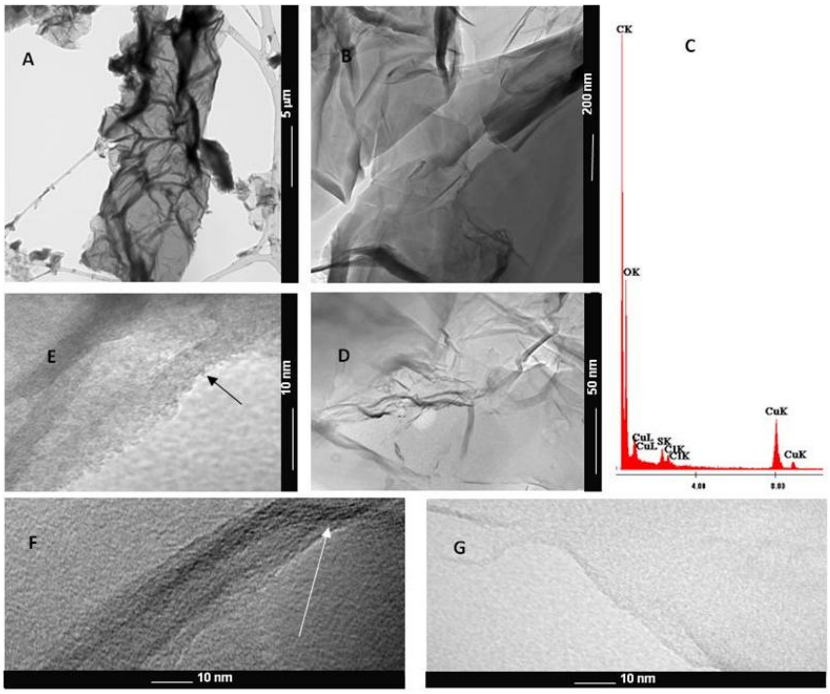

Figure V.15 *(A,B,D,E,F,G) TEM images of GO at different magnifications, (C) EDX spectrum taken in the area indicated with D*

GO powder was further investigated by Raman spectroscopy. As shown in Figure V.16B, the Raman spectrum of GO displays two prominent peaks at: ~1357 and ~1596 cm^{-1}, that correspond to the well-documented D (the breathing mode of A_{1g} symmetry involving phonons near the K zone boundary) and G (originated from the in-plane vibration of sp^2 carbon atoms that is a doubly degenerate phonon mode (E_{2g} symmetry) at the Brillouin zone center) bands, respectively (Wojtoniszak *et al.*, 2012a; Sarno *et al.*, 2014). The G band broadens and up-shifts in comparison to those observed in graphite (~1581 cm^{-1}). A possible explanation of this behavior is the presence of isolated double bonds which resonate at higher frequencies (Wojtoniszak *et al.*, 2012a). Generally, GO exhibits preserved graphene like regions (about 1 nm diameter) and distorted regions (several nm) related to the synthesis (Eigler *et al.*, 2012a). The I_D/I_G ratio in Raman spectroscopy can be used to evaluate the distance between defects in graphene and for GO it is about 0.9 (514 nm laser excitation); it increases with increasing the mean distance between two defects (L_D) from 1 to about 3 nm, followed by a decrease for larger distances $L_D > 3$ nm (Cançado *et al.*, 2011). In our case, the I_D/I_G ratio is 0.85 indicating a L_D of about 1.5 nm. In the spectrum are also visible the 2D peak at 2700 cm^{-1}, that is the second order of the D peak and the D + D’ peak at 2940 cm^{-1} due to the defect activated combination of phonons (Erickson *et al.*, 2010). The D + D’ peak, as usually for GO, is higher in intensity than the 2D peak.

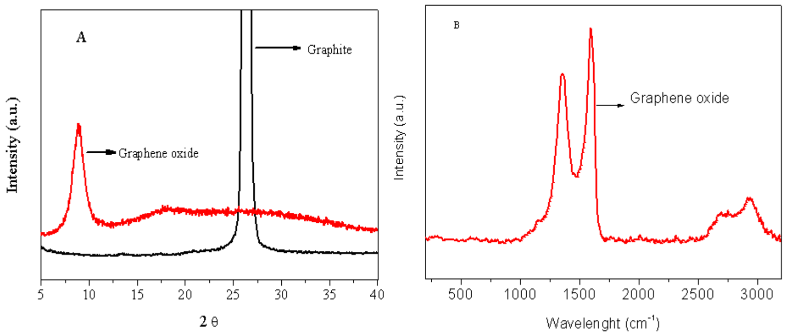

Figure V.16 *XRD of starting Graphite and of GO (A), GO Raman Spectrum (B)*

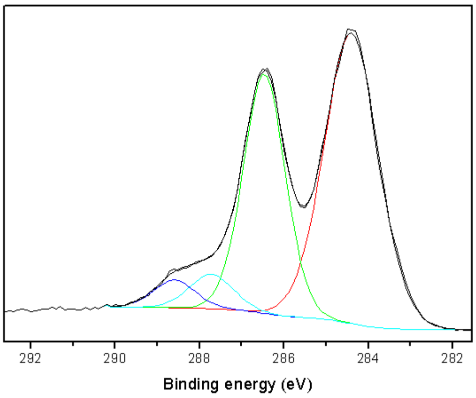

Figure V.17 *XPS - C 1s core level for GO*

The formation of oxygenated groups due to the oxidation of graphite is confirmed by XPS. The C/O ratio, calculated from C 1s and O 1s core level spectra, decreased from 58.9 to 2.5 after the oxidation process, clearly indicating a considerable degree of oxidation. The C 1s XPS spectrum of GO, shown in Figure V.17, exhibited the characteristic peaks of C–C skeleton, hydroxyl, epoxyl and carbonyl groups at 284.4, 286.4, 287.7 and 288.7 eV, respectively (Krishnamoorthy *et al.*, 2013).

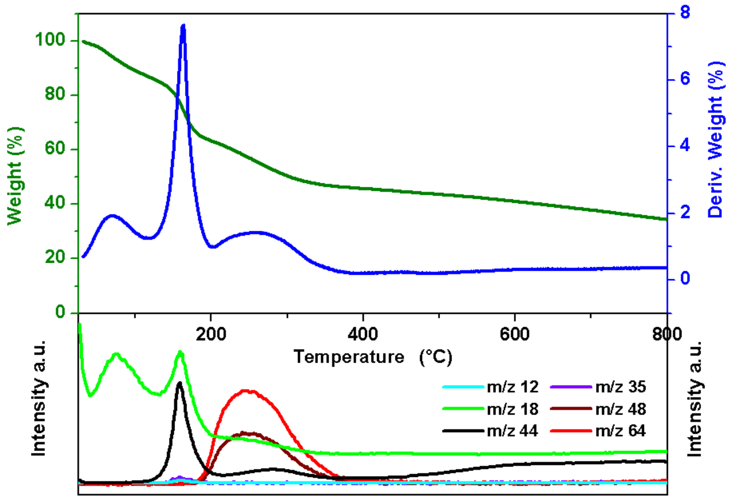

Figure V.18 *TG-DTG-MS profiles for GO*

GO was analyzed by simultaneous thermogravimetric and mass spectrometric analysis (TG-MS), under 1% v/v O_2 in N_2 (Figure V.18). The weight loss took place in three temperature regions. Between room temperature and about 115 °C the weight loss can be attributed to physically adsorbed water (as indicated by the corresponding total ion current (TIC) m/z=18) (Ali *et al.*, 2009). The TG-MS analysis indicated that the second weight loss (115-200 °C) was mainly due to water and simultaneous release of CO_2 (Barroso-Bujans *et al.*, 2010; Eigler *et al.*, 2012b). Ali et al. (Ali *et al.*, 2009) suggested that the elimination of CO_2 increases hydrophobicity which leads to co-elimination of water bound to hydrophilic sites. Additionally, HCl (m/z=35) is detected that originates from Chlorine species. At higher temperature, in the range 200-400 °C, the weight loss is due to the carbon lattice oxidation and SO_2 (m/z=64) that originated from Sulfur species (Eigler *et al.*, 2012a). Above 400 °C a further slight weight loss with a contemporaneous release of CO_2 takes place. The residue is constituted by the most abundant and stable Carbon in this oxygen atmosphere.

V.2.3 Polymer-GO nanocomposites

In this part of the work, we focused our attention on the feasibility of the SC-CO_2 assisted phase inversion process on the system CA/GO. We prepared solutions containing 25% w/w of CA in NMP and added different amounts of GO, varying from 3 to 9% w/w with respect to polymer content. The operative parameters were selected considering a previous work on CA membranes formation by SC-CO_2 assisted phase inversion (Reverchon *et al.*, 2004); in particular, pressure of 200 bar and temperature of 40 °C were selected, since they represent the optimized thermodynamic combination (Reverchon *et al.*, 2004).

From a macroscopic point of view, the structures produced using CA alone, show a white and opalescent color (see Figure V.19a), whereas, CA structures loaded with 3 and 9% w/w GO, show an uniform black color (Figure V.20a, Figure V.21a).

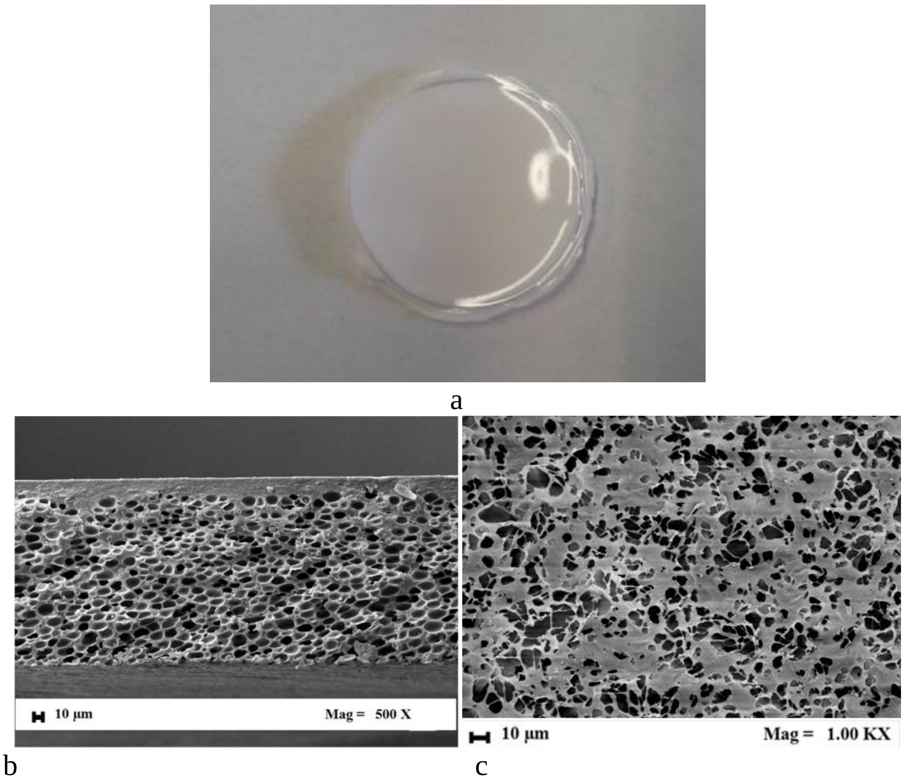

Figure V.19 *CA structures obtained at 200 bar 40 °C starting from 25% w/w CA/NMP solution: a) macroscopic view, b) FESEM analysis of the section, c) FESEM analysis of the top surface*

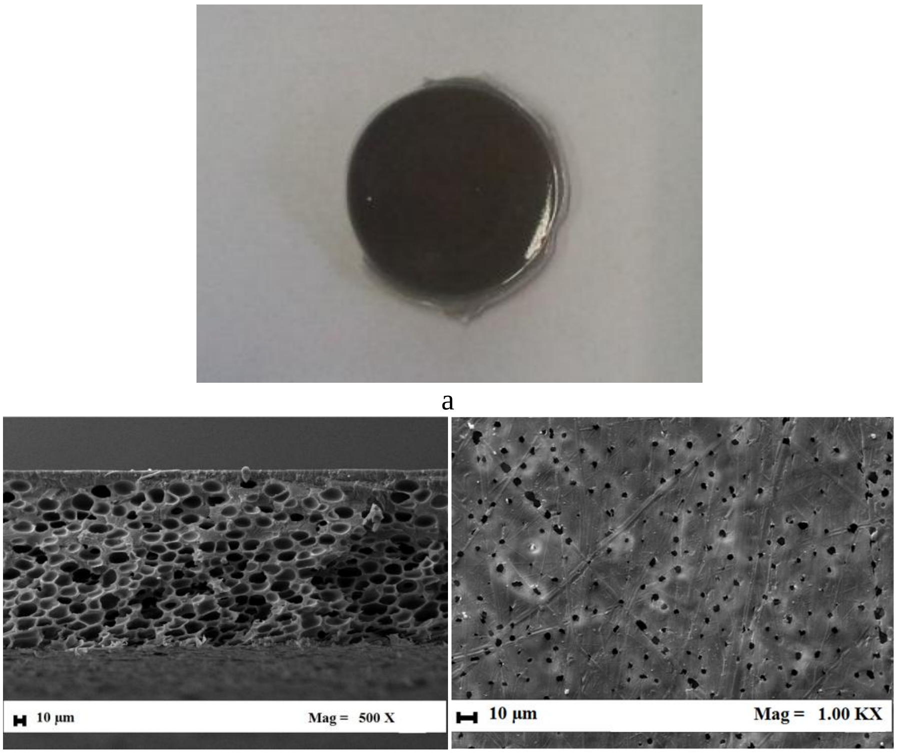

a

b c

Figure V.20 *CA/GO structures obtained at 200 bar 40 °C starting from 25% w/w CA/NMP solution and 3% w/w of GO: a) macroscopic view, b) FESEM analysis of the section, c) FESEM analysis of the top surface*

a

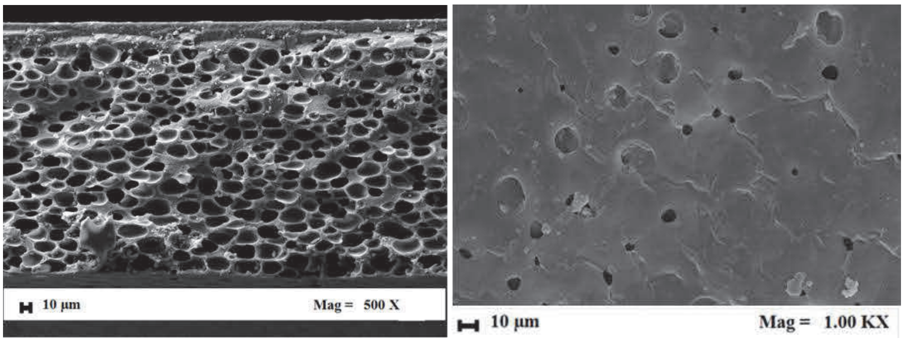

b c

Figure V.21 *CA/GO structures obtained at 200 bar 40 °C starting from 25% w/w CA/NMP solution and 9% w/w of GO: a) macroscopic view, b) FESEM analysis of the section, c) FESEM analysis of the top surface*

From a microscopic point of view, we observed from FESEM images, that, even with the highest GO content, the section of the structures maintain the cellular morphology, characteristics of CA alone (Figure V.19b compared with Figures V.20b-V.21b). Porous top surfaces were obtained in all cases (Figures V.19c-V.20c-V.21c) and a quasi-constant overall porosity (between 80-82%) was also measured. No stratification of GO towards top or bottom surfaces was observed, also at microscopic level.

DSC analyses were also performed on CA membranes and CA/GO composite structures. They showed similar traces for all materials treated, confirming that GO addition did not sensibly influence the physico-chemical characteristics of the final structures.

Summarizing, these results show that the morphology of CA structures loaded with GO is similar to those produced with pure CA; i.e., GO presence does not affect the structure formation mechanism during the process assisted by SC-CO_2 and GO is uniformly loaded in the porous structure. Moreover, when we performed FESEM analyses at higher enlargements (up to 150000 KX), aggregates of GO were not more visible in the polymeric structure; this is an information about the dispersion of GO in the polymeric matrix even at micro/nano-level. The morphology obtained (i.e., porous) suggests that nucleation and growth of droplets of the polymer-lean phase, with further solidification of the polymer-rich phase is the mechanism of the structure formation.

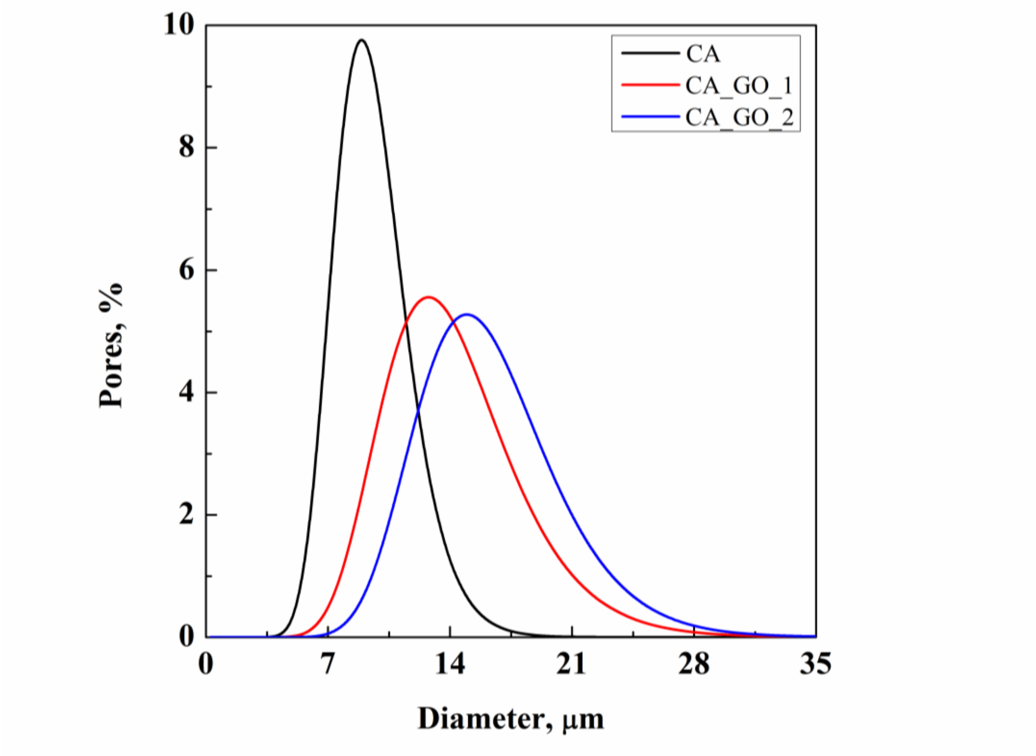

Figure V.22 *Pore size distribution in CA/GO composite structures obtained at different GO loadings*

Table V.3 *Mean pore size of CA+GO structures obtained at different GO loadings*

Sample	***Mean pore size ± standard deviation (μm)***
CA	9.2 ± 2.1
CA_GO_1	14.0 ± 3.9
CA_GO_2	16.6 ± 4.2

Increasing the amount of GO in the starting solution, the mean pore size of the structures enlarges. This result is well evidenced by the pore size distribution reported in Figure V.22 and by data in Table V.3: increasing the amount of GO up to 9% w/w, the mean pore size increases from 9.2 to 16.6 µm. It indicates that even if the structures morphology has not been affected, the addition of GO plays an important role during the structure formation process. A plausible explanation for this result is that the affinity of GO with many kinds of hydrophilic groups can decrease the mass transfer between the solvent and SC-CO_2 (i.e., the non-solvent) during the phase-separation: larger pore are formed due to the slower mass transfer. Moreover, the presence of GO can disrupts the polymer chains, facilitating pores formation. These hypotheses are also supported by the slight effect of GO content on the porosity of top surfaces. Increasing the amount of GO, the top surface porosity decreases (Figures V.19c-V.20c-V.21c) and it is known that porosity of membranes surface depends on the phase separation rate: when the process is slower, the top surface tends to become “denser”, whereas, in the case of faster process, the top surface is usually “opened”.

Therefore, the addition of GO does not visibly affect thermodynamics of the phase separation process (i.e., the structure formation mechanism), but, influences the microstructure formation acting on the kinetics of the process (i.e., the phase separation rate).

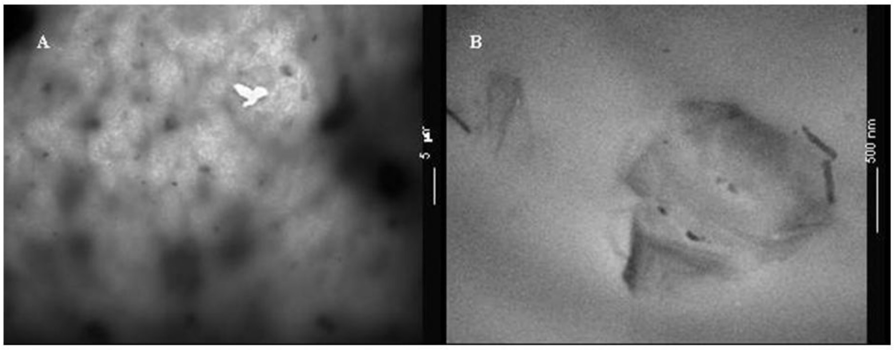

Figure V.23 *TEM image of CA_GO_2_8h at different magnifications*

Figure V.23 shows two TEM images, at increasing magnification, of the polymer-GO composite. The GO nanosheets are visible in Figure V.23A as black spots. Their lateral size is consistent with the starting GO sheets, as further evidenced by the high resolution TEM image (see Figure V.23B). In particular, in this image, GO is well separated and exfoliated, dispersed into the polymer matrix. Therefore, the partly exfoliated starting GO material (see starting GO characterization) has been furtherly separated as individual nanolayers and its eventual restacking has been blocked by SC-CO_2 processing and by incorporation in the polymeric structure.

An explanation of this result is that CO_2 is a small molecule that, at supercritical conditions, maintains gas-like properties as low viscosity, zero surface tension and high diffusivity; therefore, it can penetrate the solid material and can delaminate tightly-stacked layered materials. This effect has been sometimes described for nano-clays and graphite (Pu *et al.*, 2009).

In Figure V.24 the TG-MS profiles, under a 1% v/v of O_2 in N_2 flow, of tests CA, CA_GO_1, CA_GO_2, CA_GO_2_8h, are reported as a function of temperature. During the thermal oxidation of CA, after an initial weak release of water ~5.0% w/w, the weight loss took place in the range 270-435 °C in which the main mass fragments of CA (m/z=15, 30, 43, 55, 61) were detected, together with m/z=18 of H_2O and m/z=44 due to the formation of CO_2. The remaining carbon is oxidized completely up to 900 °C.

In all the composites an additional weight loss was clearly visible at lower temperature, between about 190 and 270 °C. This weight loss is certainly due to a CA fraction, as confirmed by the evolution of its main mass fragments, that oxidizes/decomposes at lower temperatures in presence of GO. It increases at increasing GO content in the composites and decreases at increasing SC-CO_2 process time. No evidence of specific weight losses due to GO oxyfunctional groups can be seen. For all the composites, unlike CA, the residue at 900 °C is not zero, it is due to GO and obviously increases with GO content but also with SC-CO_2 treatment times. This last observation, together with the no relevant presence of oxyfunctional groups release, suggests that the SC-CO_2 process promotes a GO partial reduction, which is probably the reason for the increased carbon skeleton amount (Ganguly *et al.*, 2011) and reduced weight loss between 190 and 270 °C (that is probably due to CA fraction adjacent to the highly reactive functional groups of GO). This effect of SC-CO_2, though under different conditions, has been already reported (Rangappa *et al.*, 2010); but, it is the first time that it is evidenced during the incorporation in a polymeric matrix. The results also suggest that the reduction level could be modulated by varying the processing time.

No trace of SO_2 (m/z=48, 64) and Chlorine (m/z=35) initially retained in GO (see starting GO characterization) can be seen. This result evidences a further effect of SC-CO_2 processing: the ability to remove residual solvent/impurities. Therefore, all residual traces from the GO preparation are removed. This capability of SC-CO_2 has been evidenced in other supercritical assisted processes, mainly SC-CO_2 drying of alginate hydrogel beads (Della Porta *et al.*, 2013) and solvent elimination/killing in pharmaceutics compounds post-processing. But, it is the first time that this experimental evidence is shown for GO processing. It has very interesting implications from the point of view of GO purification and compatibilization with a biological environment, since Sulphur and Chlorine residues are cytotoxic.

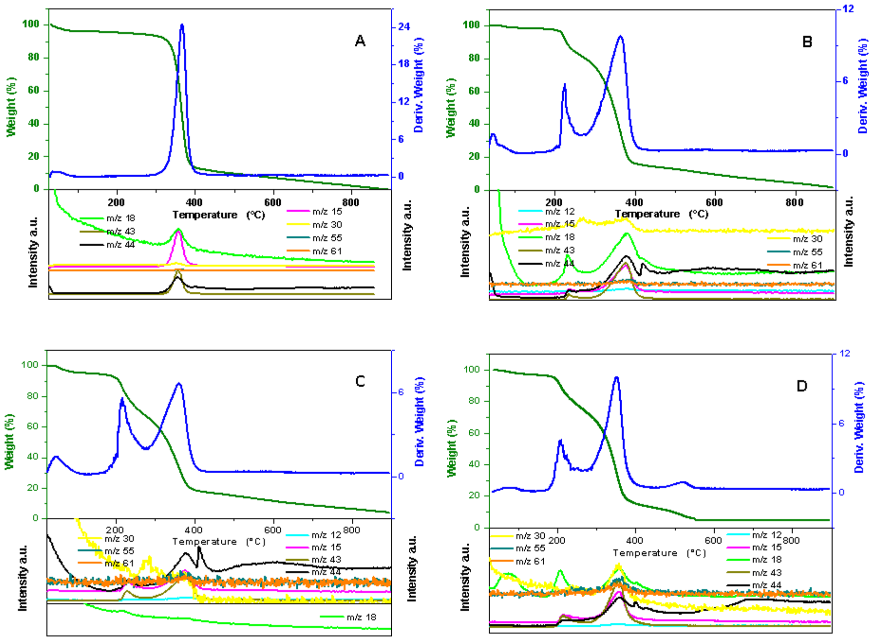

Figure V.24 *TG-DTG-MS profiles for CA (A), CA_GO_1 (B), CA_GO_2 (C), CA_GO_2_8h (D)*

To better understand the evolution of GO under SC-CO_2 process conditions, CA from CA_GO_2_8h was dissolved in NMP, and the TG-MS profiles, under a 1% v/v of O_2 in N_2 flow, of the recovered GO, reported as a function of temperature in Figure V.25. The weight loss due to the oxyfunctional groups results clearly reduced (compare with Figure V.18), moreover, the residue is considerably increased, likely due to a GO reduction. For GO thermal reduction under vacuum it has been reported (Ganguly *et al.*, 2011) that upon progressive thermal treatment: first of all, the in-plane -COOH groups become highly unstable; followed by a formation of phenolic groups and rapid removal of edge plane -C=0 at T<400 °C and basal plane -C=0 groups at T>400 °C; finally resulting in a little survival of phenolic groups. The profile of H_2O (m/z=18) (Figure V.25 bottom) observed in the temperature range 120-200 °C, for the recovered GO, likely suggests that it has reached an advanced level of reduction in which the surviving species are prevalently carbonyl groups. No trace of SO_2 (m/z=48, 64) and Chlorine (m/z=35) initially retained in GO can be seen, as already shown by the composites thermal analysis. Starting from the thermogravimetric residue in Figure V.24d (4.85% w/w, that is due to GO) and that in Figure V.25, we also measured the approximate GO amount in CA_GO_2_8h, that is 6.26% w/w.

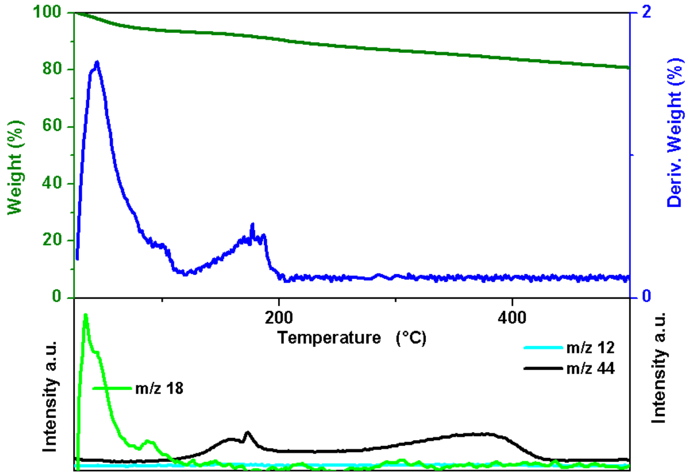

Figure V.25 *TG-DTG-MS profiles for GO from CA_GO_2_8h after CA removal in NMP*

Figure V.26A shows the XRD patterns of GO after CA structure dissolution in NMP from CA_GO_2_8h. It indicates a partial reduction of GO due to removal of oxyfunctional groups and intercalated water, confirming the indication of TG-MS analysis.

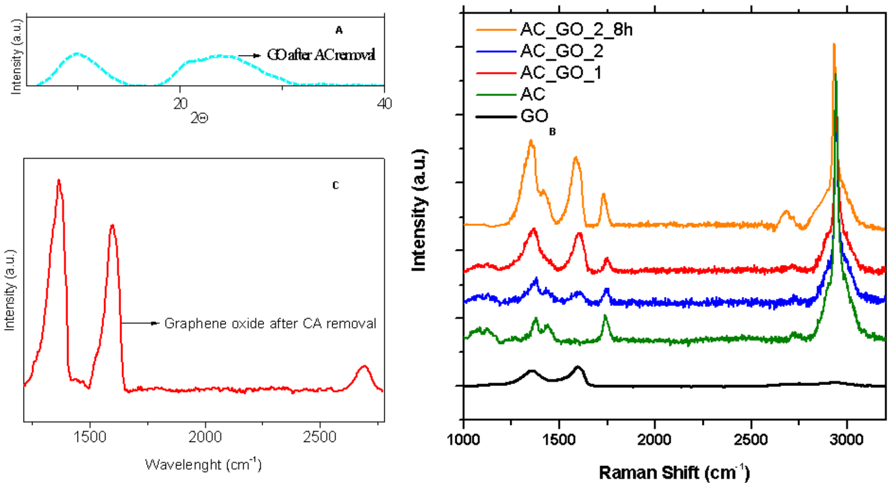

Figure V.26 *X-ray diffraction pattern of GO from CA_GO_2_8h, after a CA removal in NMP (A); Raman Spectra of GO, CA, CA_GO_1, CA_GO_2, CA_GO_2_8h (B) and GO, from CA_GO_2_8h, after a CA dissolution in NMP (C)*

Raman spectra of CA, and of the nanocomposites, in the wavenumber range 1000-3200 cm^{-1}, are shown in Figure V.26B. Spectrum in green exhibits typical Raman modes of CA. Both CA_GO_1 and CA_GO_2 show an additional Raman line at 1593 cm^{-1} (the G-line, due to the in plane vibration of the C–C bonds of GO), more pronounced at higher GO loading. The other typical GO band, at 1357 cm^{-1} (D line), is partially superimposed to the band at 1370 cm^{-1} of CA. In CA_GO_2_8h the G band down-shifts to a position close to the G band of graphite (1586 cm^{-1}), this is typical of reduced graphene (Wojtoniszak *et al.*, 2012b) and can be attributed to graphitic “self-healing” (Kudin *et al.*, 2008), while the 2D band is more pronounced (Ciambelli *et al.*, 2005). The Raman spectrum of GO, after the dissolution of CA in NMP, is shown in Figure V.26C, as observed in CA_GO_2_8h the G line is down-shifted and 2D band more pronounced. Moreover, D band at 1357 cm^{-1} becomes prominent, indicating that SC-CO$_2$ process influences the size of the in-plane sp^2 domains (Cançado *et al.*, 2011). In particular, an I_D/I_G ratio of 1.25 can be measured, indicating an increasing L_D distance. This value suggests again a partial GO reduction, in agreement with the results of TG-MS and XRD measurements, for reduced graphene oxide (rGO). Cui et al. (Cui *et al.*, 2011) found an I_D/I_G ratio of 1.4, a value of 1.9 was observed for rGO reduced by HI at 100 °C. However, it is difficult to compare the results, because the measurements are often recorded on GO with different edge thickness.

V.2.4 Conclusions and perspectives

Homogeneous CA/GO membrane-like composites were successfully prepared using a SC-CO$_2$ assisted phase separation, confirming the ability of supercritical processing to treat polymeric suspensions preventing stratification phenomena. The structures exhibited the cellular morphology observed for CA alone, also at the highest GO loadings (9% w/w). During the processing, the thin GO nanosheets were exfoliated by interaction with SC-CO$_2$ and their enclosure in the polymeric matrix also prevented their restacking.

S and Cl impurities, that were present in the starting GO material, were completely eliminated by SC-CO$_2$ during the structures formation, producing an improved material. This result is new and it can be very useful, for example, for biological applications of GO.

The partial reduction of GO to graphene has also been observed for the first time and could be modulated modifying the process conditions, for example, by varying pressure and duration of the SC-CO$_2$ assisted phase separation. It could be the basis for the formulation of a simpler technique to produce exfoliated graphene.

V.3 3-D PLLA scaffolds formation by a supercritical freeze extraction assisted process

The goal of this work is to propose a new SFEP for the formation of porous structures suitable for TE applications, that combines the advantages of TIPS process for the phase separation and 3-D structures formation, followed by immediate supercritical drying that can produce complete and fast solvent elimination avoiding structure collapse.

We will explore the feasibility of this process and the possibility of producing 3-D PLLA scaffolds characterized by a homogeneous microstructure suitable for cells colonization and growth, and nanostructured internal surfaces for cells interaction and guidance for their adhesion, migration, differentiation and organization. Supercritical drying parameters will be investigated to analyze their effect on the scaffolds integrity and morphology.

V.3.1 Preparation of PLLA scaffolds

Solutions of PLLA in chloroform with concentrations of 5, 10, 15 and 20% w/w were prepared. The solution was stirred at room temperature until it became homogeneous. It was, then, phase separated at -30 °C for 24 h and the samples were dried using SC-CO_2 pumped at a temperature of 35 °C for 4 h, using different process pressures of 100, 150, 200 and 250 bar.

The vessel was filled from the bottom with SC-CO_2 up to the desired pressure using a high pressure pump (Milton Roy-Milroyal B, Pont-Saint-Pierre, France). The pressure was controlled by a manometer and the temperature was set by a controller. A depressurization time of 10 min was used to bring back the system at atmospheric pressure. The temperature used was the lowest possible to maintain CO_2 at supercritical conditions and, at the same time, to avoid the PLLA glass transition temperature (60-65 °C) crossing during the process.

V.3.2 PLLA scaffold: results and discussion

We processed two different kinds of PLLA (L207s and L209s, see Materials and Methods section) using solutions in chloroform with different polymer concentrations ranging between 5 and 20% w/w. TIPS was performed at -30 °C; then, supercritical drying was immediately performed operating at different pressures, ranging between 100 and 250 bar. The time gap between TIPS and supercritical drying was minimized (about 60 s), since TIPS process is reversible and a temperature increase of the sample can modify the morphology of the phase-separated structures. SC-CO_2 at 35

°C was used in all the experiments, since this is the lowest temperature that can be safety used to maintain CO_2 at supercritical conditions; therefore, an initial large temperature difference between the drying medium and the sample was unavoidable and the feasibility of the process had to be verified.

Therefore, in the first part of the work, we studied the feasibility of the process and the effect of polymer concentration in the starting solution on the final scaffold morphology. The first series of experiments was performed on L207s PLLA using polymer concentrations between 5 and 20% w/w; drying was performed at 100 bar and 35 °C. As shown by FESEM images reported in Figure V.27, we generated homogeneous PLLA structures, characterized by cellular morphology and increasing the polymer concentration, the pore size largely decreased.

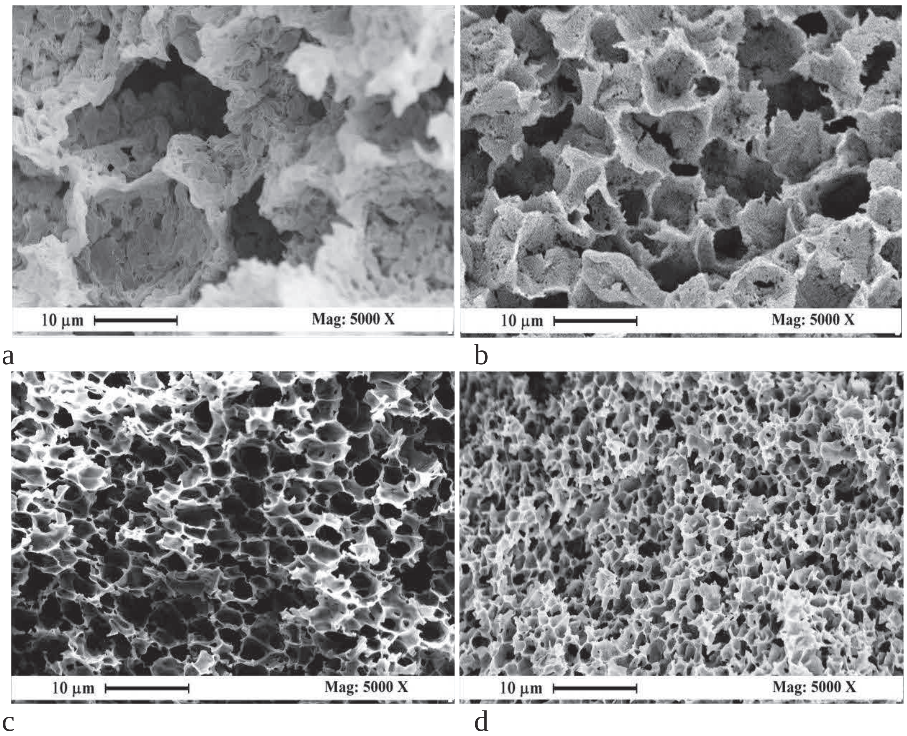

Figure V.27 *Sections of PLLA scaffolds obtained starting from solutions at different polymer concentrations: (a) 5% w/w, (b) 10% w/w, (c) 15% w/w, (d) 20% w/w, phase separated at -30 °C and dried by SC-CO_2 at 35 °C and 100 bar*

This information is qualitatively shown in Figure V.27, when FESEM images taken at the same enlargement were reported, and this evidence is quantitatively shown in Figure V.28, where pore size distributions are reported. Increasing from 5 to 20% w/w the concentration of the polymer, the mean pore size decreases from about 15 to 3 µm and pore size distribution shrinks.

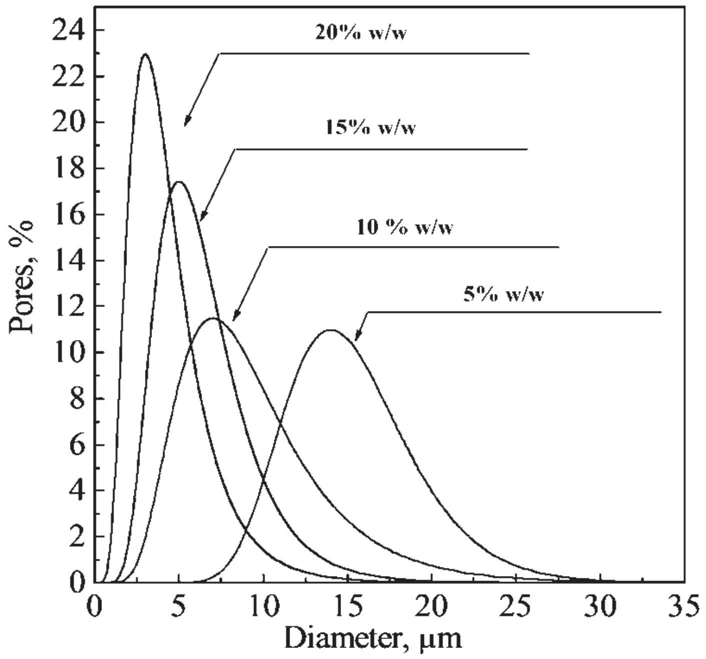

Figure V.28 *Pore size distribution in PLLA scaffolds obtained starting from different polymer concentrations*

Moreover, FESEM images show that, at the lowest PLLA concentration (5% w/w), there is a higher interconnection. This result has been confirmed by porosimetric analysis that measured a porosity ranging between 93% (for 5% w/w PLLA scaffold) and 84% (for 20% w/w PLLA scaffold). Observing FESEM images produced at larger magnifications, like the one reported for example in Figure V.29, it is possible to note that, in addition to the micrometric structure, pore walls are also characterized by a nanometric substructure in which pores of about 200 nm in diameter are present.

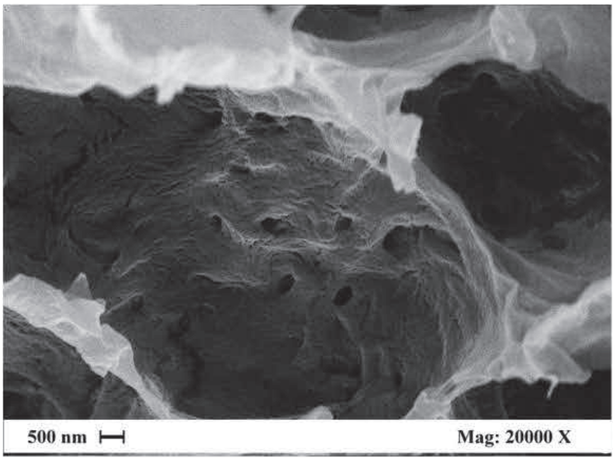

Figure V.29 *FESEM image at higher magnification of a 10% w/w PLLA scaffold, phase separated at -30 °C and dried by SC-CO_2 at 100 bar and 35 °C*

We also analyzed the scaffolds skin and verified that, increasing polymer concentration, the resulting skin morphology changed from dense to porous (see FESEM images in Figure V.30).

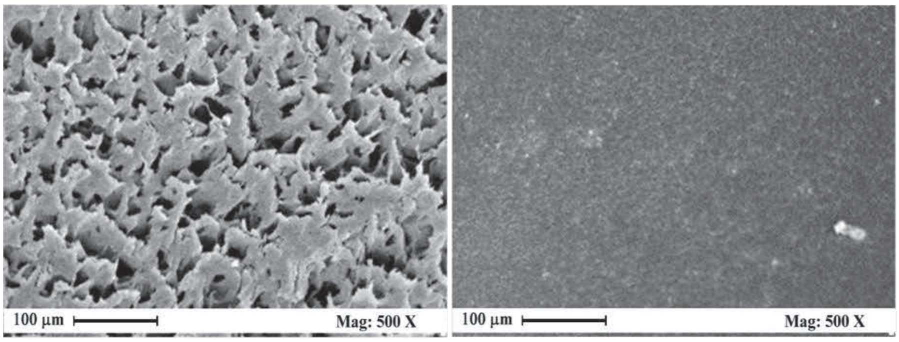

a b

Figure V.30 *PLLA scaffold surfaces obtained starting from (a) 10% and (b) 20% w/w polymer concentration, processed at 100 bar and 35 °C*

The formation of porous skins is difficult to be obtained using the traditional procedures; i.e., TIPS process coupled with the freeze drying. Since the possibility of obtaining a 3-D structure is relevant for TE applications when, for example, bones have to be regenerated, we also focused our attention on the size and shape of the structures generated. We measured the size and the shape of the samples after TIPS and after supercritical drying, verifying that the structure did not modify after supercritical processing. Operating in this manner, cylindrical scaffolds of 4 mm thickness and 2 cm diameter were obtained and their size and shape were preserved. Larger structures can be also obtained; indeed, cylindrical scaffolds of 2 cm of thickness and 2 cm of diameter were generated in other experiments too. We measured the compressive modulus of some of the scaffolds obtained to verify if mechanical resistance is compatible with the one required for scaffolding applications. To obtain a statistically significant value, the compressive modulus was measured on 5 identical samples (2 cm x 4 mm) for each scaffold produced. The scaffolds obtained starting from 5% w/w of polymer show a mean compressive modulus of 103 kPa; 10% w/w scaffolds show a mean compressive modulus of 138 kPa, whereas a mean compressive modulus of 147 kPa was obtained for 20% w/w scaffolds. This result can be easily explained considering that, when the scaffolds are obtained starting from a more concentrated polymeric solution, the higher percentage of polymer in the scaffold gives higher resistance to the structure. The required mechanical resistance depends on the organs to be repaired; for example, 100 kPa are necessary for bone TE applications (Reverchon *et al.*, 2008). Solvent residue analysis was also performed as described in Materials and Methods and chloroform residue present in the scaffolds was found to be lower than 5 ppm.

In a second series of experiments, the effect of PLLA molecular weight was analyzed, processing two kinds of PLLA: L207s and L209s, characterized by molecular weight ranging between 85,000-160,000 Da and between 150,000-200,000 Da, respectively. Observing FESEM image reported in Figure V.31, related to a PLLA L209s scaffold, dried at 100 bar and 35 °C, using a 15% w/w polymeric solution, it is possible to note that similar morphology and pore sizes were obtained with respect to the PLLA L207s scaffolds previously reported (Figure V.27b). This result was confirmed at all concentrations and process conditions tested in this work, showing that the molecular weight should be not a relevant parameter for the present product.

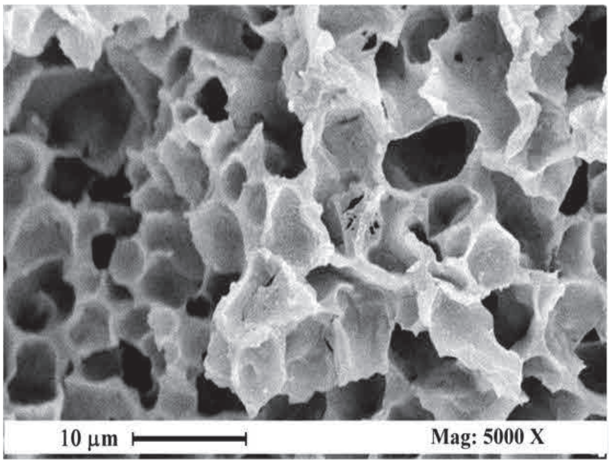

Figure V.31 *L209s PLLA scaffold section dried at 100 bar and 35 °C, 15% w/w PLLA*

In the last part of the work we studied the effect of the operative pressure on PLLA scaffolds morphology, during the supercritical drying, testing pressures ranging between 100 and 250 bar. Since the solid PLLA structures are formed during the TIPS step, as expected, the scaffolds morphology did not vary with the drying pressure and was cellular at all polymer concentrations. However, observing the skin of the PLLA scaffolds, we verified as their morphology drastically changed; indeed, operating at 100 bar, a dense skin was obtained (Figure V.30b), whereas increasing the pressure up to 250 bar, a porous skin was generated (Figure V.32).

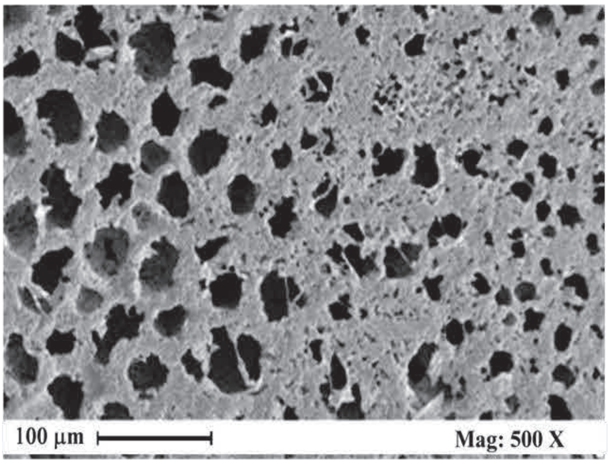

Figure V.32 *PLLA scaffold skin (20% w/w) obtained drying the structure at 250 bar and 35 °C*

The results obtained in this study can be explained considering the classical theory of the phase separation process. The cellular structure suggests that a liquid-liquid phase separation occurred during TIPS (van de Witte *et al.*, 1996b). Moreover, the presence of a nano substructure is usually related to a solid-liquid demixing mechanism (van de Witte *et al.*, 1996b; Reverchon *et al.*, 2006a; Reverchon *et al.*, 2006d); therefore, an overlap of a solid-liquid demixing with the liquid-liquid demixing can be hypothesized during TIPS of PLLA samples.

To better understand the mechanism, it is possible to consider a qualitative binary diagram in which both liquid-liquid demixing gap and gelation or crystallization curve (responsible of solid-liquid demixing) are present. In Figure V.33 a hypothetic binary diagram “polymer concentration vs temperature” has been reported. The diagram is characterized by a homogenous region and two demixing regions: the solid-liquid demixing, bordered by the crystallization/gelation/solidification curve, and the liquid-liquid demixing, bordered by the binodal curve (the external one) and the spinodal curve (located inside the binodal).

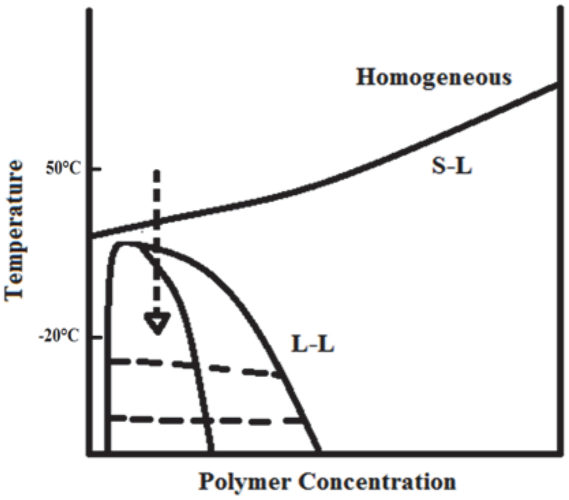

Figure V.33 *Qualitative binary diagram for the system PLLA-Chloroform*

The fact that all the samples contain also the nano substructure, suggests that solid-liquid demixing also occurred, overlapping the liquid-liquid demixing; i.e., the gelation (or crystallization/solidification) curve is next to the liquid-liquid demixing gap; as a consequence, the “composition pathway”, driven by temperature decrease (dashed line starting from point A), crosses both curves during the process.

For comparison purpose, we also performed supercritical induced phase separation (SC-IPS) experiments on the same polymeric solutions, operating at 200 bar and 35 °C. Similar structures were obtained (i.e., cellular structures as in the TIPS process); but, smooth pores were generated, confirming that, in that case, only liquid-liquid (i.e., liquid-supercritical fluid) phase separation occurred. To compare SFEP with SC-IPS process, we have to consider that a ternary system PLLA/chloroform/SC-CO_2 is involved, due to the active role of SC-CO_2 during the process (as the non-solvent), differently from what occurred in SFEP. The obtained morphology suggests different relative positions between the solid-liquid (i.e., in this case, solid-supercritical fluid) and the liquid-liquid (i.e., liquid-supercritical fluid) demixing curves, with respect to the PLLA-chloroform binary system (Figure V.33). In Figure V.34, a qualitative ternary diagram is reported, in which the solid-liquid demixing curve is located "behind" and "far from" the liquid-liquid demixing curve; therefore, the "solution pathway" (dashed line starting from point B), driven by the solution composition modification, does not cross it during the phase separation process.

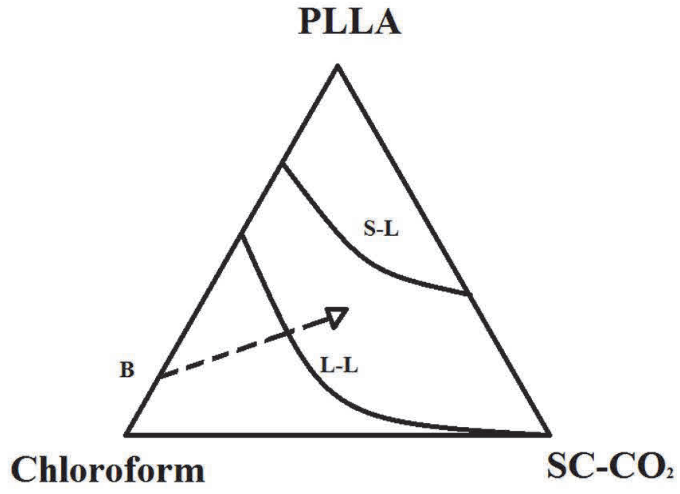

Figure V.34 *Qualitative ternary diagram for the PLLA/Chloroform/SC-CO_2 system*

Regarding the effect of the polymer concentration in the starting solution, it is known that a decrease of the starting polymer concentration leads to a reduction of polymer-rich phase during the phase separation (van de Witte *et al.*, 1996b; Reverchon *et al.*, 2004). Obviously, this phenomenon causes an increase of pore size and a larger porosity.

The effect of supercritical processing pressure after TIPS was not surprising; indeed, it shows as supercritical drying preserved the solid structures; however, it also affects their surface characteristics: increasing SC-CO_2 pressure, at high polymer concentrations (20% w/w), it is possible to modify the scaffolds skin (Figures V.30b, V.32), and can be relevant from a TE application point of view to generate an environment able to promote cells nutrients and wastes diffusion. This result can be explained considering the increase of solvent power of SC-CO_2 when pressure is increased: an increase of the solvent power can cause a partial solubilization of the polymer at the beginning of the drying process; in this way, the thin skin generated during TIPS is partly dissolvent and the porous structure becomes visible also on the scaffold surface.

V.3.3 Conclusions

We demonstrated that using TIPS followed by SC-CO_2 drying, it is possible to produce PLLA scaffolds characterized by a micrometric cellular structure and wrinkled pore walls. The low temperature process allows to obtain 3-D solids, whose structure is preserved during supercritical drying. This last characteristic cannot be obtained using traditional or supercritical processes based on solvent-non solvent phase separation that involve a liquid phase that can produce only flat, prevalently bi-dimensional structures.

V.4 3-D PLLA/Ibuprofen composite scaffolds obtained by a supercritical fluids assisted process

In this study, for the first time, the possibility of generating a 3-D PLLA scaffold loaded with an active compound by SFEP has been evaluated. The effects of process parameters on the scaffolds morphology, the drug distribution and the drug release have been studied.

V.4.1 Preparation of PLLA composite scaffolds

Solutions of PLLA in chloroform with concentrations of 5, 10 and 15% w/w were prepared. Subsequently, ibuprofen was solubilized in the polymeric solution with a concentration of 10% w/w with respect to the polymer. The ternary solution was stirred at room temperature until it became homogeneous. It was, then, phase separated at -30 °C for 24 h and the samples were dried using SC-CO_2 at different temperatures (ranging from 35 to 55 °C) and different pressures (ranging between 100 and 200 bar) for 4 h. The vessel was filled from the bottom with SC-CO_2 up to the desired pressure using a high pressure pump (Milton Roy-Milroyal B, Pont-Saint-Pierre, France). The pressure was controlled by a manometer and the temperature was set by a controller. A depressurization time of 15 min was used to bring back the system at atmospheric pressure.

V.4.2 PLLA composite scaffold: results and discussion

We processed PLLA + ibuprofen solutions in chloroform with different polymer concentrations ranging between 5 and 15% w/w and with a fixed amount of drug, 10% w/w respect to PLLA. TIPS was obtained at -30 °C for 24 h; then, supercritical drying was immediately performed operating at different pressures, ranging between 100 and 200 bar, and different temperatures, ranging between 35 and 55 °C. The time gap between TIPS and supercritical drying was minimized (about 50 s), since TIPS process is reversible and a temperature increase of the sample can modify the morphology of the phase-separated structures.

The possibility of generating 3D structure is relevant for TE applications; for this reason, first of all, we focused our attention on the size and shape of the structures generated. We measured the size and the shape of the samples after TIPS and after supercritical drying, verifying that the structure did not modify after supercritical processing. Cylindrical composite scaffolds of 4 mm thickness and 2 cm diameter were obtained and their size and shape were preserved. Then, we studied the effect of polymer concentration in the starting solution on the final composite scaffolds morphology.

The first series of experiments was performed using polymer concentrations between 5 and 15% w/w; supercritical drying experiments were performed at different pressures and temperatures. An example is reported in FESEM images (taken at the same enlargement) of Figure V.35, where PLLA/ibuprofen composite scaffolds obtained at 45 °C and 150 bar at different polymer concentrations are presented.

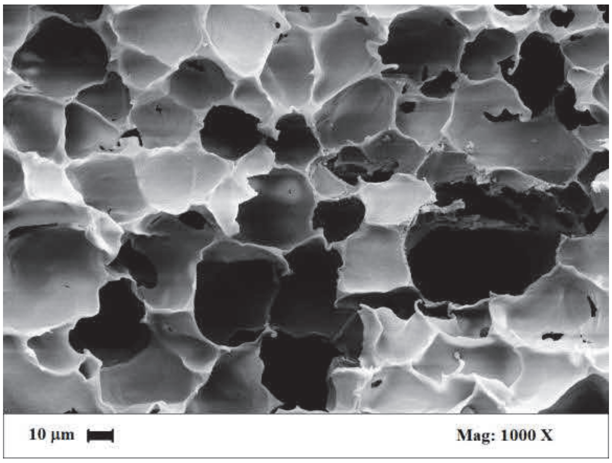

a

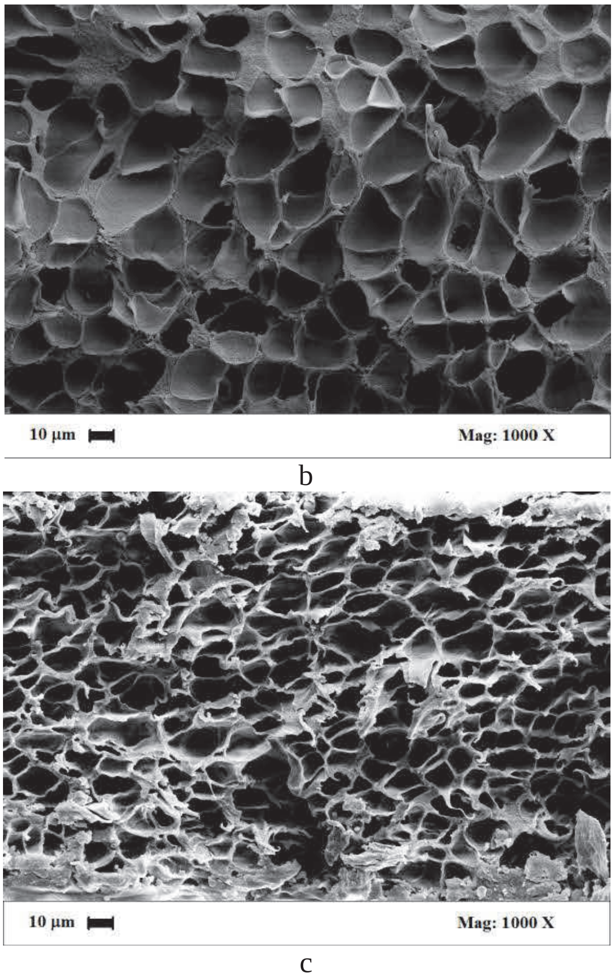

Figure V.35 *Sections of PLLA/ibuprofen composite scaffolds obtained starting from solutions at different polymer concentrations: a) 5% w/w, b) 10% w/w, c) 15% w/w, phase separated at -30 °C and dried by SC-CO_2 at 45 °C and 150 bar*

Homogeneous structures characterized by a cellular morphology were generated; the presence of drug is not detectable by FESEM analysis and the results obtained put in evidence the fact that the drug did not interfere with the scaffolds formation.

Increasing the polymer concentration, the pore size largely decreased; this information is qualitatively shown in Figure V.35, where FESEM images taken at the same enlargement were reported, and it is quantitatively shown by pore size distributions in Figure V.36.

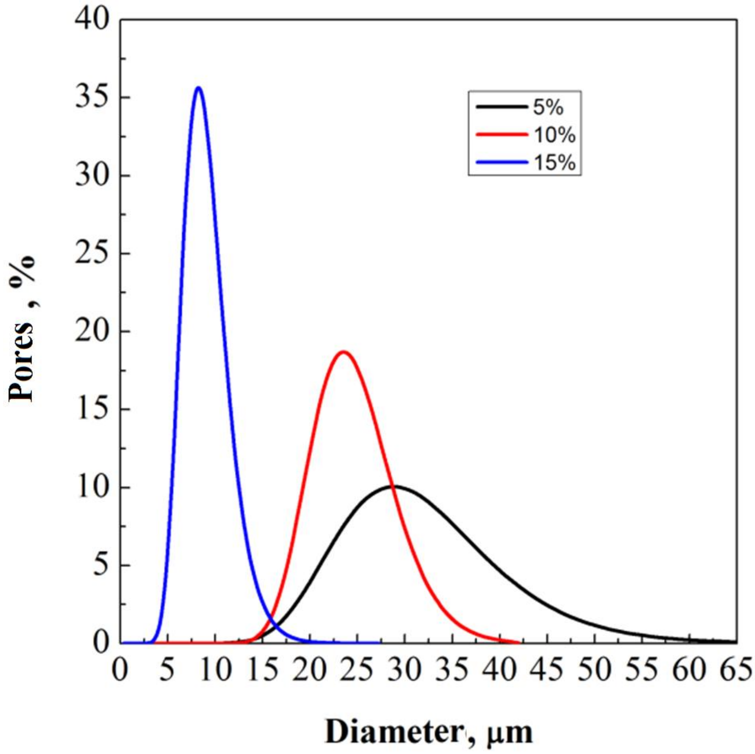

Figure V.36 *Pore size distribution of PLLA/ibuprofen composite scaffolds obtained starting from different polymer concentrations*

Increasing from 5 to 15% w/w PLLA concentration, the mean pore size decreases from about 30 to 8 μm and pore size distribution shrinks. Moreover, porosimetric analysis measured a porosity ranging between 89% (for 5% w/w PLLA scaffold) and 78% (for 15% w/w PLLA scaffold). Observing FESEM images produced at higher magnifications, like the one reported in Figure V.37, it is possible to note that, in addition to the micrometric structure, pore walls were also characterized by a nanometric substructure in which pores and fibers of about 100 nm in diameter are present.

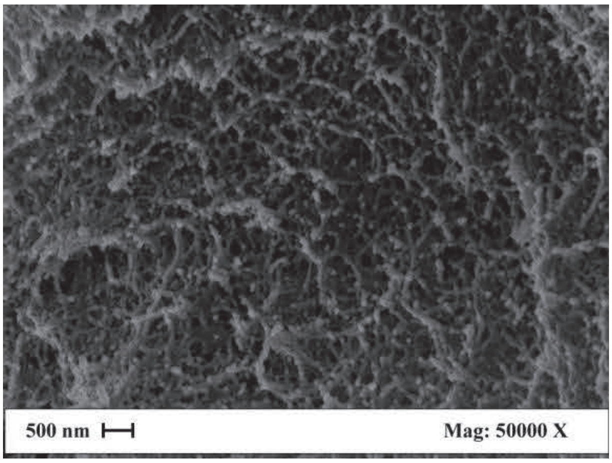

Figure V.37 *FESEM image at higher magnification of a 15% w/w PLLA/ibuprofen composite scaffold, phase separated at -30 °C and dried by SC-CO_2 at 150 bar and 45 °C*

We also analyzed the scaffolds skin and verified that, increasing the polymer concentration, the resulting skin morphology changed from dense (for 15% w/w of PLLA) to dense with isolated pores (for 10% w/w of PLLA) to porous (for 5% w/w of PLLA), as it is possible to observe in FESEM images reported in Figure V.38.

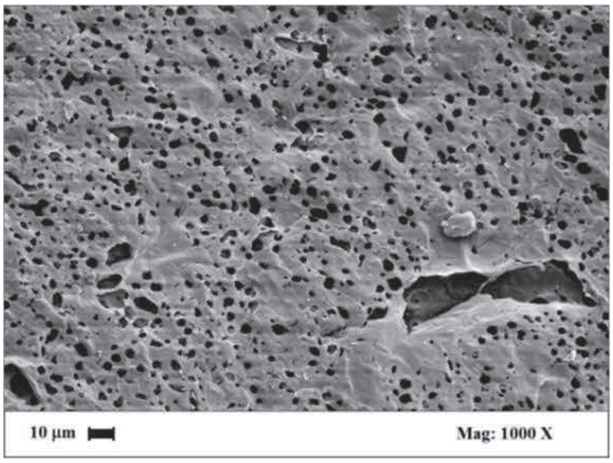

a

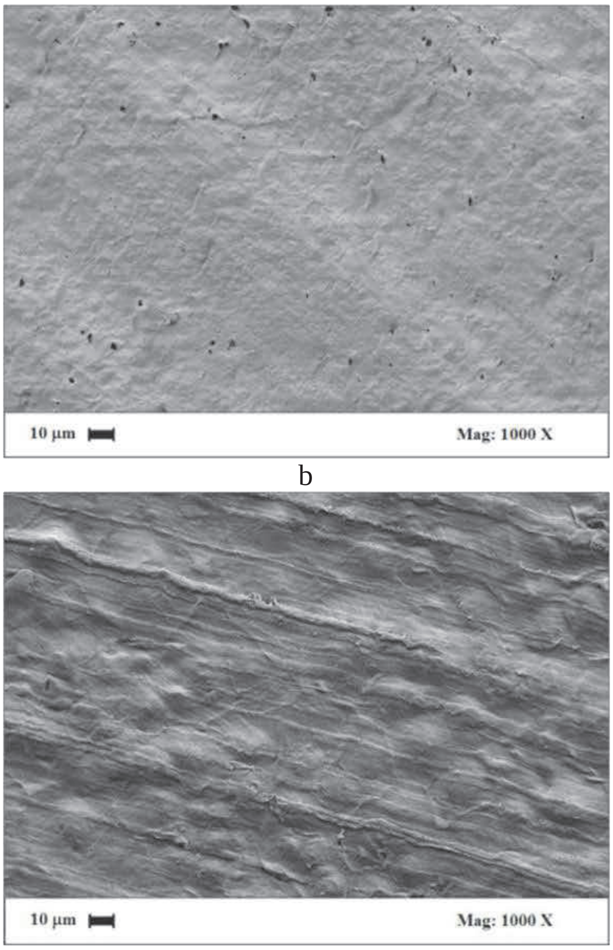

c

Figure V.38 *PLLA/ibuprofen composite scaffold surfaces obtained starting from a) 5% w/w, b) 10% w/w, c) 15% w/w polymer concentration, with 10% w/w of ibuprofen, dried at 100 bar and 45 °C by SC-CO_2*

Solvent residue analyses were also performed and values of chloroform lower than 5 ppm were found; i.e., as expected, supercritical drying allowed to completely remove the organic solvent of the starting solutions. Qualitative and quantitative analysis on PLLA/ibuprofen scaffolds were also performed; in particular, ibuprofen distribution along the scaffold was evaluated by EDX analysis. In Figure V.39, element maps of PLLA/ibuprofen composite scaffolds obtained at 150 bar and 55 °C are reported.

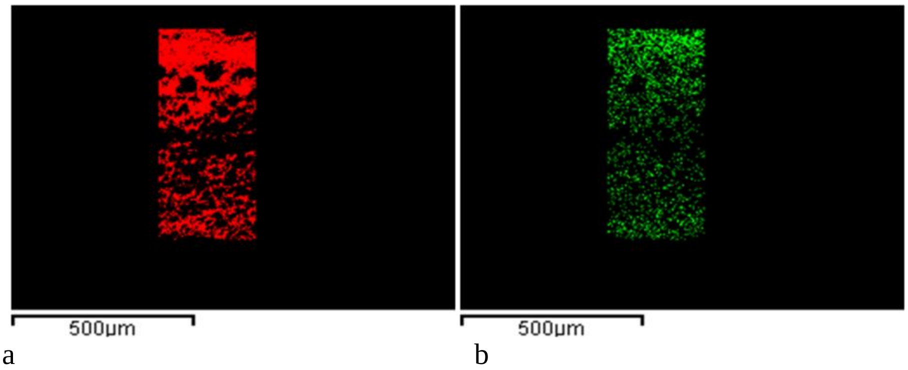

Figure V.39 *EDX analysis of PLLA/ibuprofen composite scaffolds obtained at 150 bar and 55 °C; a) red: Carbon map, b) green: Sodium map*

The drug (green map) is uniformly distributed along the scaffold section and completely overlap the presence of polymer (red map); this result is extremely important because confirms that the SFEP process allows to obtain polymer/drug composite scaffolds characterized by a homogenous distribution of the active compound. This result was observed for each operating condition tested and at all polymer concentrations.

These results can be explained considering the classical theory of the phase separation process. The cellular structure suggests that a liquid-liquid phase separation occurred during TIPS (van de Witte *et al.*, 1996b; Cardea *et al.*, 2014a). Moreover, the presence of a nano substructure is usually related to a solid-liquid demixing mechanism (van de Witte *et al.*, 1996b; Reverchon *et al.*, 2004; Reverchon *et al.*, 2006b); therefore, an overlap of a solid-liquid demixing with the liquid-liquid demixing can be hypothesized during TIPS of PLLA/ibuprofen samples.

Regarding the effect of the polymer concentration in the starting solution, it is known that a decrease of the starting polymer concentration leads to a reduction of polymer-rich phase during the phase separation (van de Witte *et al.*, 1996b; Reverchon *et al.*, 2006d). Obviously, this phenomenon causes an increase of pores size and a larger porosity. The fact that the drug is not distinguishable in the polymeric matrix by FESEM analysis can be explained considering that it is solubilized with the polymer in the starting solution; as a consequence, it forms a solid solution with the polymer in the final composite scaffold; i.e., there are molecular bonds between PLLA and ibuprofen.

Subsequently, the effect of the supercritical drying pressure on the composite scaffolds morphology was studied. Analyzing the experiments performed at 35 °C and with 15% w/w of PLLA (and 10% w/w of ibuprofen respect to PLLA), we observed that an increase of pressure from 100 to 200 bar did not affect the scaffolds morphology; indeed, a cellular structure was always obtained and this result was confirmed at each polymer concentration and temperature tested. Moreover, the pores size did not vary too. This result is qualitatively visible in Figure V.40, where FESEM images of PLLA/ibuprofen composite scaffolds obtained at different pressures are reported, and quantitatively confirmed by pore size distribution reported in Figure V.41.

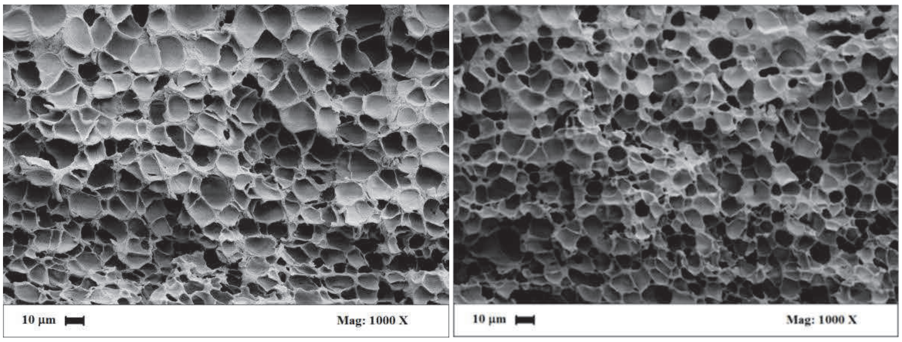

a b

Figure V.40 *PLLA/ibuprofen composite scaffolds obtained at 15% w/w of PLLA, 35 °C and at different pressures: (a) 100 bar; (b) 200 bar*

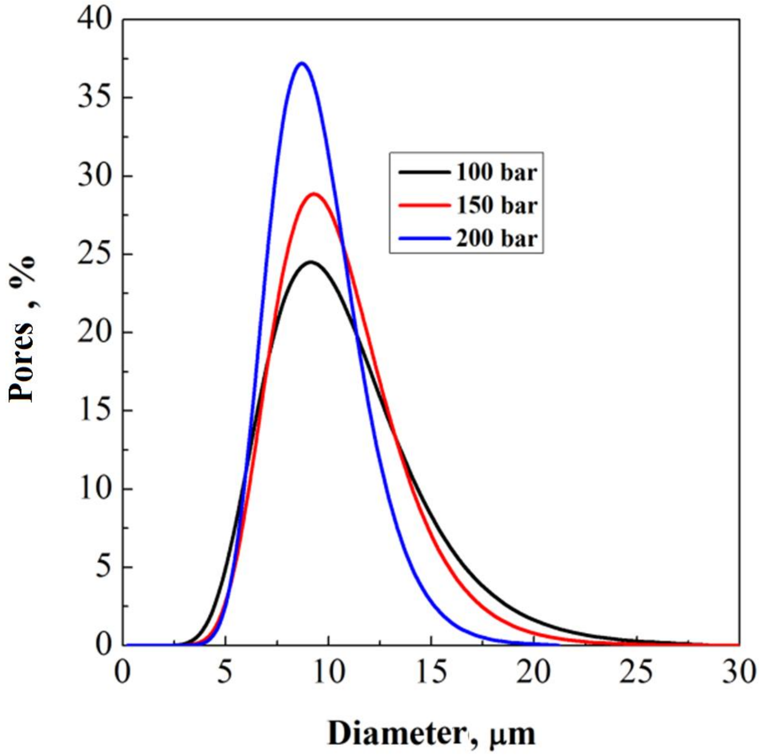

Figure V.41 *Pore size distributions of PLLA/iburprofen composite scaffolds obtained at 15% w/w of PLLA, 35 °C and at different pressures (100, 150 and 200 bar)*

We also analyzed the effect of supercritical drying temperature on composite scaffolds morphology. Also in this case, we always obtained cellular structures for each process condition tested. An example is reported in Figure V.42, where PLLA/ibuprofen composite scaffolds obtained at different drying temperatures (from 35 to 55 °C), 100 bar and 15% w/w of polymer are shown.

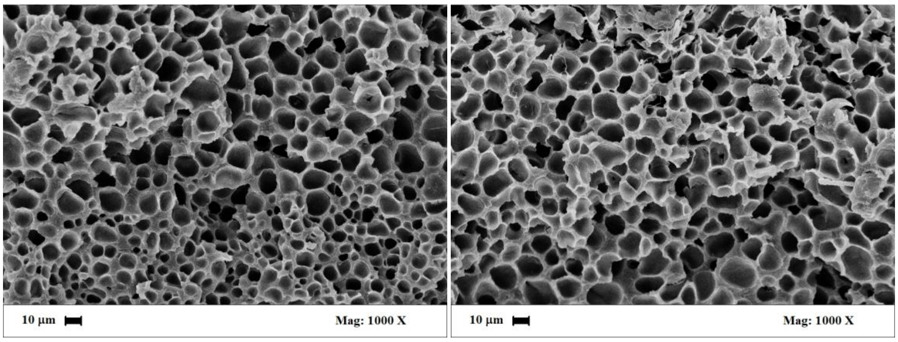

a b

Figure V.42 *PLLA/ibuprofen composite scaffolds obtained at 15% w/w of PLLA, 100 bar and at different temperatures: (a) 35 °C; (b) 55 °C*

Pore size analysis was also performed and the results confirmed what observed in FESEM images. In Figure V.43, it is possible to note that the pore size mean diameter did not change with drying temperature and the distribution curves are very similar.

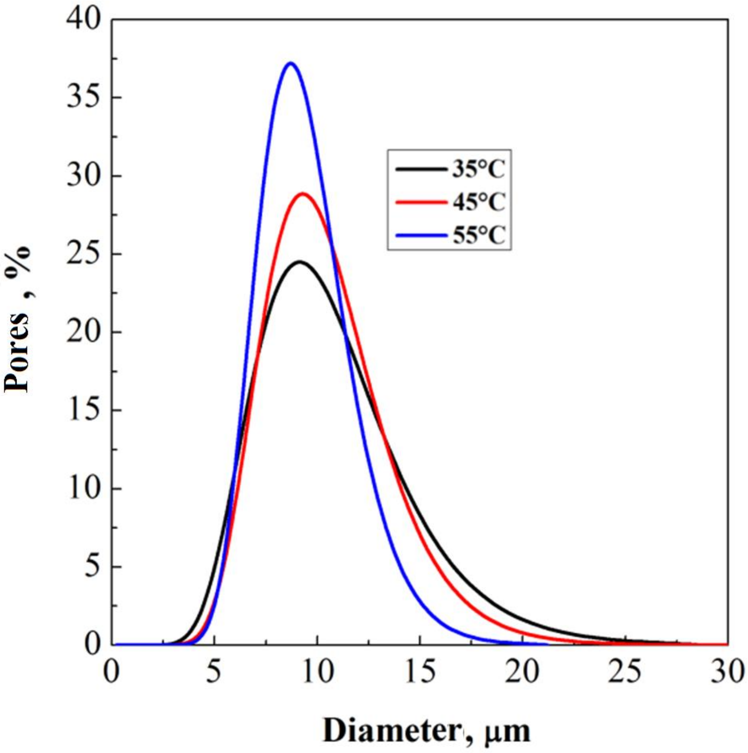

Figure V.43 *Pore size distributions of PLLA/ibuprofen composite scaffolds obtained at 15% w/w of PLLA, 100 bar and at different temperatures (35, 45 and 55 °C)*

The limited effect of supercritical processing parameters after TIPS was not surprising; indeed, it shows that supercritical drying preserved the solid structures and their morphology; but, it was not able to modify them, that are completely formed during TIPS step.

In the last part of the work, we focused our attention on the controlled release of the active compound; i.e., ibuprofen, from PLLA matrix. *In vitro* release rate assays were performed according to this procedure: the drug loaded scaffold was immersed in a glass bottle containing a physiological saline solution (pH 7.2) as drug releasing medium (1000 mL). The bottle was sealed and placed in an oven at 37 °C and shaken at 200 rpm. At predetermined time intervals, the concentration of drug was assayed using a UV/Vis spectrophotometer.

First, the effect of the polymer concentration on the drug release was studied. In Figure V.44, the drug release profiles from PLLA scaffolds obtained at 150 bar and 45 °C are reported.

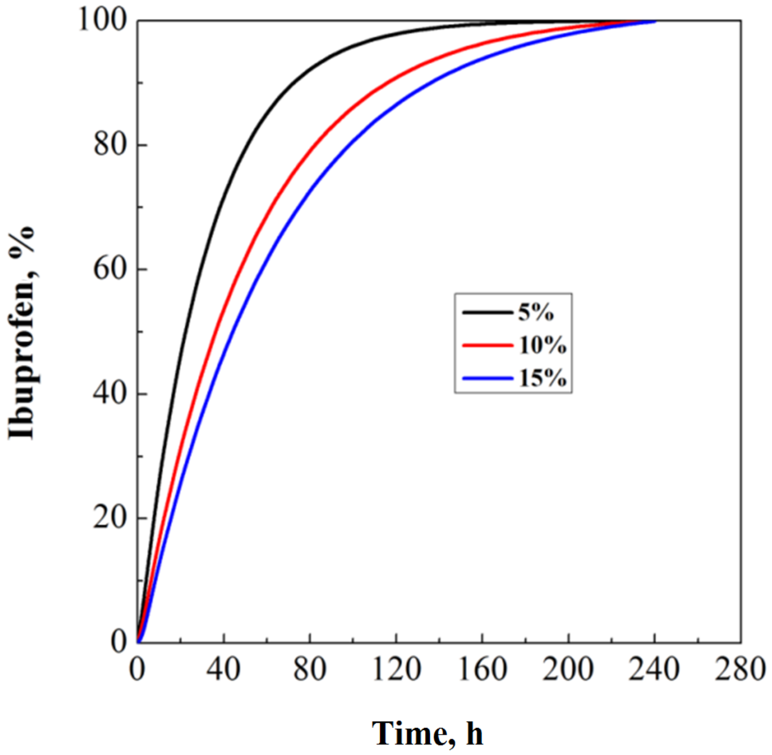

Figure V.44 *Ibuprofen release profiles from PLLA scaffolds with different polymer concentrations (from 5 to 15% w/w) obtained by supercritical drying at 150 bar and 45 °C*

It is possible to observe as, increasing the polymer concentration from 5 to 15% w/w, the drug release rate changes. In particular, the ibuprofen release rate increases when the polymer concentration decrease; for example, after 80 h of analysis, the 5% w/w PLLA scaffold released about 90% of drug, the 10% w/w PLLA scaffold released about the 80% of the drug, and the 15% w/w PLLA scaffold released about the 70% of the drug. Moreover, it is possible to put in evidence that the 100% of drug is released in about 160 h for 5% w/w PLLA scaffold and in about 240 h for 10 and 15% w/w PLLA scaffold. This behavior was observed for each operating condition tested. As expected, the homogenous distribution of the drug, observed by EDX analysis, avoided problems of burst effect.

The obtained result can be explained considering that the scaffolds produced starting from more diluted solutions (for example, 5% w/w PLLA) presented porous skin and larger pores as observed in Figures V.35a, V.38a, that facilitated physiological solution diffusion inside the scaffolds and drug contra-diffusion out of the scaffolds. Otherwise, scaffolds obtained starting from more concentrated solution (for example, 15% w/w of PLLA) presented dense skin and smaller pores, limiting physiological solution and drug diffusion in and out the structure.

Subsequently, FESEM analyses were performed on the scaffolds after the ibuprofen release to verify the effect of drug release on scaffolds morphology. In Figure V.45, FESEM images of a 15% w/w PLLA scaffold, obtained at 200 bar and 45 °C, before and after the drug release, are reported.

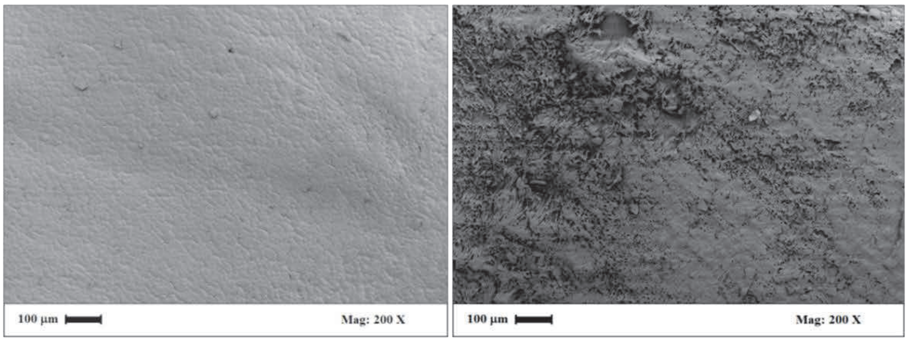

a b

Figure V.45 *Skin of 15% w/w PLLA scaffolds obtained at 200 bar and 45 °C, before (a) and after (b) the drug release*

It is possible to put in evidence that the scaffold skin morphology changed after the drug release, becoming opener. On the contrary, the scaffold inner section did not show significant modifications. The presence of “new” pores on the scaffold surface gives us important information about the drug release mechanisms in the case of high PLLA concentration scaffolds. Indeed, probably part of the drug is entrapped on the scaffold surface and is released in the physiological solution during the first part of the analysis. In this way, the surface becomes porous favoring the physiological solution diffusion inside the scaffolds and the contra-diffusion of the drug. This phenomenon explain how the dense skin scaffolds (i.e., 15% w/w of PLLA) were able to release all the drug.

We also analyzed the effect of supercritical drying pressure and temperature on drug releases. As expected, the ibuprofen releases obtained starting from scaffolds dried at different pressures and temperatures present similar trends. Indeed, as observed before, the supercritical drying operative parameters did not affect the scaffolds morphology and the pore size, indeed, the drug release curves almost overlap. This result is well-evidenced observing Figures V.46a, b, where ibuprofen release profiles from scaffolds obtained starting from 5% w/w PLLA, at 35 °C and different pressures (Figure V.46a) and starting from 10% w/w PLLA, at 150 bar and different temperatures (Figure V.46b) are reported.

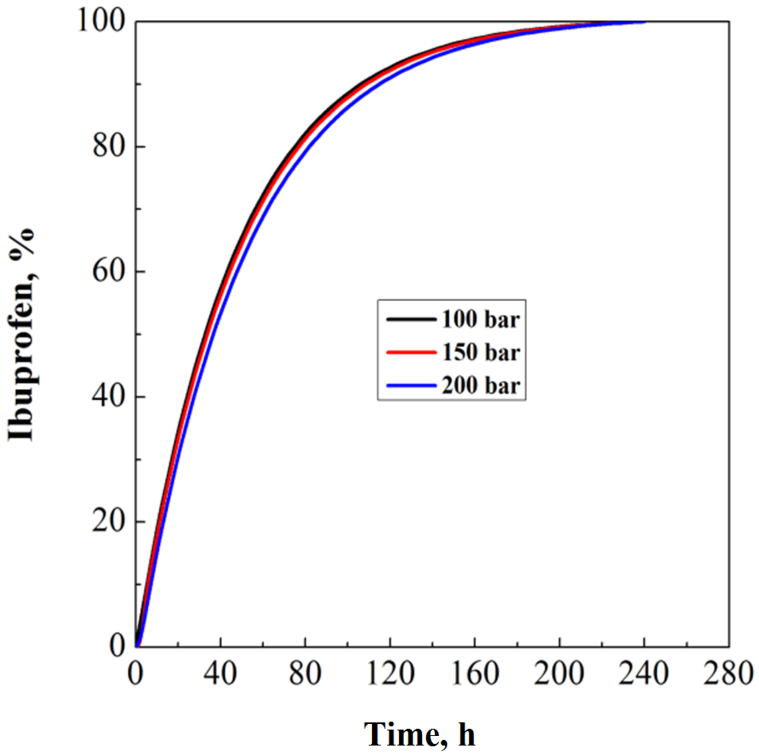

a

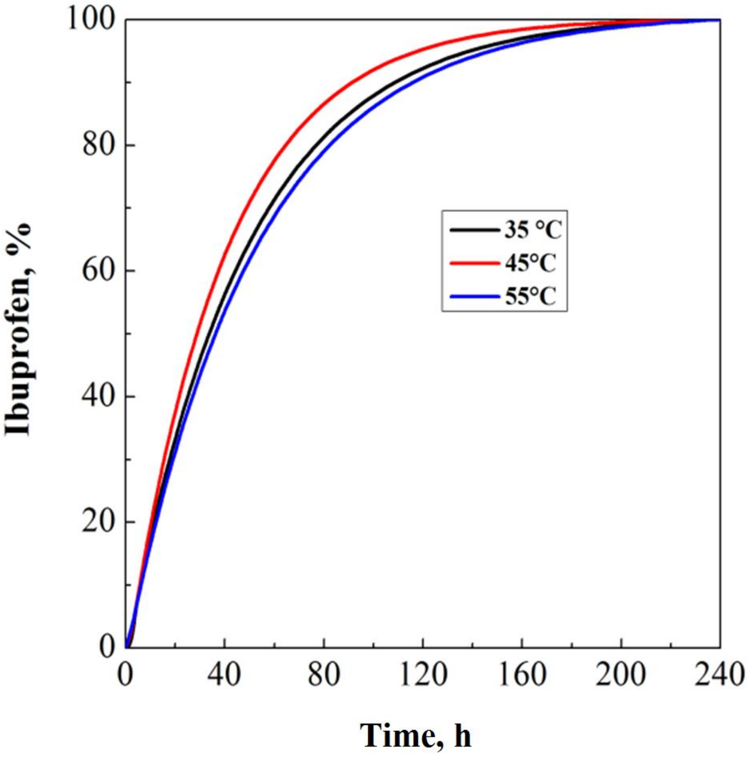

b

Figure V.46 *Ibuprofen release profiles from scaffolds obtained starting from 5% w/w PLLA, at 35 °C and different pressures (a) and starting from 10% w/w PLLA, at 150 bar and different temperatures (b)*

The proposed results confirmed what reported before: the supercritical drying temperature and pressure have no effect on the scaffolds morphology and, as a consequence, they did not affect the drug release rate.

V.4.3 Conclusions

SFEP confirmed to be a very promising process to generate polymeric scaffolds characterized by a 3-D geometry (due to low temperature process combined with supercritical drying), micrometric cellular structures and wrinkled pore walls. In particular, the possibility of generating polymer/drug composite scaffolds has been showed, assuring homogeneous distribution and controlled release of the active compound.

V.5 Chitosan scaffolds formation by a supercritical freeze extraction process

The aim of this work is to propose a SFEP for the formation of porous structures suitable for TE applications. It combines the TIPS process with supercritical drying and can produce a complete and fast solvent elimination, avoiding the structure collapse. We will explore the possibility of producing 3-D chitosan scaffolds characterized by a homogeneous microstructure, suitable for cells colonization and growth, and by a nanoporous sub-structure for cells interaction and guidance for adhesion, migration and differentiation.

Preliminary cells cultivation tests on hMSCs will be presented to evaluate first cell interactions with the produced structures.

V.5.1 Chitosan scaffolds preparation

Chitosan (Medium M_w) solution was prepared by dissolving chitosan (between 2 and 10% w/w) in water:acetic acid solutions with volume ratios of 99:1, 97:3 and 95:5; these solutions were stirred at 100 rpm and heated at 50 °C until they became homogenous. Then, they were poured in steel containers with an internal diameter of 2 cm and height of 1 cm and were phase-separated at a temperature of -20 °C for 24 h. Subsequently, the sample was put in a bath of acetone at -20 °C for 24 h to “substitute” water and, then, it was dried using SC-CO_2. SC-CO_2 drying was performed according to the following procedure: the steel containers were loaded on a metallic support that was, then, put in the high pressure vessel. The vessel was closed and filled from the bottom with SC-CO_2. When the required pressure and temperature were obtained (200 bar and 35 °C), drying was performed with SC-CO_2 at a flow rate of about 1 kg/h, that corresponds to a residence time inside the vessel of about 4 min; the drying lasted 5 h. A depressurization time of 20 min was used to bring back the system at atmospheric pressure.

V.5.2 Chitosan scaffolds: results and discussion

We processed chitosan using water:acetic acid solutions with different acetic acid percentages ranging between 99:1 and 95:5 and using polymer concentrations from 2 to 10% w/w. TIPS was performed at -20 °C; then, an acetone-water substitution step was carried out at the same temperature to eliminate water. Supercritical drying was performed operating at 200 bar and 35 °C. These process conditions were adopted for all the experiments in this work, since 35 °C is one of the lowest temperatures that can be used to maintain CO_2 at supercritical conditions, and 200 bar is a pressure that has been successfully tested in the SC-drying of other hydrogels (Della Porta *et al.*, 2013). Therefore, an initial large temperature difference between the drying medium and the sample was unavoidable and the processability had to be verified. Thus, in the first part of the experimentation, we studied the feasibility of the process and the effect of polymer concentration (from 2 to 10% w/w) in the starting solution on the final scaffold morphology, fixed the water:acetic acid ratio at 97:3.

As shown by FESEM images reported in Figure V.47, two different morphologies were generated: a bicontinuos structure for 2% w/w chitosan samples in water + acetic acid (Figure V.47a) and cellular structures for 5 and 10% w/w chitosan (Figures V.47b and c); moreover, increasing the polymer concentration, the pore size largely decreased and the scaffold structure became more uniform and homogeneous.

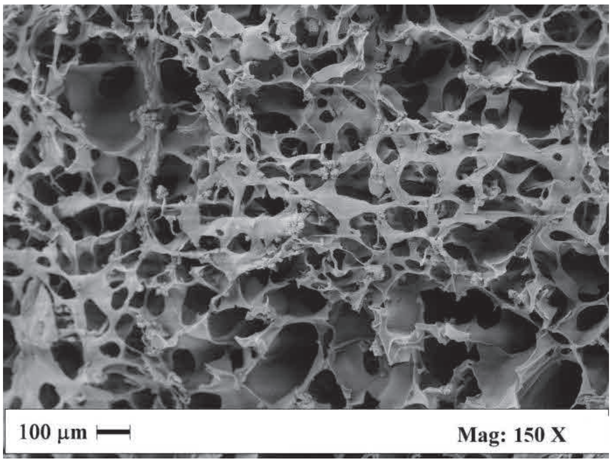

a

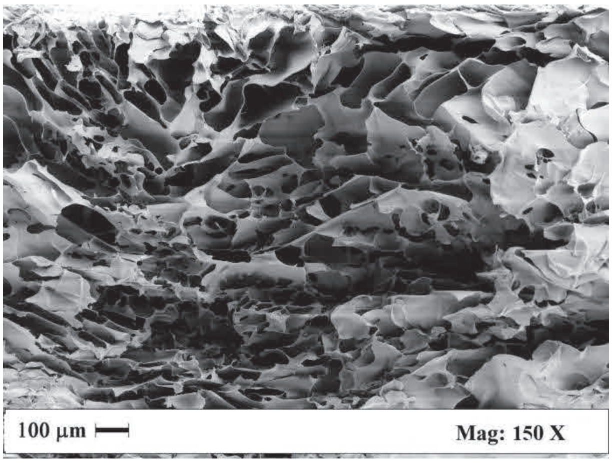

b

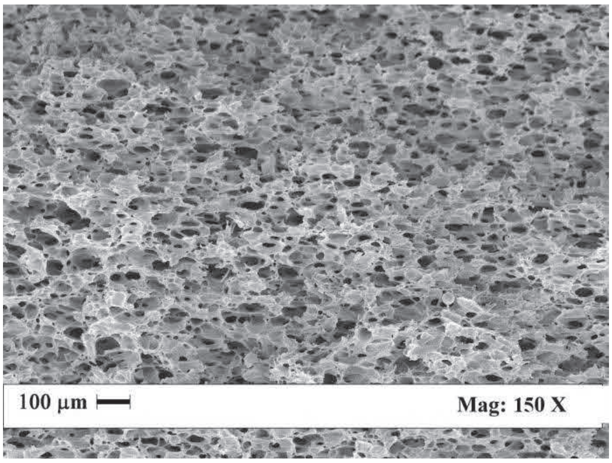

c

Figure V.47 *Effect of chitosan concentration on scaffolds morphology obtained starting from water:acetic acid ratio 97:3: (a) 2% w/w, (b) 5% w/w, (c) 10% w/w*

The pores interconnection was also analyzed using the techniques described in Chapter IV: for 2% w/w chitosan samples, a complete interconnection was found (i.e., 100%); whereas, for 5 and 10% w/w chitosan samples, pores interconnection higher that 90% was measured. The information qualitatively shown in Figures V.47b and c, where FESEM images taken at the same enlargement are reported, is quantitatively shown in Figure V.48, where pore size distributions are reported.

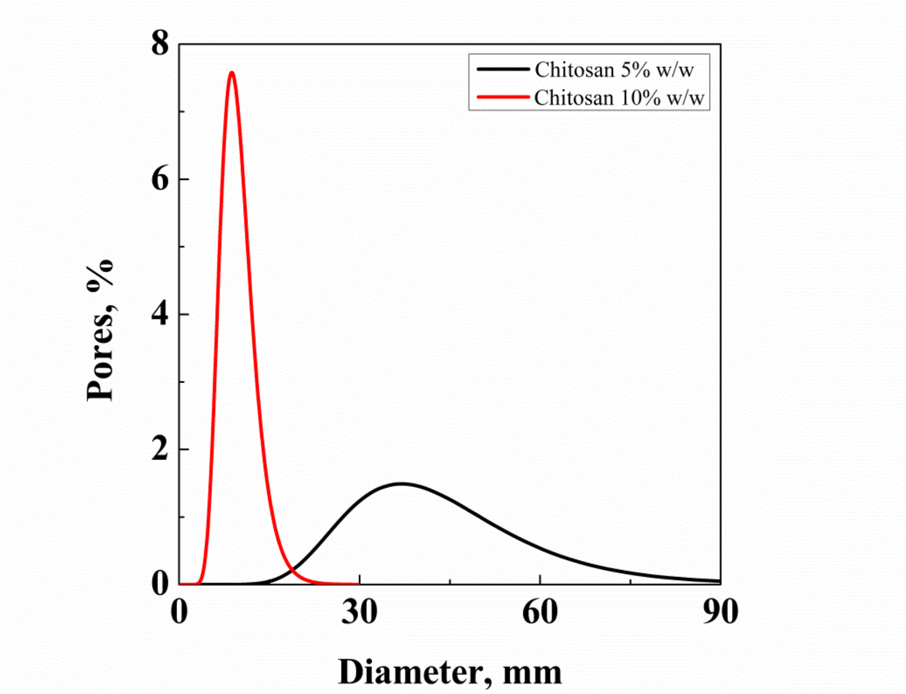

Figure V.48 *Pore size distribution of chitosan scaffolds obtained starting from 5 and 10% w/w chitosan solutions with a water:acetic acid ratio of 97:3*

Increasing from 5 to 10% w/w the polymer concentration, the mean pore size decreases from about 45 to 17 µm and pore size distribution largely shrinks (standard deviations: ± 17.6 and ± 2.8 µm, respectively).

The structures indicated by FESEM analyses were confirmed by porosimetric analysis, that measured a porosity ranging between 96% (for 2% w/w chitosan scaffold) to 87% (for 10% w/w chitosan scaffold). Moreover, observing FESEM images produced at higher magnifications, like the ones reported in Figure V.49, that are referred to 10% w/w chitosan scaffolds, it is possible to note that, in addition to the micrometric structure, pore walls are also characterized by a nanofibrous substructure in which fibers of about 80 nm are present.

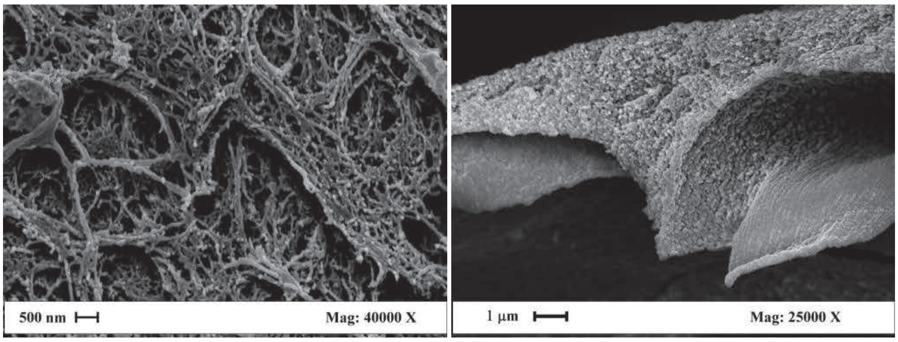

Figure V.49 *Nanofibrous sub-structure of pore walls in 10% w/w chitosan scaffolds obtained starting from solutions with water:acetic acid ratio of 97:3*

We also analyzed the scaffolds skin and verified that they were homogenously porous at all the tested operating conditions. In particular, in Figure V.50a FESEM image of the top surface of 10% w/w chitosan scaffold is reported; it is characterized by micrometric pores with a mean size of about 60 µm, that can be a suitable size for cell nutrients diffusion in and out the scaffolds.

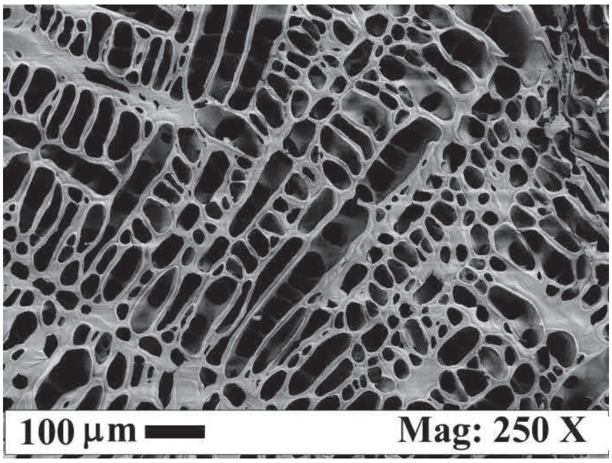

Figure V.50 *Top surface of 10% w/w chitosan scaffolds obtained starting from solutions with water:acetic acid ratio of 97:3*

This is an important result because TIPS coupled with freeze drying usually leads to surface collapse and dense skin formation, causing problems in cells colonization of the scaffold.

We also focused our attention on the size and shape of the generated structures. We measured the size and the shape of the samples after TIPS, after the substitution step (water-acetone) and after supercritical drying and verified that the structure was not subject to modification. Cylindrical scaffolds of 4 mm thickness and 2 cm diameter were typically processed in this work and their size and shape were preserved. Larger structures can be also obtained using this process, the only limitation are the dimensions of the high pressure vessel; for example, cylindrical scaffolds of 2 cm thickness and 2 cm diameter were generated in other experiments (Cardea *et al.*, 2014a).

Solvents residue analyses were also performed, as described in Chapter IV. Acetone residue in the scaffolds was found to be lower than 5 ppm; USP 467 pharmacopeia indicates a limit of 5000 ppm for acetone in structures useful for pharmaceutical applications. We also performed analyses on the acetic acid residues; indeed, the presence of acetic acid in the final scaffold could result in an undesired and uncontrolled solubilization of the scaffold once in contact with water. Also in this case, the residue was found to be lower than 5 ppm. This result was expected; the acetic acid/water solution was substituted with acetone. Moreover, SC-CO_2 presents a good affinity with acetic acid; therefore, even if traces of acetic acid were still present after the substitution step, supercritical drying contributed to their elimination.

Subsequently, the effect of acetic acid percentages on chitosan scaffolds morphology was studied. Observing 10% w/w chitosan scaffolds obtained starting from acetic acid percentages ranging between 1 and 5% v/v, we verified that their morphology was always cellular. But, increasing the acetic acid content, pore size largely decreased and the structure became more uniform. This result is clear from the comparison between FESEM images, taken at the same enlargement, shown in Figure V.47c (water:acetic acid ratio 97:3) and in Figures V.51a and b (water:acetic acid ratio 99:1 and 95:5).

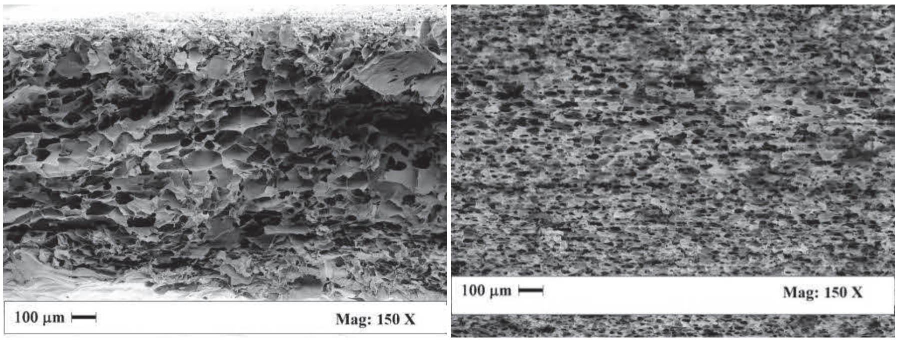

a b

Figure V.51 *Effect of acetic acid concentration on chitosan scaffolds obtained starting from 10% w/w chitosan solutions; water:acetic acid ratio of (a) 99:1 and (b) 95:5*

The corresponding pore size distributions were reported in Figure V.52.

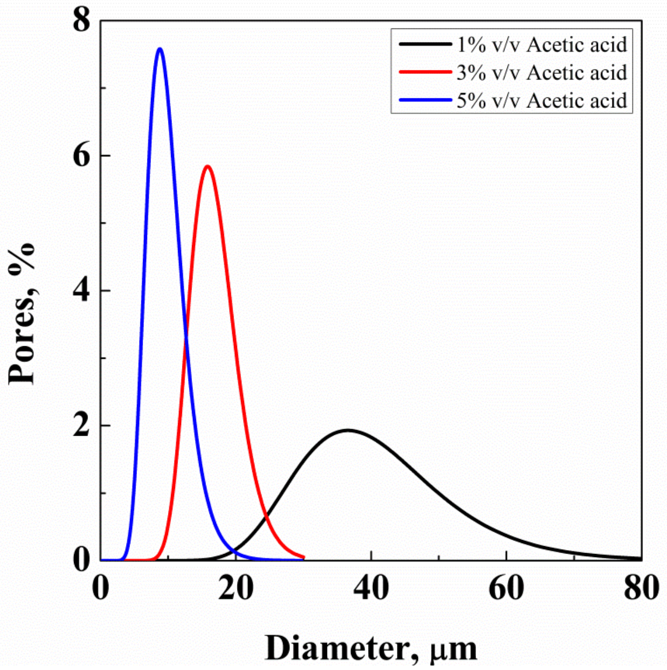

Figure V.52 *Pore size distribution of chitosan scaffolds obtained starting from 10% w/w chitosan solutions with different water:acetic acid ratio (99:1, 97:3, 95:5)*

Increasing from 1 to 5% v/v the concentration of acetic acid, the mean pore size decreases from about 40 to 10 µm and pore size distribution largely shrinks (standard deviation: ± 11.4 and ± 3 µm, respectively).

The results obtained in this work can be explained applying the classical theory of the phase separation processes. The structures generated suggest that a liquid-liquid phase separation occurred during TIPS (van de Witte *et al.*, 1996b). Moreover, the presence of a nanofibrous sub-structure is usually related to a solid-liquid demixing mechanism; therefore, an overlap of a solid-liquid demixing with the liquid-liquid demixing can be hypothesized during TIPS of chitosan solutions. To better understand this mechanism, it is possible to consider a qualitative binary diagram, in which both liquid-liquid demixing gap and gelation or crystallization curve (responsible of solid-liquid demixing) are present. In Figure V.53, a hypothetic binary diagram “polymer concentration vs. temperature” has been reported. The diagram is characterized by a homogenous region and two demixing regions: the solid-liquid demixing, bordered by the crystallization/gelation/solidification curve, and the liquid-liquid demixing, bordered by the binodal curve (the external one) and the spinodal curve (located inside the binodal).

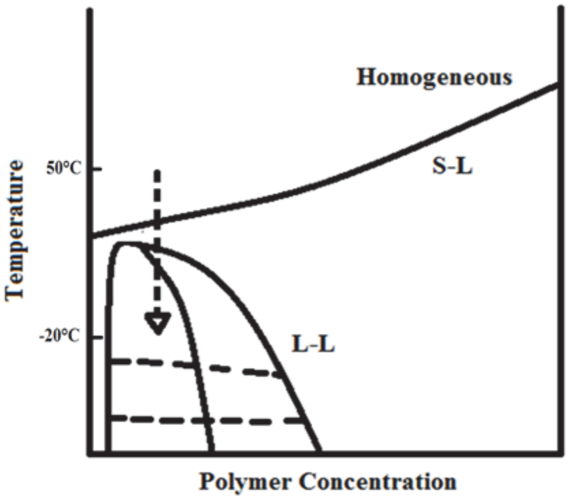

Figure V.53 *Qualitative binary phase diagram "polymer concentration vs. temperature" for the system chitosan/acid water*

The fact that all the samples contain also the nanofibrous substructure suggests that solid-liquid demixing also occurred, overlapping the liquid-liquid demixing; i.e., the gelation (or crystallization/solidification) curve is near to the liquid-liquid demixing gap; as a consequence, the "solution pathway", driven by temperature decrease from 50 °C (solution starting temperature) to -20 °C (phase separation temperature), crosses both curves during the process. In correspondence of the larger polymer concentrations in the starting solution (5 and 10% w/w), cellular structures are produced; this fact suggests that a binodal decomposition occurred. Obviously, the decrease of the polymer concentration causes an increase of pores size and a larger porosity (Reverchon *et al.*, 2004). For the bicontinuous structure obtained in correspondence of a concentration equal to 2% w/w of chitosan, a spinodal decomposition can be hypothesized.

The effect of acetic acid content on scaffolds morphology can be related to the increase of the acidity of the starting solution; consequently, the solubility of chitosan increases. It means that, from a thermodynamic point of view, the liquid-liquid miscibility gap, reported in Figure V.53, shrinks. In this way, starting from the same chitosan concentration (for example, 10% w/w) and operating with the same phase separation temperature (-20 °C), the demixing point will be located nearest to the polymer-rich phase curve, causing the formation of smaller pores. A qualitative explanation of this result is reported in Figure V.54: increasing acetic acid concentration, the miscibility gap is modified from curve 1 to curve 2 and the demixing point C, once fixed the starting point B and the demixing temperature T_c, falls nearest the polymer rich curve in the case of curve 2; i.e., smaller pores are generated.

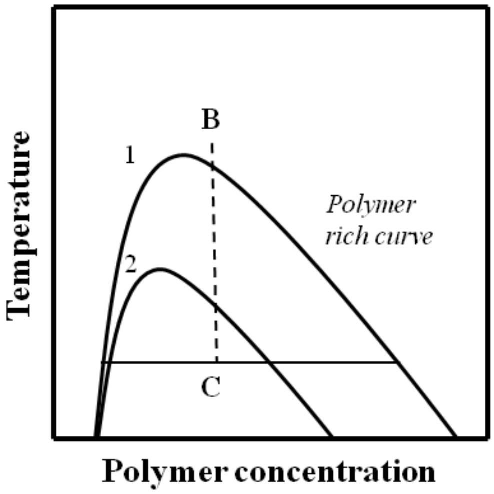

Figure V.54 *Qualitative modification of binary phase diagram changing acetic acid concentration*

In the last part of this work, some preliminary cultivation tests were performed on hMSCs. FESEM image reported in Figure V.47c shows the presence of a regular pore structure for 10% w/w chitosan scaffolds. Moreover, it is possible to observe that the structure is completely uniform and characterized by a nanofibrous substructure (Figure V.48) that should ensure the roughness which promotes the cellular adhesion, growth, migration and differentiation. For this reason, the sample shown in Figures V.47 and 48, representing the scaffold obtained from 10% w/w chitosan solution with 97:3 water:acetic acid ratio, was chosen to be tested for viability of cell culture. To demonstrate the effectiveness of the cellular culture on this kind of scaffolds, some samples seeded with hMSCs were cultured for 4 days in a static culture. In Figure V.55 live/dead assay images, taken on day 2 and day 4, are reported.

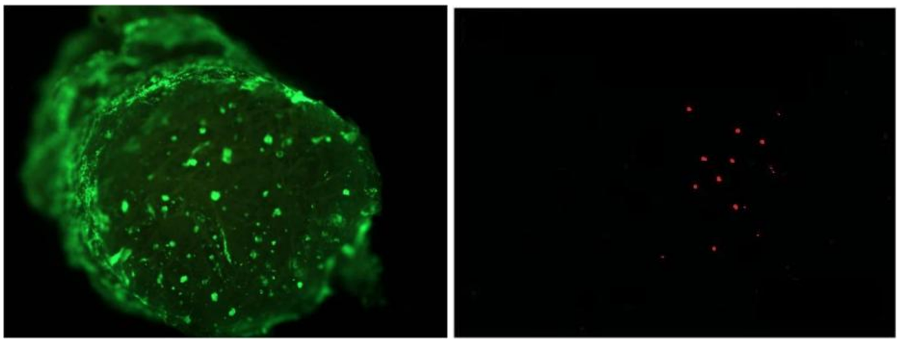
a c

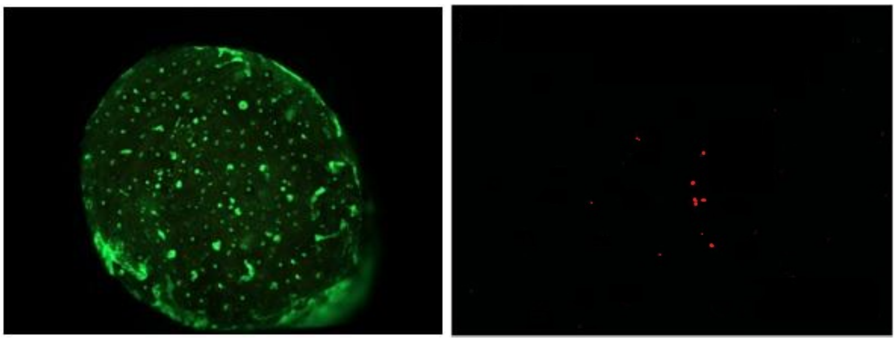

b d

Figure V.55 *hMSCs cultured for 2 (a) and 4 (b) days in osteogenic media. Live cells (stained green) and dead cells (stained red) on scaffolds obtained starting from 10% w/w of chitosan with 3% v/v of acetic acid*

Visible cell colonies were distributed on all the scaffold surface and into the scaffold itself. In particular, Figure V.55a shows hMSCs cultured for 2 days. Live cells were stained green and appeared to be well-distributed; dead cells were stained red and were very few (Figure V.55c). The percentage of live cells at day 2 calculated for chitosan scaffold was 86.5 (± 2.5)%. Figure V.55b shows cell proliferation at day 4. Live cells adhered with homogenous distribution on the scaffold surface and section and their number sensibly increased: there were few dead cells on the whole sample (Figure V.55d). Indeed, the percentage of live cells increased to 92.4 (± 1.4)% for the tested chitosan scaffolds.

V.5.3 Conclusions

We demonstrated that using TIPS followed by SC-CO_2 drying, it is possible to produce chitosan scaffolds characterized by a micrometric cellular structure, nanofibrous sub-structure and porous surfaces. In particular, two different morphologies were generated: a bicontinuos structure for 2% w/w chitosan samples in water + acetic acid and a cellular structure for 5 and 10% w/w chitosan; moreover, it is possible to control pore size changing chitosan concentration in the starting solution.

The low process temperature allows to obtain 3-D solids, whose structure is preserved during supercritical drying. Moreover, no residual solvents (acetone and acetic acid) are present after the process.

Preliminary results on cell cultivation confirm that the produced chitosan scaffolds are characterized by a morphology that is potentially suitable for TE applications. This result can depend on the micrometric morphology of the scaffolds that assures a good nutrient diffusion and on the nanometric sub-structure that allows an adequate cells adhesion.

V.6 Complete Glutaraldehyde elimination during Chitosan hydrogel drying by SC-CO_2 processing

In this work, we propose, for the first time, SC-CO_2 gel drying of chitosano (CH) scaffolds with the simultaneous elimination of unreacted Glutaraldehyde (GTA), taking advantage of its solubility in SC-mixtures. Operating in this manner, we can obtain improved CH scaffolds for TE applications that maintain the original nanofibrous structure of the gel, and do not contain residues of the highly cytotoxic GTA used for the crosslinking that, otherwise, does not allow the proliferation of cells in the scaffold. CH-GTA aerogels will be characterized from a macroscopic and microscopic point of view and a study of the release of GTA residues will be performed.

V.6.1 Preparation of Chitosan aerogel

Two kinds of CH (Low M_W and Medium M_W) were used, starting from two different CH concentrations (2 and 5% w/w) in acid water (water to acetic acid ratio 95:5). The best preparation of CH hydrogel was the following: Chitosan Medium M_W (0.40 g) was dissolved in 20 mL of water/acetic acid solution (pH 2.43) to obtain a CH concentration of 2% w/w. NaOH (1 M in water, pH 14) was slowly added to this solution and the changes in pH were registered, each added mL, by a pH-meter. At the same time, the gel formation was monitored until the maximum gel point was reached at pH 12.5. The gel sample was, then, repeatedly washed with distilled water, to remove the excess of NaOH solution. CH hydrogels were crosslinked using a GTA solution 0.25% w/w in water. The crosslinking solution was obtained by diluting 1 mL of GTA (25% w/w) in 99 mL of water. Different ratios CH gel/GTA were used (see Table V.4), to identify the best operating conditions: CH:GTA 32:1, 16:1, 8:1, 4:1 and 1:1; GTA content was increased to the maximum ratio (1:1) to verify the efficacy of the SC-CO_2 purification process on crosslinked CH aerogel.

Table V.4 *CH and GTA amounts used for the crosslinking reaction*

CH:GTA	*32:1*	*16:1*	*8:1*	*4:1*	*1:1*
CH hydrogel, mL	10	3	3	3	3
GTA 0.25% w/w, mL	0.3	0.2	0.4	0.75	3

The crosslinking reaction was performed at room temperature, adding GTA solution to CH gel, under Vortex shaking for 1 min. The system was left for three days in quiet. The crosslinked sample was, then, repeatedly washed with distilled water. SC-CO_2 drying cannot be directly applied in the case of hydrogels, since SC-CO_2 shows a very reduced affinity with water (Diamond *et al.*, 2003). Therefore, before drying, the samples were immersed in an ethanol bath for 24 h at room temperature, to allow the complete replacement of water with ethanol, inside the samples.

The obtained alcogels were SC-CO_2 dried at the following operating conditions: 35 °C, 200 bar, for 8 h.

V.6.2 Crosslinked Chitosan aerogel: results and discussion

In the first part of the study, some experiments were performed to optimize the CH hydrogel in water. We found that at the end of the drying process, the samples maintained the same shape and volume, that is the first evidence that the delicate nanofibrous architecture of CH gels was not destroyed. This evidence was confirmed by FESEM images (Figure V.56a-d), in which both CH aerogel (Figure V.56a) and crosslinked CH aerogel (Figure V.56b-d) showed the same nanofibrous morphology. The nanofibers are very regular and uniformly distributed along the samples section and have an average size of about 100 nm. The only difference in Figure V.56 images is the different arrangement of the nanofibers that could depend on the quantity of GTA used for crosslinking.

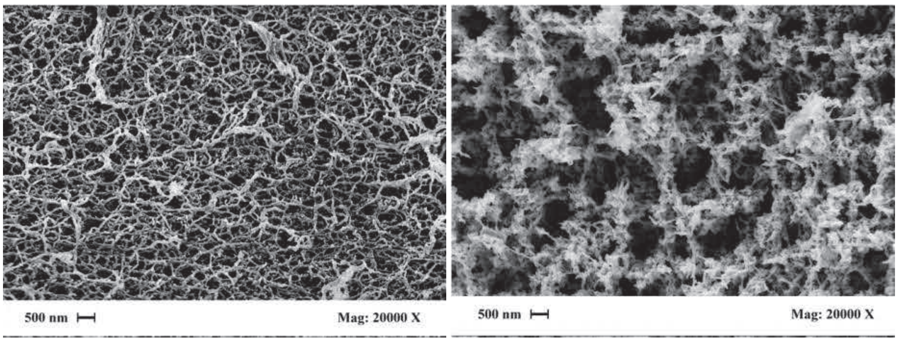

a b

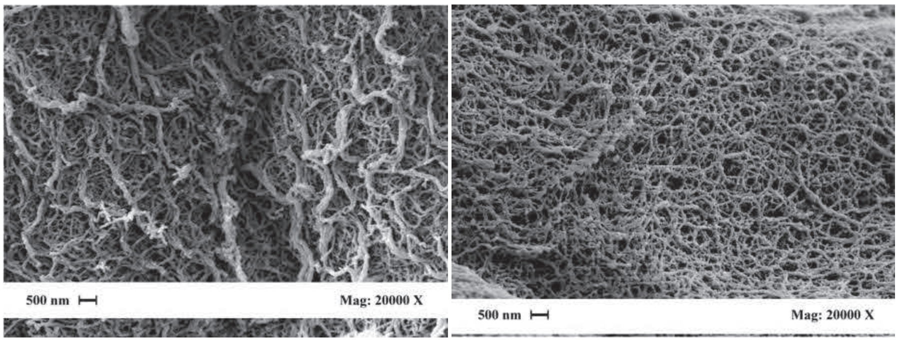

c d

Figure V.56 *FESEM images of Chitosan medium M_w (2% w/w): (a) CH aerogel section; (b) CH:GTA 16:1 aerogel section; (c) CH:GTA 8:1 aerogel section; (d) CH:GTA 4:1 aerogel section*

Also the samples surface maintained the uniform and nanofibrous morphology, as shown, for example, in Figure V.57, where is reported a FESEM image of the surface of a CH:GTA 4:1 aerogel. On the contrary, aerogels produced by freeze-drying show closed surfaces, due to the force exerted by the surface tension during the solvent extraction from the polymeric matrix, that causes the polymer collapse.

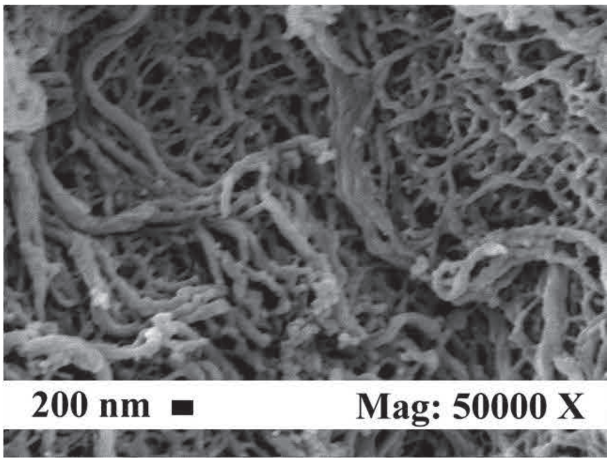

Figure V.57 *FESEM image of CH:GTA 4:1 aerogel surface*

This result is important to favor the interaction of cells with the aerogel, since open skins are required for the cell inoculation, adhesion and proliferation; i.e., this morphology improves the efficiency of the cells culture. Summarazing, nanostructured gel morphology was preserved in all cases and it is similar to that of the ECM proteins of the native tissues, that show an average fibers diameter between 50-500 nm; i.e., 1 to 2 orders of magnitude smaller than the living cells. This characteristic allows the cells to be in direct contact with many ECM fibers, thereby defining their three dimensional orientation (Barnes *et al.*, 2007).

V.6.2.1 Glutaraldehyde release from Chitosan aerogel

The second problem in CH hydrogel drying is the entrapment inside the structure of unreacted GTA. It can be reduced by washing several times the samples with ethanol to extract at least part of the GTA and using calibrated quantities of GTA to induce crosslinking, reducing at a minimum the unreacted material. However, since GTA is a powerful sterilizing agent, the possibility to extract its residues during the drying process can largely improve the final product in view of its application for cells cultivation. Indeed, GTA is a small molecule and though its solubility in SC-CO_2, at the best of our knowledge, is not known, it could be slightly soluble in SC-CO_2. Moreover, during SC-drying, CO_2 extracts ethanol contained in the alcogel, forming a SC-mixture ethanol-CO_2. This mixture shows more affinity with GTA than SC-CO_2 alone, due to the presence of ethanol in which GTA is largely soluble. The gas-like diffusivity of the ethanol-CO_2 SC-mixture can allow it to extract entrapped GTA more efficiently than liquid ethanol. To verify experimentally this hypothesis, a series of GTA release experiments was performed.

In a typical experiment, 15 mL of CH hydrogel were immersed in 3 mL of PBS buffer (pH 7.4) and glycine 0.1 M (PBS:Gly = 0.43) and GTA absorbance was measured at 234 nm, using a UV-Vis spectrophotometer at room temperature (Bigi *et al.*, 2001). The released GTA curves are reported in Figure V.58; GTA concentration was measured using a calibration curve obtained using know quantities of GTA. Final concentration values, in terms of ppm, are reported in Table V.5.

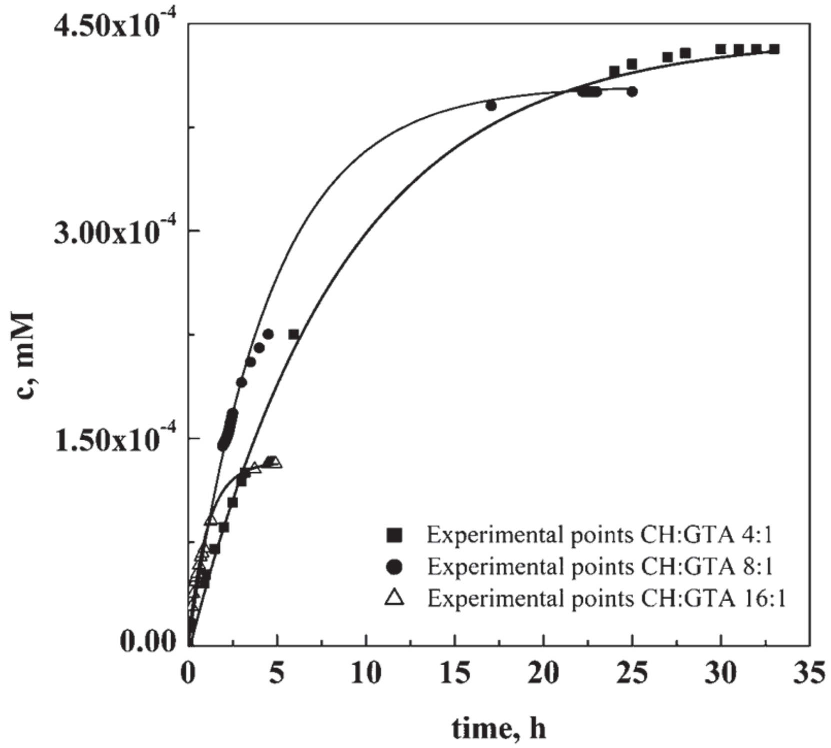

Figure V.58 *GTA release from CH aerogels 2% w/w*

Table V.5 *Maximum GTA concentration measured in the release medium*

Aerogel	*GTA concentration, ppm*
CH:GTA 1:1	77.7
CH:GTA 4:1	$4.32 \cdot 10^{-2}$
CH:GTA 8:1	$4.01 \cdot 10^{-2}$
CH:GTA 16:1	$1.32 \cdot 10^{-2}$

The sample CH:GTA 1:1, in which the quantity of GTA used for crosslinking is in a large excess, is not reported in Figure V.58. In all the other cases, the obtained asymptotic curves were fitted using an exponential equation. The released quantities, converted in ppm (Table V.5), show maximum values of about 0.04 ppm for the CH:GTA ratios 4:1 and 8:1 and of about 0.01 ppm for CH:GTA ratio 16:1. This amount is negligible when compared to 3 ppm reported in the literature as the GTA residue that blocks, almost completely, cells reproduction (Speer *et al.*, 1980). These materials can be readily used for TE applications.

V.6.2.2 FTIR analysis

IR spectroscopy was used to verify the structural modifications introduced by GTA on CH during the crosslinking reaction. Figure V.59 shows FTIR spectra obtained with ATR method on samples of CH 2% w/w. In particular, the following sample curves are reported: pure CH (reference), CH:GTA 16:1, 8:1, 4:1 and 1:1. The last sample (1:1) contained a large GTA excess and was used only to verify the efficiency of the SC-CO_2 based purification process on crosslinked aerogels.

FTIR spectrum of CH (Figure V.59, first curve from the top) shows the typical band at 3360 cm^{-1} of OH and NH_2 stretching. The peak at 2874 cm^{-1} belongs to stretching vibration of CH groups. In all the spectra, two peaks are visible at 1650 cm^{-1} and 1640 cm^{-1}, which can be attributed to C=O stretching and NH bending of amide groups (note that CH we used had a deacetylation degree of 80%). The peak at 1376 cm^{-1} can be assigned to methyl groups of the polymer and the one at 1420 cm^{-1} to the bending of O–H and C–H groups.

From the 16:1 to the 1:1 CH:GTA curve, a peak at 1590 cm^{-1}, belonging to the imine C=N bond, formed between the amine residues of CH and the aldehyde terminals of the GTA, is well detectable. At the same time, only in the CH:GTA 1:1 curve, a small peak at 1750 cm^{-1}, typical of C=O carbonyl group is slightly visible. This indicates a non negligible presence of GTA in the sample 1:1. The large peaks at around 1070 e 1024 cm^{-1} correspond to the CO bending vibration, typical of CH saccharidic structure.

Therefore, FTIR analysis shows that the cross-linking process of CH with GTA has been successfully obtained, as is demonstrated by the presence of the well detectable peak at 1590 cm^{-1} in all curves of cross-linked samples (imine C=N bond) and that the GTA has been removed from the hydrogels, except for the 1:1 sample, in which the carbonyl peak at 1750 cm^{-1} (belonging to free GTA) is non negligible. This result was, however, expected, since in this sample the excess of GTA was increased over a reasonably necessary amount, to set an upper limit to the use of GTA.

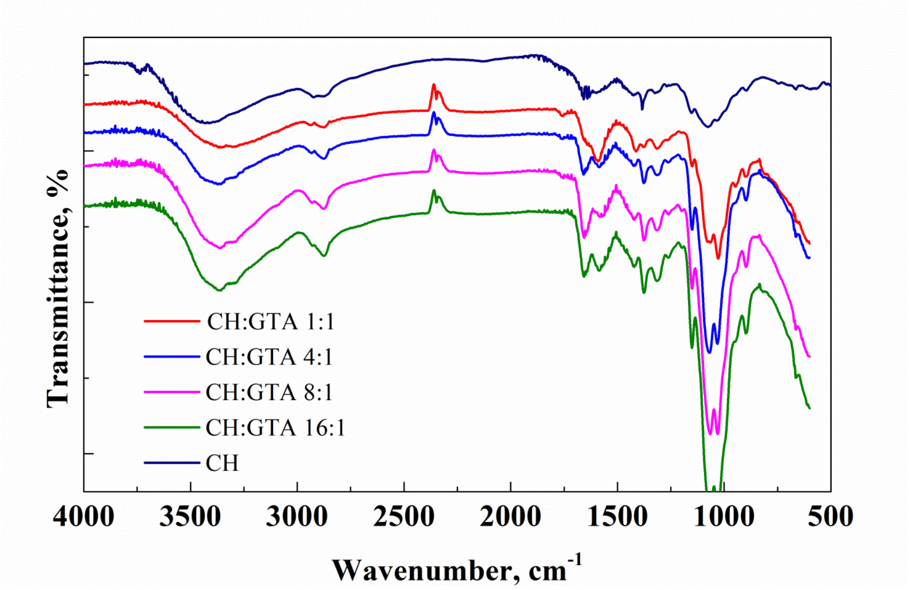

Figure V.59 *FTIR spectra of pure CH and CH aerogels, 2% w/w crosslinked with GTA*

V.6.2.3 TGA analysis

In Figure V.60 and in Table V.6, thermogravimetric curves and decomposition temperatures (T_d) of CH aerogles are reported. Compared to decomposition temperature of the CH aerogel (218 °C), the crosslinked CH samples show a higher T_d, ranging from 247 to 251 °C, and increasing with the increase of crosslinking agent used (from CH:GTA 16:1 to CH:GTA 1:1). This data is consistent with the fact that the crosslinking reaction leads to a more thermally stable structure, and to a consequent increased degradation temperature of the CH aerogel samples.

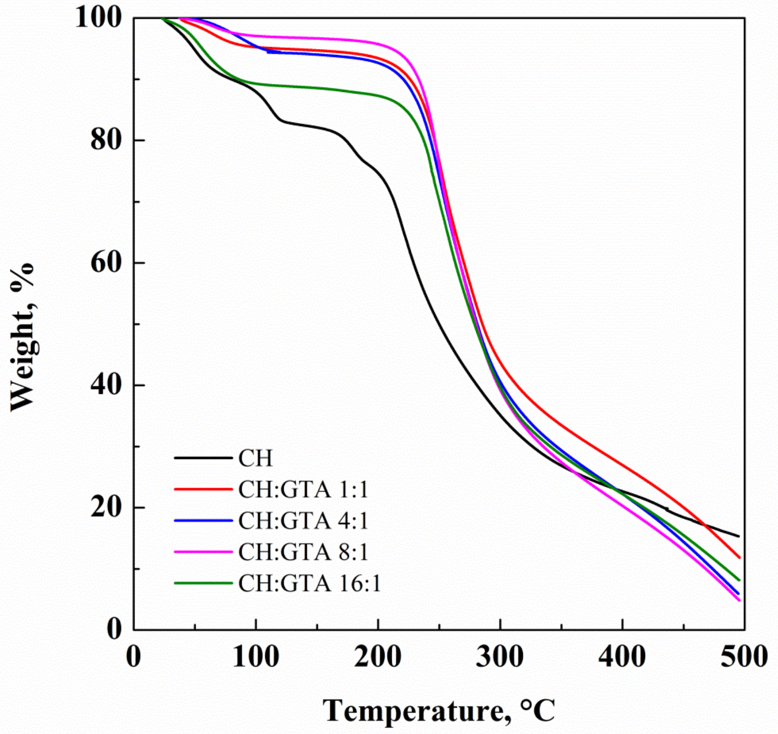

Figure V.60 *Thermogravimetric analysis of CH aerogel samples*

Table V.6 *Degradation temperature of CH aerogels crosslinked with GTA*

Aerogel	***T_d^*, °C***
CH	218
CH:GTA 16:1	247
CH:GTA 8:1	248
CH:GTA 4:1	249
CH:GTA 1:1	251

$^*T_d$ = Degradation temperature, corresponding to the maximum weight loss of the sample.

V.6.3 Conclusions

The results on crosslinking, SC-CO_2 drying and GTA residues measurements, confirm that CH hydrogels crosslinked with GTA were successfully dried, preserving their nanostructure: no collapse of the nanostructure was observed in the aerogels surface and section. The hypothesis that SC-(CO_2 + ethanol) mixture is able to efficiently extract GTA residues entrapped in the gel matrix was verified and negligible residues of GTA were found during release experiments.

Therefore, the produced CH aerogels not only maintained their delicate nanostructure necessary for the cells cultivation, but can also be safely used for TE applications.

V.7 FEM Modeling of the reinforcement mechanism of HA in PLLA scaffolds

The aim of the present work is the development of a parametric FEM, governed by algorithms based on our experimental evidences, to critically analyze the mechanical characteristics of PLLA scaffolds loaded with HA nanoparticles, obtained by supercritical gel drying, in consideration of the fact that they show promising regenerative interactions in presence of hMSCs (Pisanti *et al.*, 2012).

V.7.1 Preparation of the composite scaffolds

Scaffolds were prepared according to the procedure reported in a previous work (Reverchon *et al.*, 2009). Solutions with PLLA at concentrations of 15% w/w in dioxane were prepared; then, ethanol, as the non-solvent, was added, obtaining a dioxane/ethanol ratio of 1.7. The solution was stirred and heated at 60 °C until it became homogeneous. Then, fructose microparticles were added with a mean diameter of 250 μm, together with HA nanoparticles (diameter < 200 nm), forming a gel suspension. This gel was dried using SC-CO_2 at 200 bar, 35 °C for 4 h (Reverchon *et al.*, 2009); the obtained structures were poured in distilled water for 24 h to eliminate fructose particles. Subsequently, the scaffolds were put in an oven for 4 h at 40 °C, to evaporate water.

V.7.2 Experimental results

In the first part of the work, we reproduced and extended the results obtained in a previous work (Reverchon *et al.*, 2009). In particular, we focused the attention on the influence of HA nanoparticles loading in PLLA, on the morphology and mechanical resistance of the scaffolds generated by supercritical gel drying. Various HA percentages were tested.

V.7.2.1 Effect of HA nanoparticles percentage

Supercritical drying experiments were performed at 200 bar and 35 °C, partly replicating the ones obtained in a previous work (Reverchon *et al.*, 2009), to verify the process reproducibility. PLLA concentration was maintained constant at 15% w/w in the liquid solvent formed by dioxane and ethanol (see Preparation of the composite scaffolds). HA content was varied from 10 to 50% w/w of PLLA. In Figure V.61, FESEM images of the new produced PLLA scaffolds have been reported. They are all characterized by the presence of the microporous structure due to the presence of porogen particles (Figures V.61a, V.61c) and by an uniform nanometric network related to the gel structure (Figures V.61b, V.61d). Part of HA nanoparticles tends to adhere on PLLA fibers, probably, as a result of electrostatic forces acting among nanoparticles and polymer (see Figure V.62b).

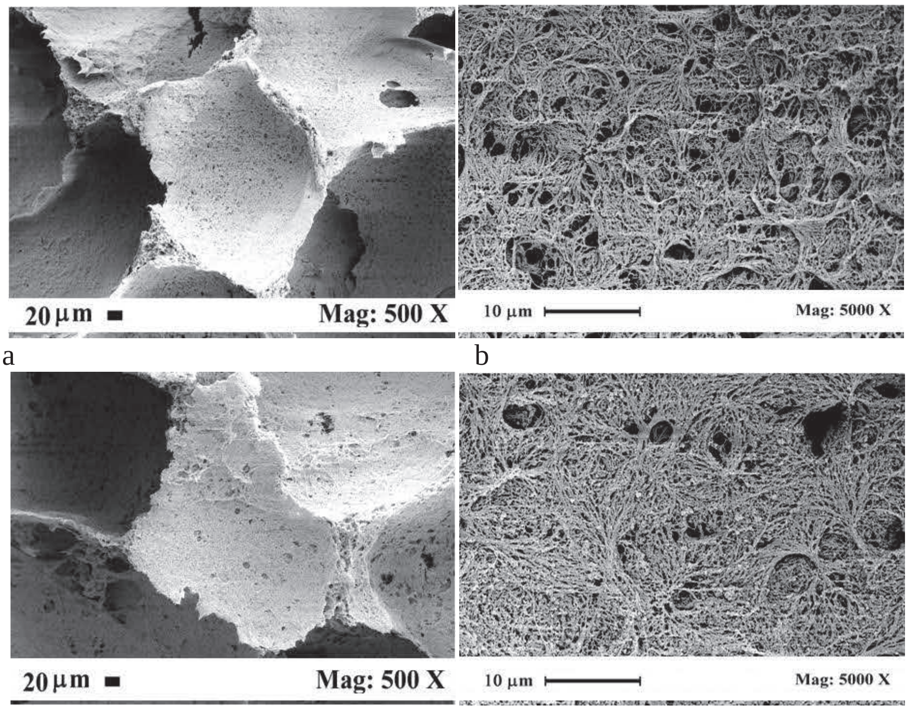

a b

c d

Figure V.61 *PLLA/HA scaffolds obtained by SC-CO_2 drying at 200 bar and 35 °C, with a-b) 10% w/w HA, c-d) 50% w/w HA*

At high HA loadings, HA nanoparticles tend also to deposit at the bottom of the pores of the polymeric structure. These experimental evidences are well described in Figure V.62. In Figure V.62a, PLLA nanofibers related to a scaffold not loaded with HA are shown, that, when compared with HA decorated nanofibers in Figure V.62b, clearly show the difference between the two nanostructures. HA decoration in multiple layers is clearly visible. In Figure V.62c, instead, a FESEM image of HA nanoparticles found on the bottom of a micropore is reported.

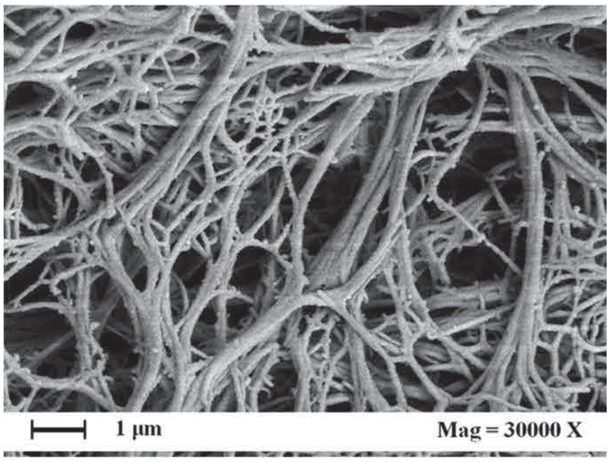

a

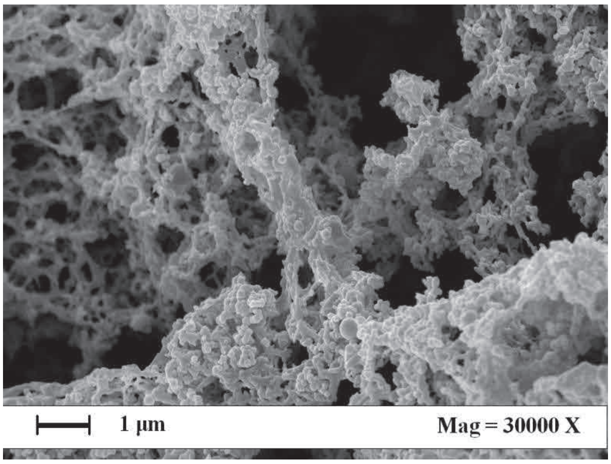

b

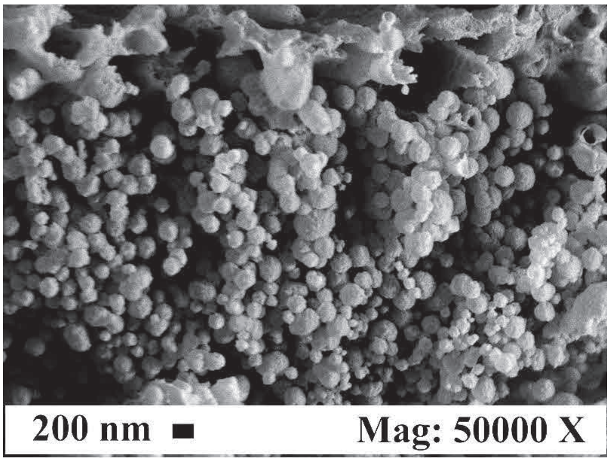

c

Figure V.62 *PLLA scaffolds obtained by SC-CO_2 drying at 200 bar and 35 °C, a) 15% w/w PLLA, b) 15% w/w PLLA + 50% w/w HA, c) HA nanoparticles on the bottom of a PLLA micropore, 50% w/w HA*

In the scaffolds with HA contents equal or lower than 30% w/w no accumulation of nanoparticles is evidenced on the bottom of micropores. It is also relevant that the presence of HA nanoparticles does not modify the microporous and the macroporous structure; i.e., dimension and shape of the pores and of the scaffolds.

Another possible problem, is the possibility of nanoparticles to agglomerate. For this reason, we verified the overall HA nanoparticles distribution inside the scaffold structure. In Figure V.63, we report an EDX analysis of HA nanoparticles distribution along the scaffold. It confirms that a relatively uniform distribution has been obtained for a 30% w/w loading of HA.

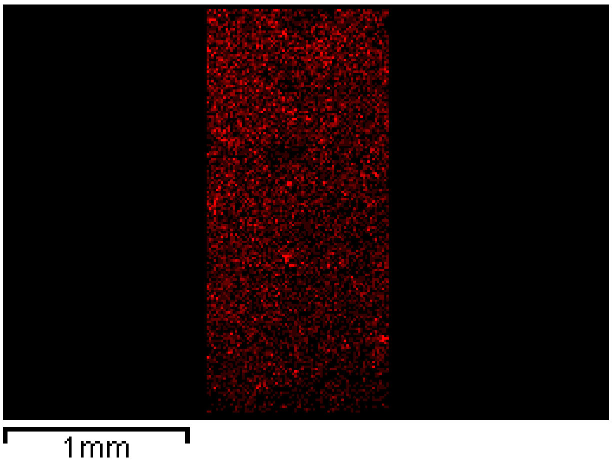

Figure V.63 *HA nanoparticles distribution (measured through the Calcium atoms distribution - red) along the section of a PLLA scaffold with 30% w/w of HA*

Once verified the morphology of the scaffolds and the distribution of HA nanoparticles, we focused the attention on the mechanical characteristics of PLLA + HA scaffolds. We analyzed the compressive modulus of PLLA scaffolds starting from pure PLLA and, then, analyzing those with increasing percentages of HA nanoparticles. These results are reported in Table V.7. The loading of HA nanoparticles inside the structure produces a sensible increase of the compressive modulus from 81 to 122 kPa, thus overcoming the compressive modulus that is usually set as the optimum for bone temporary scaffolds (100 kPa). These results are similar to those obtained in a previous work (Reverchon *et al.*, 2009), confirming the good reproducibility of the process.

Table V.7 *Compressive modulus of PLLA scaffolds obtained with different HA contents*

PLLA, % w/w	***HA, % w/w PLLA***	***Compressive Modulus, kPa***
15	0	81 ± 1.5
15	10	107 ± 1.8
15	30	120 ± 2.0
15	50	122 ± 2.5

A first explanation of these results can be hypothesized considering that the presence of uniformly distributed HA nanoparticles inside the nanofibrous structure of the scaffold reinforces the overall structure producing a higher mechanical resistance. However, as we will see in the modeling section, more intriguing scenarios are possible. In principle, it could be possible to find a compromise between the nanofibrous structure of non-loaded PLLA scaffolds, the fibrous + nanoparticle structure of PLLA + HA scaffolds and the obtained mechanical resistance. The better compromise seems to be represented by PLLA scaffold containing 30% w/w of HA, considering that the loading of 50% w/w of HA nanoparticles produces a negligible increase of the compressive modulus. Moreover, cultivation of hMSCs in the same PLLA + HA scaffolds with different porogen diameters and 30% w/w HA nanoparticles loading was performed in a previous work (Pisanti *et al.*, 2012) using a tubular perfusion bioreactor. The scaffolds loaded with 250 µm porogen were the most appropriate for hMSCs migration, proliferation and differentiation. Effects of the architecture of the scaffold were magnified in dynamic culture, leading to increased proliferation and osteoblastic differentiation evidenced by ALP and bone morphogenic protein-2 (BMP-2) expression (Pisanti *et al.*, 2012).

V.7.3 FEM modeling and results

In this part of the work, we focused our attention on the realization of parametric FEM models, that can give a proper representation of the experimental evidences. PLLA scaffolds generated in this work are characterized by two kinds of porosity: at micrometric and at nanometric level.

Therefore, FEM models must be able to:

- simulate the nanometric and micrometric porosity;
- allow the realization of a sensitivity analysis, aimed at finding parameters on which to focus the modeling and to verify the hypothesized mechanisms of reinforcement, in the context of linear elasticity;
- successful reproduce experimental results.

The results we obtained in this work, come from the appropriate interaction of two FEM models managed as will be explained in detail in the following paragraphs: a FEM model representing the micrometric porosity and a FEM model representing the nanoscale porosity.

V.7.3.1 Modeling micrometric porous structure

The porogen, as discussed in the experimental section, consists of fructose particles with a mean diameters of 250 µm, that can be modeled as spheres with a good degree of approximation. It formed a suspension in the polymeric solution that is, then, compressed at 10 bar to produce a contact among porogen particles inducing the interconnection among the pores of the final structure. In the hypothesis of spherical particles having all the same diameters, it is possible to approximate the structure as a “Close-packing of equal spheres”; i.e., a dense arrangement of congruent spheres in an infinite, regular arrangement. The greatest fraction of space that can be occupied by spheres, in regular lattice arrangement, is equal to 0.74.

There are two simple regular lattices that achieve this highest average density; they are called face-centered cubic (fcc) and hexagonal close-packed (hcp) (Figure V.64). Both are based on sheets of spheres arranged at the vertices of a triangular tiling; they differ in how the sheets are stacked upon one another (Figure V.64). The direction of compression coincides with the direction of the compression mechanical testing and is the same of the axis of the cylindrical container. This fact is in favor of the adoption of the hexagonal close-packed (hcp) modeling.

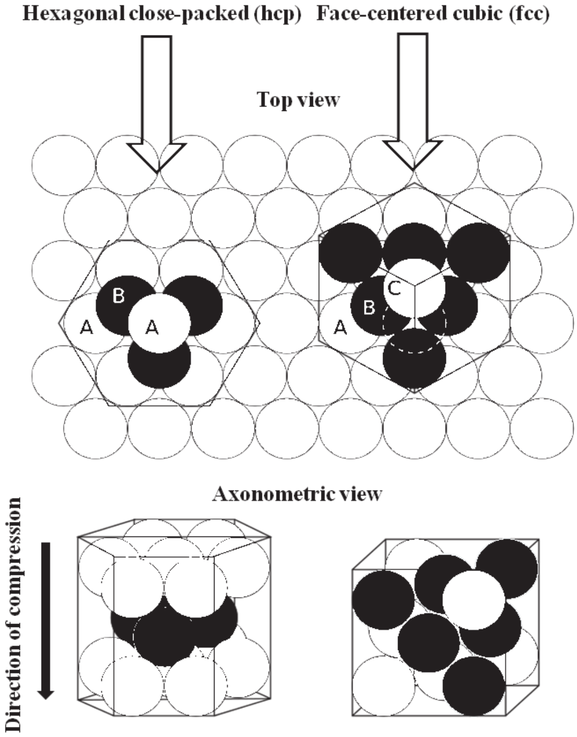

Figure V.64 *hcp (left) and fcc (right) close-packing of spheres*

Identification of the representative volume element (RVE)

In finite element modeling, RVE is the smallest volume element investigated; that is large enough to contain all the intrinsic characteristics in the real structure to be simulated (material properties and geometrical characteristics). Our choice has fallen on a porous hexagonal prism, based on the theory of hcp, according to which, there is a spherical pore arrangement of ABA type. A layer is composed by 7 spherical pores, while the B layer by 3 spherical pores (Figure V.64 on the left).

For this purpose, in the *Ansys* FEM simulation environment, we have written an algorithm that, depending on the porosity, is able to realize the geometrical RVE model previously described, using a Newton-Raphson method to approximate the porosity (see Figure V.65). The micrometric porosity was calculated on the basis of the specific weight of the polymer and of the amount by weight of fructose particles and of the other components contained in the gel. It is equal to about 0.8. Remembering that, in hcp distribution the maximum accessible porosity is equal to about 0.74 in condition of tangency among the spheres, the algorithm used to model the desired porosity (0.8), produces some intersections among the spheres. This fact results in the formation of holes that connect the pores of the structure, as in the experimental evidence.

In the second step, the algorithm is able to realize an identical mesh on the two bases of the prism; therefore, it can apply displacement boundary conditions on counterpart nodes to simulate the compression test.

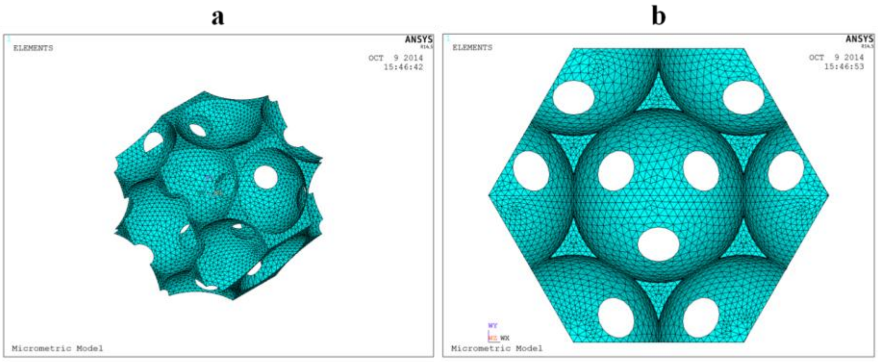

Figure V.65 *RVE FEM model (micrometric structure level): a) 3D view; b) Top view*

The use of an identical mesh, on opposite sides of the porous hexagonal prism, allows us to apply the following boundary conditions on the displacements related to homologous nodes lying on opposite sides:

$$\begin{cases} u_2 = \varepsilon_{xx} L + u_1 \\ v_2 = v_1 \\ w_2 = w_1 \end{cases} \tag{1}$$

being u, v and w the three displacement components of opposite nodes, indicated with 1 and 2 subscripts and being ε_{xx} the imposed deformation along the x axis (prism axis).

The Cauchy Tensor associated to this test presents negligible components compared to σ_{xx} component; therefore, we can easily calculate the homogenized Young's modulus, using the following relationship:

$$E_{xx} = \frac{\langle\sigma_{xx}\rangle}{\langle\varepsilon_{xx}\rangle} \tag{2}$$

being $\langle\varepsilon_{xx}\rangle$ the strain component applied to the RVE in the *x* direction; and

$$\langle\sigma_{xx}\rangle = \frac{\sum \sigma_{xxi} v_i}{V_p} \tag{3}$$

in which σ_{xxi} is the *x* normal component of the Cauchy Tensor and v_i the volume of the i-th finite element of the model; V_p the volume of the pore-free virtual hexagonal prismatic RVE. This algorithm can calculate $\langle\sigma_{xx}\rangle$ also as:

$$\langle\sigma_{xx}\rangle = \frac{\sum F_i}{A} \tag{4}$$

being F_i the *x* component of the reaction nodal force applied on the i-th node lying on one of the basis of the prism and *A* the surface of the hexagonal basis. These two different methods of calculation produced the same result.

Selection of a particular mesh, after a convergence analysis of the results

The part of the algorithm written to generate the mesh in *Ansys* environment (FEM routine) processes the input data on the microscopic geometry, allowing the construction of volumes and surfaces of RVE. At this point, the algorithm requires the definition of elements for the finite element discretization. We have chosen "20 nodes" solid elements well suited to model curved boundaries and "mesh-only" elements used, in this case, to drive the volume-meshing in a 3-D space (Cricrì *et al.*, 2012; Naddeo *et al.*, 2014). The convergence analysis of the results (in terms of mechanical properties) has been performed using the variation of the average size of the model mesh (defined as $M=R/i$, being R the radius of the spherical pores) starting by $i = 2$ to a value at which the percentage error of FEM model from $i = n$ to $i = n+1$ can be considered negligible for the purposes of the present work, since a stable asymptotic solution is reached. Stabilization of the result at $i = 15$ can be observed, beyond which the error assumes an oscillating low value. For this reasons, an average size of the model mesh equal to $M=R/15$ has been chosen with a corresponding percentage error of 0.085. Choosing this value as the average size for the model mesh, the obtained Young's modulus is equal to 6.88% of the Young's modulus introduced as input.

Therefore, considering E_{ex} the experimentally measured Young's modulus of PLLA gel without fillers (HA), the nanoporous structure model should behave as a continuum characterized by a Young's modulus equal to $E_n = E_{ex}/0.069$. It means that the model of the nanoporous structure characterized by an input Young's modulus equal to that of the compact and untreated PLLA (E_I) should give, as output, a value equal to E_n. This output value will be the first target for the realization of the nanoporous structure model (nanofiber network) whose development will be explained in the following chapter.

V.7.3.2 Modeling the nanofiber network

Starting from the experimental data, it is possible to calculate the nanoscale porosity through the following relation:

$$P_n = \frac{P_{tot} - P_M}{1 - P_M} \tag{5}$$

being P_n the nanoscale porosity, P_M the measured micrometric porosity and P_{tot} the experimentally measured global porosity.

Aerogel can exhibit a great structural variety, from branched to compact clusters, depending on the intrinsic or extrinsic conditions (solvent, water content, pH, catalysts, reaction time, etc.). Attempts to model the microstructure of aerogels used void expansion methods (VEM) (Schenker *et al.*, 2009), diffusion-limited aggregation (DLA) (Ma *et al.*, 2001a) and Gaussian random field methods (GRF) (Quintanilla *et al.*, 2003). At present, there is no consensus on which simulation strategy is the most adequate. For instance, it is not possible to tune the porosity of the material with standard DLA or GRF. Moreover, some authors argued that the fractal scaling produced by DLA cannot be observed experimentally. On the other hand, GRF and VEM do not seem to model the physics of gel formation adequately (Morales *et al.*, 2014). In the past, the deviation of aerogels from the prediction for foams has been attributed to the abundance of "dead-ends" (Ma *et al.*, 2002) that are clusters connected to the backbone of the aerogel network at only one point. Other authors (Ma *et al.*, 2000) used the diffusion limited cluster-cluster aggregation (DLCA) algorithm (Gilmore *et al.*, 1982) to generate 3D on-lattice aerogel models and the simulations showed that "loop" structure could be important to account for the stiffness of the aerogel (Ma *et al.*, 2001a). On the other hand, the DLCA model (obviously) contains excessive dead ends which lead to underestimation of the gel modulus at a given density.

Using the commercial image analysis software *Photoshop*, FESEM micrographs of the gel have been converted into black and white images, applying a threshold value. Then, the morphological parameters of the aerogel have been evaluated. The fibers are substantially arranged in a random network, in all the PLLA aerogel samples without apparent dead ends. No evident clusters or aggregates have been found in the fiber network.

Since a great part of the stiffness of an aerogel depends on how the fiber network is connected in the space (Ma *et al.*, 2001a), in first approximation, we imagined a space frame of cylinder-shaped fibers to simulate a structure that basically behaves like an isotropic material. We realized a space frame entirely formed by tetrahedral structures; the idea is to use a modified finite element discretization algorithm to realize the geometric space frame.

RVE identification of the nanometric level

The RVE was chosen as cubic-shaped and discretized in tetrahedra to allow an easily boundary conditioning and its dimensions were be chosen taking care of the statistical intrinsic characteristics, trying to obtain an acceptable degree of isotropy (Cricrì *et al.*, 2012). For this reason, we modified a finite element discretization algorithm of the commercial software *Ansys* to transform the tetrahedral mesh of an unit size cubic RVE into a parametric geometric space frame whose beams match the tetrahedra edges; subsequently, after deleting the tetrahedral solid mesh, it realizes the mesh of this geometric space frame using linear two-node beam elements in 3-D.

A FEM routine creates identical surface mesh between opposite edges to apply opportune displacement equations that couple homologous nodes on opposite sides depending on the imposed average strain (Cricrì *et al.*, 2012; Naddeo *et al.*, 2014) (periodic boundary conditions (Ching *et al.*, 2009)). In Figure V.66, a mesh example is presented. For graphical purposes, a reduced mesh wires are represented, than those used in the calculation.

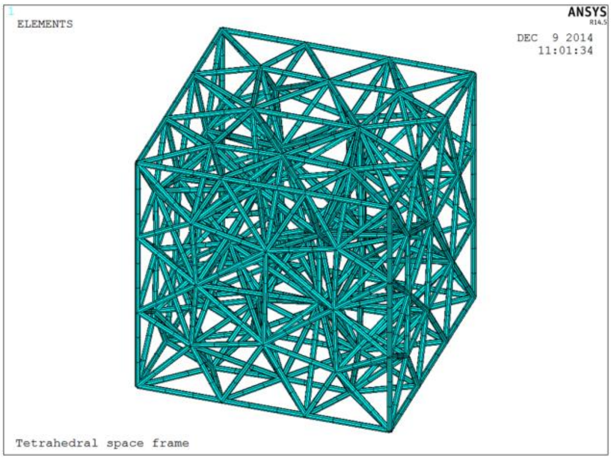

Figure V.66 *RVE showing a meshed tetrahedral space frame*

Homogenized modules

After the application of the boundary conditions, three static tensile tests and three static shear tests (with imposed average deformations) are automatically performed obtaining all the stiffness matrix components of RVE. Imposing the overall deformation $\langle \varepsilon \rangle = [0, \dots, \langle \varepsilon_i \rangle, \dots, 0]$ and assuming small strains and elastic behavior of the material, for each i-th imposed deformation, the algorithm calculates all the components of the corresponding i-th column of the stiffness matrix, using the following formulation; from the elastic overall constitutive law we can write:

$$\overline{\overline{C_{hi}}} = \frac{\langle \sigma_h \rangle}{\langle \varepsilon_i \rangle} \ \forall \ h, i = 1, \dots., 6 \tag{6}$$

in which the stress component $\langle \sigma_h \rangle$ is calculated in FEM routine, using the following relation:

$$\langle \sigma_h \rangle = \frac{\sum_{elem} \sigma_{h\,elem} vol_{elem}}{vol_{RVE}} \tag{7}$$

in which $\sigma_{h\,elem}$ is the h-th stress component of the single element, due to the i-th imposed deformation. In this way, with a single FEM run, characterized by six sequential imposed deformations, the algorithm allows to calculate all the components of the stiffness matrix with eq. 6 (which provides $\overline{\overline{C_{ij}}}$ values). The algorithm is, finally, able to provide, as the output, the stiffness and compliance matrices of the examined composite material.

Choice on the RVE size

An original criterion has been used (Naddeo *et al.*, 2014) to optimize the size of the RVE, taking into account the accuracy of statistical computation and the computational burden, assuring that RVE is statistically representative. The assumption is that the nanoscale structure has an isotropic behavior. In small RVEs, the position of fibers may affect the isotropic degree; for this reason, a criterion, directly related to the number of polymeric fibers (number of tetrahedra), has been used choosing the size of RVE. The criterion is based on the minimization of the following function:

$$|\Delta|^2 = \sum_{i,j=1}^{6} \left(C_{i,j} - C^I_{i,j}(\lambda, G) \right)^2 \tag{8}$$

in which $C_{i,j}$ is the i, j-th component of the stiffness matrix extrapolated from FEM calculation, $C^I_{i,j}$ is the i, j-th component of the unknown isotropic stiffness matrix, λ and G represent the independent parameters that define the isotropic stiffness matrix (Lamè constants).

The minimization of eq. 8 leads to the determination of λ and G, parameters that define the isotropic material closer (with regard to the mechanical behavior) to the material simulated by the *Ansys* calculation. Consequently, the algorithm calculates the parameter δ, given by the ratio between the norm of the "*difference tensor*" $\Delta = C - C^I$ and the norm of the tensor C^I, which provides information about isotropicity in the model, depending on the size of RVE (in terms of tetrahedron mean size). Being Lrve the edge of the cubic RVE, this criterion showed that, for RVE having tetrahedron mean size smaller than Lrve/12, the value of the parameter δ tends to a small constant value.

Analysis of the results and verification of the stiffness of the proposed structure

Once realized the RVE space frame, setting the nanoscale porosity P_n, the ratio between the average diameter and the length of the cylindrical fibers was univocally determined. As previously stated, the model of the porous nanoscale structure, characterized by an input Young's modulus equal to that of the compact and untreated PLLA (E_I), should give us as output, a value equal to E_n.

In this case $E_I = 1974 \times 10^3$ kPa (Lu *et al.*, 2007), the experimentally measured Young's modulus of the PLLA gelled without fillers (HA) (total porosity $P_{tot} = 0.96$) was $E_{ex} = 81$ kPa and the Young's modulus as output of the nanoscale structure should be $E_n = E_{ex}/0.0688 = 1177.33$ kPa. FEM model gives us approximately $E_n = 68281$ kPa. Thus, despite a significant decrease of the structural characteristics (of the order of 96.5%), this structure remains remarkably rigid and modeling results are very far from the experimental data.

In the authors' opinion, what can determine the further decrease of the mechanical characteristics in the structure, is the particular shape of the cylindrical fibers observed in FESEM images (Figures V.61 and V.62a). They show an average curvature that leads to a buckling tendency, determining a higher compliance of the entire structure. This observation is supported by a previous study (Ma *et al.*, 2002) revealing that loop structure is lacking in the modeled gels. For this reason, a further modeling was developed to address loop formation, during the gel aggregation process, discovering that bending was the major mode of deformation of the network. Also Pinrad (Pirard *et al.*, 1997) proposed a mechanism based on the preferential buckling of the network around larger pores.

To take into account these characteristics, first, we realized a parametric modeling of a single cylindrical curved fiber, modeled choosing, as the cylinder axis, a spline curve interpolating three points, two of which coincident with the endpoints of the rod of length L and a third in a central position at a distance d from the rod axis. By computing the Young's modulus of the curved rod varying the curvature determined by the size of the parameter *d*, maintaining volume and section at a constant value and considering the force directed along the line connecting the two end points of the curved rod, we obtained a decrease of the Young's modulus of more than two orders of magnitude in the transition from $d = 0$ *to* $d = 0.5L$. For this reason, we implemented in the main algorithm, a routine that substitutes the beams of the Space above, with parametric curved rods. FEM discretization was realized using quadratic (three-node) multi-layered pipe elements in 3-D, suitable to model the filler (HA) that tends to cover PLLA fibers. A convergence analysis of the results has been made taking into account the computational effort.

Identification of the configuration that achieves the desired results in terms of the mechanical response

The total volume of the described structure is:

$$V_p = \sum_{i=1}^{n} L_i(d)\Sigma \tag{9}$$

being n the total number of fibers, V_p the volume occupied by the polymeric matrix, L_i the length of the i-th spline which is a function of the parameter d and Σ the section of the fiber which does not vary with the i. The introduced routine is able to realize an interpolating spline curve of output data points that describes the function $E = E(d)$ maintaining constant $P_n = 0.8$ using the relation (9). Introducing E = 1177.33 kPa, the interpolating curve gives the value $d = 0.4514$. Therefore, introducing this value as input, it is possible to reach a value equal to about $E_n = 1178$ kPa; i.e., very close to that expected. Introducing, this value as input in the micrometric porosity model previously described, we can get a value of $E_{FEM} = 81.41$ kPa, that is very close to the one experimentally measured that is equal to $E_{ex} = 81$ kPa.

V.7.3.3 Modeling of the filler (HA)

Modeling of HA filler has been obtained on the basis of the information coming from FESEM images and studying the mechanical experimental curves. In particular, it is possible to make some considerations on the trend of the experimental curve of Young's modulus when the weight percentage of the filler is increased (Table V.7).

FESEM images show that multi-layer decoration of the nanofibers increases with the weight percentage of HA up to 30% w/w (Figure V.61b). For higher HA percentages, Young's modulus only slightly increases. We suppose that this is an indication of the fact that exceeding HA deposited inside the micrometric pores of the structure (see Figure V.62c). It is, therefore, possible to imagine that two coaxial cylinders are formed, in which the external one is the filler that realizes a kind of multi-layer coating or decoration on the polymer matrix represented by the inner cylinder. FESEM images (Figure V.62b) indicate an extensive HA nanoparticles coverage of the nanofibers in the case of a relatively open network; this coverage is not homogeneous in thickness and spot decorations are evident. We have no indication about the coverage of the nanofibers located in the most internal part of the network. If HA nanoparticles adhesion is due to electrostatic interactions among HA nanoparticles and PLLA nanofibers, multi-layer decoration can be explained as the nanoparticles adhesion until the local surface electric charge has been completely neutralized. Moreover, since electrostatic charges tend to dispose on the external surfaces of a solid system, it is possible that nanofibers in the internal part of the network could bear a reduced or zero electric charge and, as a consequence, are not (or partly) covered by HA nanoparticles. For this reasons, we decided to model the second cylinder as partially covering the inner one, introducing a *"loaded surface index"* defined as $C_i = L_c/L$, being L_c the portion of PLLA cylinder fiber covered by HA and L the length of the cylinder fiber. The idea is to model the generic PLLA fiber coated by HA as shown in Figure V.67.

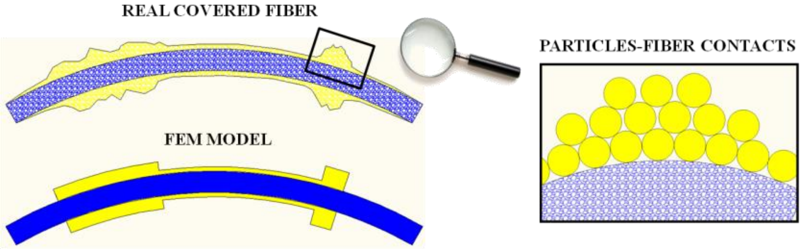

Figure V.67 *Schematic example of a covered fiber section: on the left, relation between real fiber and FEM model; on the right, a detail of the contact between HA particles and PLLA fiber*

For this reason, it was first realized a finite element model of a single partially covered rod ($C_i = 0.33$). FEM tensile tests confirmed the plateau effect of the Young's modulus with the increasing weight percentage of HA recorded in the experimental tests (Figure V.68) for HA weight percentages larger than 30% w/w.

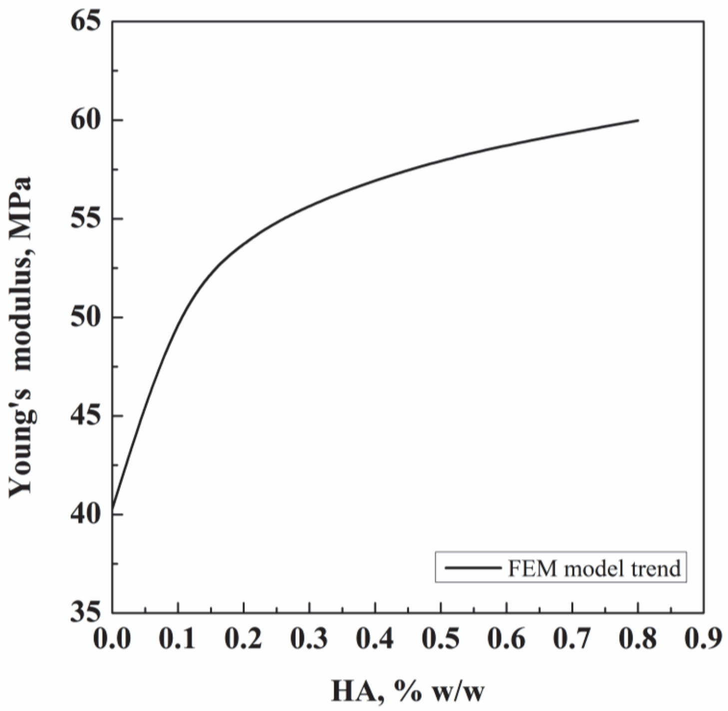

Figure V.68 *Plateau effect of the Young's modulus with the increasing weight percentage of HA for a single fiber FEM model*

The next step was the implementation of an additional routine able to:

- select a given percentage of geometric lines (forming the axis of symmetry of the curved cylindrical fibers) according to a given "loaded surface index" C_i (defined as above);
- calculate the thickness of HA coating based on the weight percentage of HA and the specific weight of both PLLA and HA;
- mesh the selected lines, representing the areas covered by HA, with multi-layered elements described in the previous paragraph.

In Figure V.69, a cubic RVE of the nanostructured model, in which it is possible to distinguish the inflected PLLA fibers partially covered by HA, is shown.

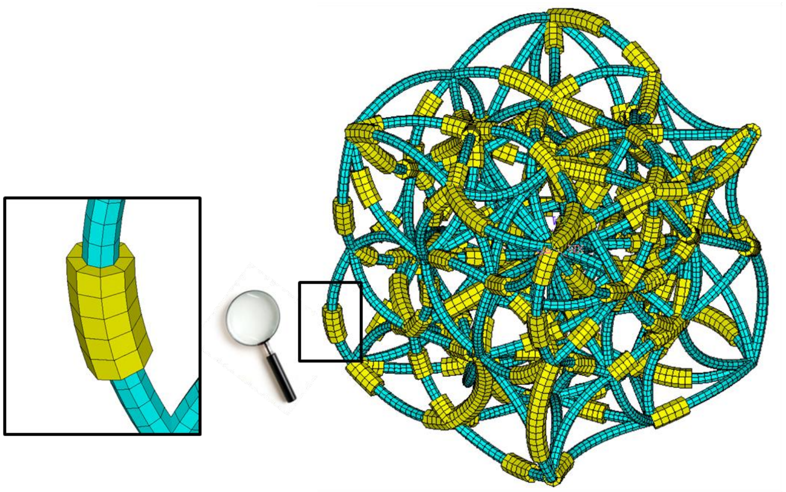

Figure V.69 *Explanatory example of a cubic RVE of the nanostructured model: PLLA (blue elements); HA (yellow elements)*

We calibrated the "loaded surface index" starting from C_i = 0.0 to approximate the resulting Young's modulus to the corresponding experiments, with the maximum weight percentage of HA. Introducing for HA as input, a Young's modulus equal to E_{HA} = 114 GPa (Katz *et al.*, 1971; Gilmore *et al.*, 1982) and a Poisson ratio equal to ν_{HA} = 0.262 (Ching *et al.*, 2009), we obtained for the model a Young's modulus equal to E = 122.82 kPa in correspondence of C_i = 0.14, which is a value fairly close to the one experimentally obtained (E_{ex} = 122 kPa). The resulting value for the "loaded surface index" can be easily explained also taking into account the quasi-spherical shape of HA particles; the contact on the nanofibers, therefore, occurs only on the small areas of contact between PLLA fiber and the quasi-spherical shaped HA particles, leaving the remaining parts free from interactions (see also Figure V.67).

V.7.4 Discussion, conclusions and perspectives

Once the "loaded surface index" was set at C_i = 0.14, we realized a series of finite element analyses to model all the other weight percentages of HA experimentally used, assuming that the "loaded surface index" remained constant. The curve in Figure V.70 allows the comparison of experimental and numerical results in terms of Young's modulus.

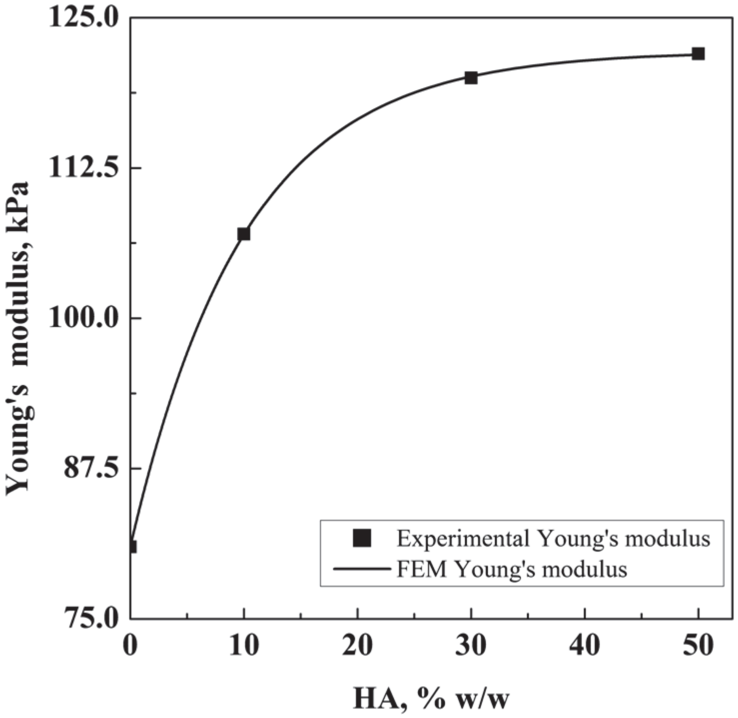

Figure V.70 *Superposition of the numerical results on the experimental results*

It is useful to remind that FEM results have been obtained by the combination of both FEM model of the composite micrometric porous structure and FEM model of the nanoscale structure, varying only the weight percentage of HA introduced in input in FEM modeling algorithm. This comparison also confirms the plateau effect experimentally recorded for HA loadings larger than 30% w/w.

Summarizing the results, this work showed that the combination of FEM model of the composite micrometric porous structure based on the theory of hcp and the nanoscale structure of PLLA scaffold, modeled as a quite regular space frame of isotropic curved fibers without any “dead-ends” or discontinuities, is able to well reproduce our experimental results, when we set a porosity equal to the one experimentally recorded both at micrometric and at nanometric level. A mechanical response highly adherent to the experimental one has been obtained; it confirms the hypothesis, corroborated by other works in the literature (Pirard *et al.*, 1997; Ma *et al.*, 2002), that the decrease of the mechanical properties of aerogels depends on how the fiber network is connected in the space and that bending is the major mode of deformation of the network, caused by the buckling tendency of the curved fibers. Furthermore, the parametric modeling of HA nanoparticles, forming a sort of cylinder that cover PLLA fibers with a limit in “loaded surface” at higher HA amounts, confirms the reinforcement mechanism for which HA tends to increase the fiber thickness of the already covered zones. Therefore, HA coverage of PLLA fibers increases their stiffness and produces the macroscopic increase of Young’s modulus. This phenomenon goes on until the electrostatic force between HA particles and PLLA fiber becomes negligible. As a consequence, the other HA nanoparticles start to deposit on the bottom of the microporous cavities in the scaffold and do not give any further contribution to the mechanical resistance of the structure. It is possible to formulate another hypothesis about the overall stiffness of the nanofibrous structure beyond the range of small displacements: HA nanoparticles decoration obstacles the nanofibers relative motion, increasing the friction and partly blocking them. It is also possible that rigidity increase and movement obstacle mechanisms can coexist.

In the perspective, the idea is to use the model we developed as a tool to understand/confirm the interactions among other structures (pores/nanofilaments) and/or materials involved.

Numerical analyses allow us to discover, through sensitivity analyses, the parameters to be controlled during the supercritical process. An example might be the analysis of the influence, on the mechanical behavior of the structure, of the porosity imparted by the porogen, that can be directly related also to the pressure used to produce the contact among the porogen particles to induce the interconnections among the pores.

Another example of the utility of this parametric FEM model concerns the control of the interaction between PLLA and HA. By opportune simulations, it is possible to observe that, using the same weight percentage of HA, but increasing the “loaded surface”, we can largely increase the overall mechanical characteristics of the composite. This means that, during scaffold production, the study could be focused in achieving a more uniform distribution of HA on the PLLA network fibers that may depend on the particle size and shape of the material introduced in the process, which can ensure a greater contact surface between particles and fiber.

Possible future developments of FEM model may be: the development of a method to estimate the amount of precipitated particles for a better approximation of the real composite structure; the evaluation of the effect of large deformations, implementing new material characteristics to contemplate the field of geometrical and material nonlinearity and the introduction of the influence of the mutual contacts among the various composite components.

CHAPTER V

CHAPTER VI. Conclusions

In this work, 3-D, nano- and microporous structures also loaded with bioactive materials, were produced using green supercritical assisted processes. These materials can be used for bone, tendon and vascular regeneration, when different biopolymers and arrangements are adopted. It was demonstrated that thanks to SC-CO_2 processing, these structures maintained their native organization at nanoscale, simulating the tissue ECM and were organic solvent and crosslinker residues free. Therefore, they can be safely used in nanomedicine for tissue engineering applications. For the first time, a FEM modeling to understand the mechanical interactions in composite polymeric structures, was developed in the case of PLLA scaffolds loaded with HA nanoparticles. It was able to model properly the properties of the composite scaffolds and will be used in the next future to model/simulate different biomaterials developed for scaffolding applications.

In perspectives, cells cultivation on the produced structures and *in vivo* experimentation with the help of M.D. colleagues in different laboratories at Faculty of Medicine (University of Salerno, Italy), San Martino Hospital (Genoa, Italy), University of Maryland (USA), etc., will be performed, completing the translation from smart 3-D structures to clinical applications.

CHAPTER VI

REFERENCES

Ali, F., Agarwal, N., Nayak, P. K., Das, R. and Periasamy, N. (2009) Chemical route to the formation of graphene. *Current science*, **97**, 683-685.

Annabi, N., Mithieux, S. M., Weiss, A. S. and Dehghani, F. (2009) The fabrication of elastin-based hydrogels using high pressure CO_2. *Biomaterials*, **30**, 1-7.

Annabi, N., Mithieux, S. M., Weiss, A. S. and Dehghani, F. (2010) Cross-linked open-pore elastic hydrogels based on tropoelastin, elastin and high pressure CO_2. *Biomaterials*, **31**, 1655-1665.

Arora, K. A., Lesser, A. J. and McCarthy, T. J. (1998) Preparation and characterization of microcellular polystyrene foams processed in supercritical carbon dioxide. *Macromolecules*, **31**, 4614-4620.

Barnes, C. P., Sell, S. A., Boland, E. D., Simpson, D. G. and Bowlin, G. L. (2007) Nanofiber technology: Designing the next generation of tissue engineering scaffolds. *Advanced drug delivery reviews*, **59**, 1413-1433.

Barroso-Bujans, F., Alegría, A. N. and Colmenero, J. (2010) Kinetic study of the graphite oxide reduction: combined structural and gravimetric experiments under isothermal and nonisothermal conditions. *The Journal of Physical Chemistry C*, **114**, 21645-21651.

Barry, J. J., Nazhat, S. N., Rose, F. R., Hainsworth, A. H., Scotchford, C. A. and Howdle, S. M. (2005) Supercritical carbon dioxide foaming of elastomer/heterocyclic methacrylate blends as scaffolds for tissue engineering. *Journal of Materials Chemistry*, **15**, 4881-4888.

Barry, J. J., Silva, M. M., Cartmell, S. H., Guldberg, R. E., Scotchford, C. A. and Howdle, S. M. (2006) Porous methacrylate tissue engineering scaffolds: using carbon dioxide to control porosity and interconnectivity. *Journal of materials science*, **41**, 4197-4204.

Berkland, C., Kim, K. K. and Pack, D. W. (2003) PLG microsphere size controls drug release rate through several competing factors. *Pharmaceutical research*, **20**, 1055-1062.

Berkland, C., King, M., Cox, A., Kim, K. K. and Pack, D. W. (2002) Precise control of PLG microsphere size provides enhanced control of drug release rate. *Journal of controlled release*, **82**, 137-147.

Betz, M. W., Modi, P. C., Caccamese, J. F., Coletti, D. P., Sauk, J. J. and Fisher, J. P. (2008) Cyclic acetal hydrogel system for bone marrow stromal cell encapsulation and osteodifferentiation. *Journal of Biomedical Materials Research Part A*, **86**, 662-670.

Bhattarai, S. R., Bhattarai, N., Yi, H. K., Hwang, P. H., Cha, D. I. and Kim, H. Y. (2004) Novel biodegradable electrospun membrane: scaffold for tissue engineering. *Biomaterials*, **25**, 2595-2602.

Bigi, A., Cojazzi, G., Panzavolta, S., Rubini, K. and Roveri, N. (2001) Mechanical and thermal properties of gelatin films at different degrees of glutaraldehyde crosslinking. *Biomaterials*, **22**, 763-768.

Blaker, J., Gough, J., Maquet, V., Notingher, I. and Boccaccini, A. (2003) In vitro evaluation of novel bioactive composites based on Bioglass®-filled polylactide foams for bone tissue engineering scaffolds. *Journal of Biomedical Materials Research Part A*, **67**, 1401-1411.

Borden, M., Attawia, M., Khan, Y., El-Amin, S. and Laurencin, C. (2004) Tissue-engineered bone formation in vivo using a novel sintered polymeric microsphere matrix. *Journal of Bone & Joint Surgery, British Volume*, **86**, 1200-1208.

Bryant, S. J. and Anseth, K. S. (2001) The effects of scaffold thickness on tissue engineered cartilage in photocrosslinked poly (ethylene oxide) hydrogels. *Biomaterials*, **22**, 619-626.

Cabodi, M., Choi, N. W., Gleghorn, J. P., Lee, C. S., Bonassar, L. J. and Stroock, A. D. (2005) A microfluidic biomaterial. *Journal of the American Chemical Society*, **127**, 13788-13789.

Cançado, L. G., Jorio, A., Ferreira, E. H. M., Stavale, F., Achete, C. A., Capaz, R. B., Moutinho, M. V. O., Lombardo, A., Kulmala, T. S. and Ferrari, A. C. (2011) Quantifying Defects in Graphene via Raman Spectroscopy at Different Excitation Energies. *Nano letters*, **11**, 3190-3196.

Cantón, I., Mckean, R., Charnley, M., Blackwood, K. A., Fiorica, C., Ryan, A. J. and MacNeil, S. (2010) Development of an Ibuprofen-releasing biodegradable PLA/PGA electrospun scaffold for tissue regeneration. *Biotechnology and bioengineering*, **105**, 396-408.

Cao, J.-H., Zhu, B.-K., Ji, G.-L. and Xu, Y.-Y. (2005) Preparation and characterization of PVDF–HFP microporous flat membranes by supercritical CO_2 induced phase separation. *Journal of Membrane Science*, **266**, 102-109.

Cardea, S., Baldino, L., Pisanti, P. and Reverchon, E. (2014a) 3-D PLLA scaffolds formation by a supercritical freeze extraction assisted process. *Journal of Materials Science: Materials in Medicine*, **25**, 355-362.

Cardea, S., Baldino, L., Scognamiglio, M. and Reverchon, E. (2014b) 3D PLLA/Ibuprofen composite scaffolds obtained by a supercritical fluids assisted process. *Journal of Materials Science: Materials in Medicine*, **25**, 989-998.

Cardea, S., Gugliuzza, A., Schiavo Rappo, E., Aceto, M., Drioli, E. and Reverchon, E. (2006) Generation of PEEK-WC membranes by supercritical fluids. *Desalination*, **200**, 58-60.

Cardea, S. and Reverchon, E. (2011) Nanostructured PVDF-HFP membranes loaded with catalyst obtained by supercritical CO_2 assisted techniques. *Chemical Engineering and Processing: Process Intensification*, **50**, 630-636.

Cardea, S., Sessa, M. and Reverchon, E. (2010) Supercritical phase inversion to form drug-loaded poly (vinylidene fluoride-co-hexafluoropropylene) membranes. *Industrial & Engineering Chemistry Research*, **49**, 2783-2789.

Cascone, M., Barbani, N., P. Giusti, C. C., Ciardelli, G. and Lazzeri, L. (2001) Bioartificial polymeric materials based on polysaccharides. *Journal of Biomaterials Science, Polymer Edition*, **12**, 267-281.

Chai, B., Li, J., Xu, Q. and Dai, K. (2014) Facile synthesis of reduced graphene oxide/WO_3 nanoplates composites with enhanced photocatalytic activity. *Materials Letters*, **120**, 177-181.

Chen, F., Yoo, J. J. and Atala, A. (1999) Acellular collagen matrix as a possible “off the shelf” biomaterial for urethral repair. *Urology*, **54**, 407-410.

Chen, L. and Wang, M. (2002) Production and evaluation of biodegradable composites based on PHB–PHV copolymer. *Biomaterials*, **23**, 2631-2639.

Ching, W., Rulis, P. and Misra, A. (2009) Ab initio elastic properties and tensile strength of crystalline hydroxyapatite. *Acta Biomaterialia*, **5**, 3067-3075.

Ciambelli, P., Sarno, M., Gorrasi, G., Sannino, D., Tortora, M. and Vittoria, V. (2005) Preparation and physical properties of carbon nanotubes–PVA nanocomposites. *Journal of Macromolecular Science, Part B: Physics*, **44**, 779-795.

Ciardelli, G., Chiono, V., Vozzi, G., Pracella, M., Ahluwalia, A., Barbani, N., Cristallini, C. and Giusti, P. (2005) Blends of poly-(ε-caprolactone) and polysaccharides in tissue engineering applications. *Biomacromolecules*, **6**, 1961-1976.

Compton, O. C., Jain, B., Dikin, D. A., Abouimrane, A., Amine, K. and Nguyen, S. T. (2011) Chemically active reduced graphene oxide with tunable C/O ratios. *Acs Nano*, **5**, 4380-4391.

Conte, A., Buonocore, G., Sinigaglia, M. and Del Nobile, M. (2007) Development of immobilized lysozyme based active film. *Journal of Food Engineering*, **78**, 741-745.

Cricrì, G., Garofalo, E., Naddeo, F. and Incarnato, L. (2012) Stiffness constants prediction of nanocomposites using a periodic 3D-FEM model. *Journal of Polymer Science Part B: Polymer Physics*, **50**, 207-220.

Cui, P., Lee, J., Hwang, E. and Lee, H. (2011) One-pot reduction of graphene oxide at subzero temperatures. *Chemical Communications*, **47**, 12370-12372.

Dahms, S., Piechota, H., Dahiya, R., Lue, T. and Tanagho, E. (1998) Composition and biomechanical properties of the bladder acellular matrix graft: comparative analysis in rat, pig and human. *British journal of urology*, **82**, 411-419.

Dahms, S. E., Piechota, H. J., Nunes, L., Dahiya, R., Lue, T. F. and Tanagho, E. A. (1997) Free ureteral replacement in rats: regeneration of ureteral wall components in the acellular matrix graft. *Urology*, **50**, 818-825.

Della Porta, G., Del Gaudio, P., De Cicco, F., Aquino, R. P. and Reverchon, E. (2013) Supercritical drying of alginate beads for the development of aerogel biomaterials: optimization of process parameters and exchange solvents. *Industrial & Engineering Chemistry Research*, **52**, 12003-12009.

Diamond, L. W. and Akinfiev, N. N. (2003) Solubility of CO_2 in water from −1.5 to 100 °C and from 0.1 to 100 MPa: evaluation of literature data and thermodynamic modelling. *Fluid Phase Equilibria*, **208**, 265-290.

Du, J., Tan, E., Kim, H. J., Zhang, A., Bhattacharya, R. and Yarema, K. J. (2014) Comparative evaluation of chitosan, cellulose acetate, and polyethersulfone nanofiber scaffolds for neural differentiation. *Carbohydrate polymers*, **99**, 483-490.

Duarte, A. R. C., Caridade, S. G., Mano, J. F. and Reis, R. L. (2009a) Processing of novel bioactive polymeric matrixes for tissue engineering using supercritical fluid technology. *Materials Science and Engineering: C*, **29**, 2110-2115.

Duarte, A. R. C., Mano, J. F. and Reis, R. L. (2009b) Dexamethasone-loaded scaffolds prepared by supercritical-assisted phase inversion. *Acta Biomaterialia*, **5**, 2054-2062.

Duarte, A. R. C., Mano, J. F. and Reis, R. L. (2009c) Preparation of chitosan scaffolds loaded with dexamethasone for tissue engineering applications using supercritical fluid technology. *European Polymer Journal*, **45**, 141-148.

Duarte, A. R. C., Mano, J. F. and Reis, R. L. (2009d) Preparation of starch-based scaffolds for tissue engineering by supercritical immersion precipitation. *The Journal of Supercritical Fluids*, **49**, 279-285.

Duarte, A. R. C., Mano, J. F. and Reis, R. L. (2010) Novel 3D scaffolds of chitosan–PLLA blends for tissue engineering applications: Preparation and characterization. *The Journal of Supercritical Fluids*, **54**, 282-289.

Eigler, S., Dotzer, C. and Hirsch, A. (2012a) Visualization of defect densities in reduced graphene oxide. *Carbon*, **50**, 3666-3673.

Eigler, S., Dotzer, C., Hirsch, A., Enzelberger, M. and Müller, P. (2012b) Formation and decomposition of CO_2 intercalated graphene oxide. *Chemistry of Materials*, **24**, 1276-1282.

Entcheva, E., Bien, H., Yin, L., Chung, C.-Y., Farrell, M. and Kostov, Y. (2004) Functional cardiac cell constructs on cellulose-based scaffolding. *Biomaterials*, **25**, 5753-5762.

Erickson, K., Erni, R., Lee, Z., Alem, N., Gannett, W. and Zettl, A. (2010) Determination of the local chemical structure of graphene oxide and reduced graphene oxide. *Advanced Materials*, **22**, 4467-4472.

Freed, L. E. and Vunjak-Novakovic, G. (1998) Culture of organized cell communities. *Advanced drug delivery reviews*, **33**, 15-30.

Fuchs, J. R., Nasseri, B. A. and Vacanti, J. P. (2001) Tissue engineering: a 21st century solution to surgical reconstruction. *The Annals of thoracic surgery*, **72**, 577-591.

Ganguly, A., Sharma, S., Papakonstantinou, P. and Hamilton, J. (2011) Probing the thermal deoxygenation of graphene oxide using high-resolution in situ X-ray-based spectroscopies. *The Journal of Physical Chemistry C*, **115**, 17009-17019.

Garlotta, D. (2001) A literature review of poly (lactic acid). *Journal of Polymers and the Environment*, **9**, 63-84.

Gilbert, T. W., Sellaro, T. L. and Badylak, S. F. (2006) Decellularization of tissues and organs. *Biomaterials*, **27**, 3675-3683.

Gilmore, R. and Katz, J. (1982) Elastic properties of apatites. *Journal of Materials Science*, **17**, 1131-1141.

Goel, S. K. and Beckman, E. J. (1994) Generation of microcellular polymeric foams using supercritical carbon dioxide. I: Effect of pressure and temperature on nucleation. *Polymer Engineering & Science*, **34**, 1137-1147.

Gunatillake, P., Mayadunne, R. and Adhikari, R. (2006) Recent developments in biodegradable synthetic polymers. *Biotechnology annual review*, **12**, 301-347.

Gunatillake, P. A. and Adhikari, R. (2003) Biodegradable synthetic polymers for tissue engineering. *Eur Cell Mater*, **5**, 1-16.

Hacker, M., Tessmar, J., Neubauer, M., Blaimer, A., Blunk, T., Göpferich, A. and Schulz, M. B. (2003) Towards biomimetic scaffolds: anhydrous scaffold fabrication from biodegradable amine-reactive diblock copolymers. *Biomaterials*, **24**, 4459-4473.

Harris, L., Mooney, D. J. and Shea, L. (2001). Open pore biodegradable matrices, Google Patents.

Harris, L. D., Kim, B.-S. and Mooney, D. J. (1998) Open pore biodegradable matrices formed with gas foaming.

Hench, L. (1993) Bioceramics: from concept to clinic. *American Ceramic Society Bulletin*, **72**, 93-98.

Hench, L. L. (1991) Bioceramics: from concept to clinic. *Journal of the American Ceramic Society*, **74**, 1487-1510.

Hentrich, R., Graves, G., Stein, H. and Bajpai, P. (1971) An evaluation of inert and resorbale ceramics for future clinical orthopedic applications. *Journal of biomedical materials research*, **5**, 25-51.

Hoenich, N. A. (2007) Cellulose for medical applications: past, present, and future. *BioResources*, **1**, 270-280.

Holy, C. E., Dang, S. M., Davies, J. E. and Shoichet, M. S. (1999) In vitro degradation of a novel poly (lactide-co-glycolide) 75/25 foam. *Biomaterials*, **20**, 1177-1185.

Hou, Q., Grijpma, D. W. and Feijen, J. (2003) Porous polymeric structures for tissue engineering prepared by a coagulation, compression moulding and salt leaching technique. *Biomaterials*, **24**, 1937-1947.

Hu, J., Sun, X., Ma, H., Xie, C., Chen, Y. E. and Ma, P. X. (2010) Porous nanofibrous PLLA scaffolds for vascular tissue engineering. *Biomaterials*, **31**, 7971-7977.

Hua, F. J., Kim, G. E., Lee, J. D., Son, Y. K. and Lee, D. S. (2002) Macroporous poly (L-lactide) scaffold 1. Preparation of a macroporous scaffold by liquid–liquid phase separation of a PLLA–dioxane–water system. *Journal of biomedical materials research*, **63**, 161-167.

Idris, A. and Yet, L. K. (2006) The effect of different molecular weight PEG additives on cellulose acetate asymmetric dialysis membrane performance. *Journal of Membrane Science,* **280**, 920-927.

Jacobs, M. A., Kemmere, M. F. and Keurentjes, J. T. F. (2004) Foam processing of poly(ethylene-co-vinyl acetate) rubber using supercritical carbon dioxide. *Polymer*, **45**, 7539-7547.

Jagur-Grodzinski, J. (2006) Polymers for tissue engineering, medical devices, and regenerative medicine. Concise general review of recent studies. *Polymers for Advanced Technologies*, **17**, 395-418.

Jaklenec, A., Hinckfuss, A., Bilgen, B., Ciombor, D. M., Aaron, R. and Mathiowitz, E. (2008a) Sequential release of bioactive IGF-I and TGF-β1 from PLGA microsphere-based scaffolds. *Biomaterials*, **29**, 1518-1525.

Jaklenec, A., Wan, E., Murray, M. E. and Mathiowitz, E. (2008b) Novel scaffolds fabricated from protein-loaded microspheres for tissue engineering. *Biomaterials*, **29**, 185-192.

Jenkins, M., Harrison, K., Silva, M., Whitaker, M., Shakesheff, K. and Howdle, S. (2006) Characterisation of microcellular foams produced from semi-crystalline PCL using supercritical carbon dioxide. *European Polymer Journal*, **42**, 3145-3151.

Jha, B. S., Colello, R. J., Bowman, J. R., Sell, S. A., Lee, K. D., Bigbee, J. W., Bowlin, G. L., Chow, W. N., Mathern, B. E. and Simpson, D. G. (2011) Two pole air gap electrospinning: fabrication of highly aligned, three-dimensional scaffolds for nerve reconstruction. *Acta Biomaterialia*, **7**, 203-215.

Ji, C., Annabi, N., Khademhosseini, A. and Dehghani, F. (2011) Fabrication of porous chitosan scaffolds for soft tissue engineering using dense gas CO_2. *Acta Biomaterialia*, **7**, 1653-1664.

Katz, J. and Ukraincik, K. (1971) On the anisotropic elastic properties of hydroxyapatite. *Journal of biomechanics*, **4**, 221-227.

Kim, H. W., Lee, E. J., Jun, I. K., Kim, H. E. and Knowles, J. C. (2005) Degradation and drug release of phosphate glass/polycaprolactone biological composites for hard-tissue regeneration. *Journal of Biomedical Materials Research Part B: Applied Biomaterials*, **75**, 34-41.

Kim, M.-S. and Lee, S.-J. (2004) Characteristics of porous polycarbonate membrane with polyethylene glycol in supercritical CO_2 and effect of its porosity on tearing stress. *The Journal of Supercritical Fluids*, **31**, 217-225.

Kim, S.-S., Sun Park, M., Jeon, O., Yong Choi, C. and Kim, B.-S. (2006) Poly(lactide-co-glycolide)/hydroxyapatite composite scaffolds for bone tissue engineering. *Biomaterials*, **27**, 1399-1409.

Krause, B., Diekmann, K., Van der Vegt, N. and Wessling, M. (2002) Open nanoporous morphologies from polymeric blends by carbon dioxide foaming. *Macromolecules*, **35**, 1738-1745.

Krishnamoorthy, K., Kim, G.-S. and Kim, S. J. (2013) Graphene nanosheets: ultrasound assisted synthesis and characterization. *Ultrasonics sonochemistry*, **20**, 644-649.

Kudin, K. N., Ozbas, B., Schniepp, H. C., Prud'Homme, R. K., Aksay, I. A. and Car, R. (2008) Raman spectra of graphite oxide and functionalized graphene sheets. *Nano letters*, **8**, 36-41.

Kutowy, O. and Sourirajan, S. (1975) Cellulose acetate ultrafiltration membranes. *Journal of applied polymer science*, **19**, 1449-1460.

Lee, B., Freitag, D., Arlt, W. and McHugh, M. (2007) Hollow fibers by electrospinning in supercritical CO_2. *Materials Science*, **2**.

Lee, C., Wei, X., Kysar, J. W. and Hone, J. (2008) Measurement of the elastic properties and intrinsic strength of monolayer graphene. *Science*, **321**, 385-388.

Levit, N. and Tepper, G. (2004) Supercritical CO_2-assisted electrospinning. *The Journal of Supercritical Fluids*, **31**, 329-333.

Liu, X. and Ma, P. X. (2004) Polymeric scaffolds for bone tissue engineering. *Annals of biomedical engineering*, **32**, 477-486.

Lo, H., Ponticiello, M. and Leong, K. (1995) Fabrication of controlled release biodegradable foams by phase separation. *Tissue engineering*, **1**, 15-28.

Lu, J., Qiu, Z. and Yang, W. (2007) Fully biodegradable blends of poly (l-lactide) and poly (ethylene succinate): miscibility, crystallization, and mechanical properties. *Polymer*, **48**, 4196-4204.

Luetzow, K., Klein, F., Weigel, T., Apostel, R., Weiss, A. and Lendlein, A. (2007) Formation of poly(ε-caprolactone) scaffolds loaded with small molecules by integrated processes. *Journal of Biomechanics*, **40**, Supplement 1, S80-S88.

Luu, Y., Kim, K., Hsiao, B., Chu, B. and Hadjiargyrou, M. (2003) Development of a nanostructured DNA delivery scaffold via electrospinning of PLGA and PLA–PEG block copolymers. *Journal of controlled release*, **89**, 341-353.

Ma, H.-S., Prévost, J.-H., Jullien, R. and Scherer, G. W. (2001a) Computer simulation of mechanical structure–property relationship of aerogels. *Journal of non-crystalline solids*, **285**, 216-221.

Ma, H.-S., Prévost, J.-H. and Scherer, G. W. (2002) Elasticity of DLCA model gels with loops. *International journal of solids and structures*, **39**, 4605-4614.

Ma, H.-S., Roberts, A. P., Prévost, J.-H., Jullien, R. and Scherer, G. W. (2000) Mechanical structure–property relationship of aerogels. *Journal of non-crystalline solids*, **277**, 127-141.

Ma, P. X. (2004) Scaffolds for tissue fabrication. *Materials today*, **7**, 30-40.

Ma, P. X. (2008) Biomimetic materials for tissue engineering. *Advanced drug delivery reviews*, **60**, 184-198.

Ma, P. X. and Zhang, R. (1999) Synthetic nano-scale fibrous extracellular matrix.

Ma, P. X. and Zhang, R. (2001b) Microtubular architecture of biodegradable polymer scaffolds. *Journal of biomedical materials research*, **56**, 469-477.

Ma, P. X., Zhang, R., Xiao, G. and Franceschi, R. (2001c) Engineering new bone tissue in vitro on highly porous poly (α-hydroxyl acids)/hydroxyapatite composite scaffolds. *Journal of biomedical materials research*, **54**, 284-293.

Ma, Z., Kotaki, M., Inai, R. and Ramakrishna, S. (2005) Potential of nanofiber matrix as tissue-engineering scaffolds. *Tissue engineering*, **11**, 101-109.

Mathieu, L., Montjovent, M. O., Bourban, P. E., Pioletti, D. P. and Månson, J. A. (2005) Bioresorbable composites prepared by supercritical fluid foaming. *Journal of Biomedical Materials Research Part A*, **75**, 89-97.

Mathieu, L. M., Mueller, T. L., Bourban, P.-E., Pioletti, D. P., Müller, R. and Månson, J.-A. E. (2006) Architecture and properties of anisotropic polymer composite scaffolds for bone tissue engineering. *Biomaterials*, **27**, 905-916.

Mayer-Wagner, S., Schiergens, T., Sievers, B., Redeker, J., Schmitt, B., Buettner, A., Jansson, V. and Müller, P. (2011) Scaffold-free 3D cellulose acetate membrane-based cultures form large cartilaginous constructs. *Journal of tissue engineering and regenerative medicine*, **5**, 151-155.

McHugh, M., Marquez, M., Shen, Z., Liu, J. and Lee, S. (2007). Supercritical fluid-assisted electrospinning of polymers. APS Meeting Abstracts.

Mecitoğlu, Ç., Yemenicioğlu, A., Arslanoğlu, A., Elmacı, Z. S., Korel, F. and Çetin, A. E. (2006) Incorporation of partially purified hen egg white lysozyme into zein films for antimicrobial food packaging. *Food Research International*, **39**, 12-21.

Meng, Q. and Wu, D. (2004) A study of bubble inflation in polymers and its applications. *Physics Letters A*, **327**, 61-66.

Mikos, A. G., Lyman, M. D., Freed, L. E. and Langer, R. (1994) Wetting of poly (L-lactic acid) and poly (DL-lactic-co-glycolic acid) foams for tissue culture. *Biomaterials*, **15**, 55-58.

Mooney, D. J., Baldwin, D. F., Suh, N. P., Vacanti, J. P. and Langer, R. (1996) Novel approach to fabricate porous sponges of poly (D, L-lactic-co-glycolic acid) without the use of organic solvents. *Biomaterials*, **17**, 1417-1422.

Morales, R., da Cunha, C. and Rambo, C. (2014) A complex network approach for the growth of aerogels. *Physica A: Statistical Mechanics and its Applications*, **406**, 131-138.

Mou, Z.-L., Zhao, L.-J., Zhang, Q.-A., Zhang, J. and Zhang, Z.-Q. (2011) Preparation of porous PLGA/HA/collagen scaffolds with supercritical CO_2 and application in osteoblast cell culture. *The Journal of Supercritical Fluids*, **58**, 398-406.

Mourya, V. and Inamdar, N. N. (2008) Chitosan-modifications and applications: opportunities galore. *Reactive and Functional polymers*, **68**, 1013-1051.

Murphy, W. L., Dennis, R. G., Kileny, J. L. and Mooney, D. J. (2002) Salt fusion: an approach to improve pore interconnectivity within tissue engineering scaffolds. *Tissue engineering*, **8**, 43-52.

Muzzarelli, R. A. (1973). Natural chelating polymers; alginic acid, chitin and chitosan. Natural chelating polymers; alginic acid, chitin and chitosan, Pergamon Press.

Naddeo, F., Cappetti, N. and Naddeo, A. (2014) Automatic versatile parametric procedure for a complete FEM structural analysis of composites having cylinder-shaped reinforcing fibres. *Computational Materials Science*, **81**, 239-245.

Nair, L. S. and Laurencin, C. T. (2007) Biodegradable polymers as biomaterials. *Progress in Polymer Science*, **32**, 762-798.

Nam, Y. S. and Park, T. G. (1999) Porous biodegradable polymeric scaffolds prepared by thermally induced phase separation. *Journal of biomedical materials research*, **47**, 8-17.

Nandakumar, A., Fernandes, H., de Boer, J., Moroni, L., Habibovic, P. and van Blitterswijk, C. A. (2010) Fabrication of bioactive composite scaffolds by electrospinning for bone regeneration. *Macromolecular bioscience*, **10**, 1365-1373.

Nukavarapu, S. P., Kumbar, S. G., Brown, J. L., Krogman, N. R., Weikel, A. L., Hindenlang, M. D., Nair, L. S., Allcock, H. R. and Laurencin, C. T. (2008) Polyphosphazene/nano-hydroxyapatite composite microsphere scaffolds for bone tissue engineering. *Biomacromolecules*, **9**, 1818-1825.

Oh, S. H., Kang, S. G., Kim, E. S., Cho, S. H. and Lee, J. H. (2003) Fabrication and characterization of hydrophilic poly(lactic-co-glycolic acid)/poly(vinyl alcohol) blend cell scaffolds by melt-molding particulate-leaching method. *Biomaterials*, **24**, 4011-4021.

Ozdil, D. and Aydin, H. M. (2014) Polymers for medical and tissue engineering applications. *Journal of Chemical Technology & Biotechnology*, **89**, 1793-1810.

Peppas, N. A. and Khare, A. R. (1993) Preparation, structure and diffusional behavior of hydrogels in controlled release. *Advanced drug delivery reviews*, **11**, 1-35.

Pirard, R. and Pirard, J.-P. (1997) Aerogel compression theoretical analysis. *Journal of non-crystalline solids*, **212**, 262-267.

Pisanti, P., Yeatts, A. B., Cardea, S., Fisher, J. P. and Reverchon, E. (2012) Tubular perfusion system culture of human mesenchymal stem cells on poly-L-lactic acid scaffolds produced using a supercritical carbon dioxide-assisted process. *Journal of Biomedical Materials Research Part A*, **100**, 2563-2572.

Pu, N.-W., Wang, C.-A., Sung, Y., Liu, Y.-M. and Ger, M.-D. (2009) Production of few-layer graphene by supercritical CO_2 exfoliation of graphite. *Materials Letters*, **63**, 1987-1989.

Puppi, D., Chiellini, F., Piras, A. and Chiellini, E. (2010) Polymeric materials for bone and cartilage repair. *Progress in Polymer Science*, **35**, 403-440.

Quintanilla, J., Reidy, R., Gorman, B. and Mueller, D. (2003) Gaussian random field models of aerogels. *Journal of applied physics*, **93**, 4584-4589.

Rangappa, D., Sone, K., Wang, M., Gautam, U. K., Golberg, D., Itoh, H., Ichihara, M. and Honma, I. (2010) Rapid and Direct Conversion of Graphite Crystals into High-Yielding, Good-Quality Graphene by Supercritical Fluid Exfoliation. *Chemistry-A European Journal*, **16**, 6488-6494.

Reverchon, E. and Cardea, S. (2004) Formation of cellulose acetate membranes using a supercritical fluid assisted process. *Journal of Membrane Science*, **240**, 187-195.

Reverchon, E. and Cardea, S. (2005a) Formation of polysulfone membranes by supercritical CO_2. *The Journal of Supercritical Fluids*, **35**, 140-146.

Reverchon, E. and Cardea, S. (2006a) PVDF-HFP membrane formation by supercritical CO_2 processing: elucidation of formation mechanisms. *Industrial & Engineering Chemistry Research*, **45**, 8939-8945.

Reverchon, E. and Cardea, S. (2007a) Production of controlled polymeric foams by supercritical CO_2. *The Journal of Supercritical Fluids*, **40**, 144-152.

Reverchon, E., Cardea, S. and Rappo, E. S. (2006c) Production of loaded PMMA structures using the supercritical CO_2 phase inversion process. *Journal of Membrane Science*, **273**, 97-105.

Reverchon, E., Cardea, S. and Rapuano, C. (2007b) Formation of poly-vinyl-alcohol structures by supercritical CO_2. *Journal of applied polymer science*, **104**, 3151-3160.

Reverchon, E., Cardea, S. and Rapuano, C. (2008) A new supercritical fluid-based process to produce scaffolds for tissue replacement. *The Journal of Supercritical Fluids*, **45**, 365-373.

Reverchon, E., Pisanti, P. and Cardea, S. (2009) Nanostructured PLLA−Hydroxyapatite Scaffolds Produced by a Supercritical Assisted Technique. *Industrial & Engineering Chemistry Research*, **48**, 5310-5316.

Reverchon, E., Rappo, E. S. and Cardea, S. (2006d) Flexible supercritical CO_2-assisted process for poly (methyl methacrylate) structure formation. *Polymer Engineering & Science*, **46**, 188-197.

Rezwan, K., Chen, Q., Blaker, J. and Boccaccini, A. R. (2006) Biodegradable and bioactive porous polymer/inorganic composite scaffolds for bone tissue engineering. *Biomaterials*, **27**, 3413-3431.

Rinaudo, M. (2008) Main properties and current applications of some polysaccharides as biomaterials. *Polymer International*, **57**, 397-430.

Sabirzyanov, A., Il'in, A., Akhunov, A. and Gumerov, F. (2002) Solubility of water in supercritical carbon dioxide. *High Temperature*, **40**, 203-206.

Salerno, A., Iannace, S. and Netti, P. A. (2008) Open-Pore Biodegradable Foams Prepared via Gas Foaming and Microparticulate Templating. *Macromolecular bioscience*, **8**, 655-664.

Salerno, A., Zeppetelli, S., Maio, E. D., Iannace, S. and Netti, P. A. (2010) Novel 3D porous multi-phase composite scaffolds based on PCL, thermoplastic zein and ha prepared via supercritical CO_2 foaming for bone regeneration. *Composites Science and Technology*, **70**, 1838-1846.

Sarno, M., Cirillo, C. and Ciambelli, P. (2014) Selective graphene covering of monodispersed magnetic nanoparticles. *Chemical Engineering Journal*, **246**, 27-38.

Schenker, I., Filser, F. T., Herrmann, H. J. and Gauckler, L. J. (2009) Generation of porous particle structures using the void expansion method. *Granular Matter*, **11**, 201-208.

Schugens, C., Maquet, V., Grandfils, C., Jérôme, R. and Teyssie, P. (1996) Polylactide macroporous biodegradable implants for cell transplantation. II. Preparation of polylactide foams by liquid-liquid phase separation. *Journal of biomedical materials research*, **30**, 449-461.

Sheridan, M., Shea, L., Peters, M. and Mooney, D. (2000) Bioabsorbable polymer scaffolds for tissue engineering capable of sustained growth factor delivery. *Journal of controlled release*, **64**, 91-102.

Shields, K. J., Beckman, M. J., Bowlin, G. L. and Wayne, J. S. (2004) Mechanical properties and cellular proliferation of electrospun collagen type II. *Tissue engineering*, **10**, 1510-1517.

Silva, S. S., Duarte, A. R. C., Carvalho, A. P., Mano, J. F. and Reis, R. L. (2011) Green processing of porous chitin structures for biomedical applications combining ionic liquids and supercritical fluid technology. *Acta Biomaterialia*, **7**, 1166-1172.

Singh, L., Kumar, V. and Ratner, B. D. (2004) Generation of porous microcellular 85/15 poly (DL-lactide-co-glycolide) foams for biomedical applications. *Biomaterials*, **25**, 2611-2617.

Singh, M., Morris, C. P., Ellis, R. J., Detamore, M. S. and Berkland, C. (2008) Microsphere-based seamless scaffolds containing macroscopic gradients of encapsulated factors for tissue engineering. *Tissue Engineering Part C: Methods*, **14**, 299-309.

Speer, D. P., Chvapil, M., Eskelson, C. and Ulreich, J. (1980) Biological effects of residual glutaraldehyde in glutaraldehyde-tanned collagen biomaterials. *Journal of biomedical materials research*, **14**, 753-764.

Stafford, C. M., Russell, T. P. and McCarthy, T. J. (1999) Expansion of polystyrene using supercritical carbon dioxide: effects of molecular weight, polydispersity, and low molecular weight components. *Macromolecules*, **32**, 7610-7616.

Stankovich, S., Dikin, D. A., Piner, R. D., Kohlhaas, K. A., Kleinhammes, A., Jia, Y., Wu, Y., Nguyen, S. T. and Ruoff, R. S. (2007) Synthesis of graphene-based nanosheets via chemical reduction of exfoliated graphite oxide. *Carbon*, **45**, 1558-1565.

Stephens, D., Li, L., Robinson, D., Chen, S., Chang, H.-C., Liu, R. M., Tian, Y., Ginsburg, E. J., Gao, X. and Stultz, T. (2000) Investigation of the in vitro release of gentamicin from a polyanhydride matrix. *Journal of controlled release*, **63**, 305-317.

Stropnik, Č. and Kaiser, V. (2002) Polymeric membranes preparation by wet phase separation: mechanisms and elementary processes. *Desalination*, **145**, 1-10.

Tai, H., Mather, M. L., Howard, D., Wang, W., White, L. J., Crowe, J. A., Morgan, S. P., Chandra, A., Williams, D. J. and Howdle, S. M. (2007) Control of pore size and structure of tissue engineering scaffolds produced by supercritical fluid processing. *Eur Cell Mater*, **14**, 64-77.

Temtem, M., Casimiro, T., Mano, J. F. and Aguiar-Ricardo, A. (2008) Preparation of membranes with polysulfone/polycaprolactone blends using a high pressure cell specially designed for a CO_2-assisted phase inversion. *The Journal of Supercritical Fluids*, **43**, 542-548.

Temtem, M., Pompeu, D., Jaraquemada, G., Cabrita, E., Casimiro, T. and Aguiar-Ricardo, A. (2009) Development of PMMA membranes functionalized with hydroxypropyl-β-cyclodextrins for controlled drug delivery using a supercritical CO_2-assisted technology. *International journal of pharmaceutics*, **376**, 110-115.

Tsioptsias, C. and Panayiotou, C. (2008a) Foaming of chitin hydrogels processed by supercritical carbon dioxide. *The Journal of Supercritical Fluids*, **47**, 302-308.

Tsioptsias, C. and Panayiotou, C. (2008b) Preparation of cellulose-nanohydroxyapatite composite scaffolds from ionic liquid solutions. *Carbohydrate polymers*, **74**, 99-105.

Tsioptsias, C., Stefopoulos, A., Kokkinomalis, I., Papadopoulou, L. and Panayiotou, C. (2008c) Development of micro-and nano-porous composite materials by processing cellulose with ionic liquids and supercritical CO_2. *Green Chemistry*, **10**, 965-971.

Tsivintzelis, I., Marras, S. I., Zuburtikudis, I. and Panayiotou, C. (2007) Porous poly(l-lactic acid) nanocomposite scaffolds prepared by phase inversion using supercritical CO_2 as antisolvent. *Polymer*, **48**, 6311-6318.

Vacanti, J. P. and Langer, R. (1999) Tissue engineering: the design and fabrication of living replacement devices for surgical reconstruction and transplantation. *The Lancet*, **354**, S32-S34.

Van de Witte, P., Dijkstra, P., Van den Berg, J. and Feijen, J. (1996a) Phase separation processes in polymer solutions in relation to membrane formation. *Journal of Membrane Science*, **117**, 1-31.

Vasita, R. and Katti, D. S. (2006) Nanofibers and their applications in tissue engineering. *International Journal of nanomedicine*, **1**, 15.

Velasco, D., Benito, L., Fernández-Gutiérrez, M., San Román, J. and Elvira, C. (2010) Preparation in supercritical CO_2 of porous poly(methyl methacrylate)–poly(l-lactic acid) (PMMA–PLA) scaffolds incorporating ibuprofen. *The Journal of Supercritical Fluids*, **54**, 335-341.

Wang, S.-D., Zhang, Y.-Z., Yin, G.-B., Wang, H.-W. and Dong, Z.-H. (2010) Fabrication of a composite vascular scaffold using electrospinning technology. *Materials Science and Engineering: C*, **30**, 670-676.

Wei, G. and Ma, P. X. (2004) Structure and properties of nano-hydroxyapatite/polymer composite scaffolds for bone tissue engineering. *Biomaterials*, **25**, 4749-4757.

Wei, G. and Ma, P. X. (2006) Macroporous and nanofibrous polymer scaffolds and polymer/bone-like apatite composite scaffolds generated by sugar spheres. *Journal of Biomedical Materials Research Part A*, **78**, 306-315.

Wojtoniszak, M., Chen, X., Kalenczuk, R. J., Wajda, A., Łapczuk, J., Kurzewski, M., Drozdzik, M., Chu, P. K. and Borowiak-Palen, E. (2012a) Synthesis, dispersion, and cytocompatibility of graphene oxide and reduced graphene oxide. *Colloids and Surfaces B: Biointerfaces*, **89**, 79-85.

Wu, L., Zhang, H., Zhang, J. and Ding, J. (2005) Fabrication of three-dimensional porous scaffolds of complicated shape for tissue engineering. I. Compression molding based on flexible-rigid combined mold. *Tissue engineering*, **11**, 1105-1114.

Xie, C., Hu, J., Ma, H., Zhang, J., Chang, L.-J., Chen, Y. E. and Ma, P. X. (2011) Three-dimensional growth of iPS cell-derived smooth muscle cells on nanofibrous scaffolds. *Biomaterials*, **32**, 4369-4375.

Xu, Q., Pang, M., Peng, Q., Jiang, Y., Li, J., Wang, H. and Zhu, M. (2005) Effect of different experimental conditions on biodegradable polylactide membranes prepared with supercritical CO_2 as nonsolvent. *Journal of applied polymer science*, **98**, 831-837.

Yao, J., Radin, S., S. Leboy, P. and Ducheyne, P. (2005) The effect of bioactive glass content on synthesis and bioactivity of composite poly (lactic-co-glycolic acid)/bioactive glass substrate for tissue engineering. *Biomaterials*, **26**, 1935-1943.

Yoo, J. J., Meng, J., Oberpenning, F. and Atala, A. (1998) Bladder augmentation using allogenic bladder submucosa seeded with cells. *Urology*, **51**, 221-225.

Zhang, J., Zhang, H., Wu, L. and Ding, J. (2006) Fabrication of three dimensional polymeric scaffolds with spherical pores. *Journal of materials science*, **41**, 1725-1731.

Zhang, R. and Ma, P. X. (1999) Porous poly (L-lactic acid)/apatite composites created by biomimetic process.

Zhang, R. and Ma, P. X. (2000) Synthetic nano-fibrillar extracellular matrices with predesigned macroporous architectures.

Zhang, W., Yao, D., Zhang, Q., Zhou, J. G. and Lelkes, P. I. (2010) Fabrication of interconnected microporous biomaterials with high hydroxyapatite nanoparticle loading. *Biofabrication*, **2**, 035006.

Zhong, S. P., Teo, W. E., Zhu, X., Beuerman, R., Ramakrishna, S. and Yung, L. Y. L. (2007) Development of a novel collagen–GAG nanofibrous scaffold via electrospinning. *Materials Science and Engineering: C*, **27**, 262-266.

LIST OF SYMBOLS

ALP	Alkaline phosphatase
DMEM	Dulbecco’s modified eagle’s medium
DNA	Deoxyribonucleic acid
EDTA	Ethylenediaminetetraacetic acid
NaCl	Sodium chloride
NaOH	Sodium hydroxide
PBS	Phosphate buffered saline
PCL	Polycaprolactone
PDLA	Poly-D-lactide acid
PDMS	Polydimethylsiloxane
PGA	Polyglycolic acid
PHA	Polyhydroxyalkanoate
PLA	Polylactic acid
PLGA	Poly(lactic-co-glycolic acid)
PMMA	Poly(methyl methacrylate)
PVP	Polyvinylpyrrolidone
RNA	Ribonucleic acid
T	Temperature
TCP	Tricalcium phosphate
T_g	Glass transition temperature